Optimal Design Methodology of a Three Phase Rotary Transformer for a Brushless Doubly Fed Induction Generator

by

Nikita Linda Zietsman

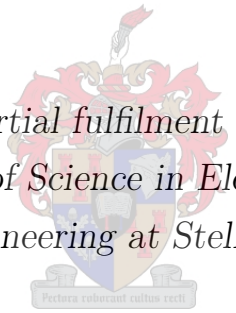

Thesis presented in partial fulfilment of the requirements for the degree of Master of Science in Electrical Engineering in the Faculty of Engineering at Stellenbosch University

Department of Electrical and Electronic Engineering,
University of Stellenbosch,
Private Bag X1, Matieland 7602, South Africa.

Supervisor: Dr. N. Gule

March 2016

Declaration

By submitting this thesis electronically, I declare that the entirety of the work contained therein is my own, original work, that I am the sole author thereof (save to the extent explicitly otherwise stated), that reproduction and publication thereof by Stellenbosch University will not infringe any third party rights and that I have not previously in its entirety or in part submitted it for obtaining any qualification.

Date: March 2016 .....

Abstract

The brushless doubly fed induction generator (BDFIG) offers higher reliability over the standard doubly fed induction generator (DFIG), by eliminating the slip ring and brush assembly. The currently employed BDFIG configuration results in a more complex machine. In order to improve reliability while still retaining the simplicity of the DFIG, alternative brushless topologies have been explored. One such solution is to make use of a rotary transformer (RT) to replace the slip rings and brushes. The RT is placed on the same shaft as the generator and provides inductive coupling over the interface.

Size and efficiency are important constraints of the RT used in a DFIG application. The purpose of this study is to develop a design methodology that takes into account the unique properties of the RT, while simultaneously minimising size and maximising efficiency. An analytical model, which makes provision for the non-idealities of the RT, is used to improve the analysis. The model is then verified using FEM. Although the improved model offers better correlation to the simulated results than the original model, there is still room for improvement.

A prototype RT, is designed using developed procedure, constructed and practically tested. The resultant size is suitably smaller than a prototype built using standard transformer design strategies. Encouraging results are obtained from the tests, indicating that the RT performs well at the rated conditions. However, a number of differences exist between the FEM analysis and the measured operation. The cause of this deviation is discussed and suitable recommendations are made for future work.

Uittreksel

Die borsellose dubbel gevoed induksie generator (BDGIG) bied hoër betroubaarheid as die standaard dubbel gevoed induksie generator (DGIG), deur die verwydering van die sleepringe en borsels. Die huidige BDGIG topologie veroorsaak 'n meer komplekse masjien. Om gelyktydig die betroubaarheid van die generator te verbeter en nogsteeds die eenvoudigheid van die DGIG te behou, alternatiewe borsellose topologieë is ondersoek. Een so oplossing is om gebruik te maak van 'n roterende transformator (RT) wat die sleepringe en borsels vervang. Die RT is op die selfde skag as die generator geplaas en lewer induktiewe koppeling oor die lug gaping.

Grootte en doeltreffendheid is belangrik beperkings van die RT. Die doel van hierdie studie is om 'n ontwerp metode te ontwikkel wat die unieke eienskappe van die RT in ag neem, en terselfdertyd die grootte verminder en doeltreffendheid maksimeer. 'n Analitiese model, wat voorsiening maak vir die nie-idealiteite van die RT, word gebruik om die ontleding van die RT te verbeter. Die model is geverifieer behulp van FEM. Hoewel die verbeterde model bied aan 'n beter korrelasie met die gesimuleerde resultate, as die oorspronklike, die model kan nogsteeds verbeter word.

'n Prototipe RT, wat ontwerp is met behulp van die metode, is gebou en prakties getoets. Die gevolglike grootte is paslik kleiner as 'n prototipe gebou met behulp van standaard transformator ontwerp strategieë. Bemoedigende resultate word verkry uit die toets, wat aandui dat die RT presteer goed by die gegradeerde voorwaardes. Daar bly 'n aantal verskille tussen die FEM ontleding en die gemeet operasie. Die oorsaak van hierdie afwyking word bespreek en gepaste aanbevelings word gemaak vir toekomstige werk.

Publications

Part of the research in this thesis has been presented at either local or international conferences. The paper details are as follows:

- N.L. Zietsman, N. Gule, "Design and Evaluation of a 1 kW Rotary Transformer", Southern African Universities Power Engineering Conference (SAUPEC), Durban, South Africa, Jan 2014.
- N.L. Zietsman, N. Gule, "Optimal Design Methodology of a Three Phase Rotary Transformer for Doubly Fed Induction Generator Application", International Electric Machines and Drives Conference (IEMDC), Coeur d'Alene, Idaho (USA), May 2015.

Acknowledgements

I would like to sincerely thank the following people for their contribution to the project:

- My supervisor, Dr. Nathie Gule, for his valuable guidance and unwavering encouragement throughout the project. Thank you for all you have taught me.
- The Centre for Renewable and Sustainable Energy Studies for providing funding for the project. I would like to thank Prof. Wikus van Niekerk in particular, for his assistance as the start of my studies.
- The SED workshop staff: Pietro Petzer, Andre Swart and Murray Jumat for all the assistance during manufacturing, equipment setup and testing.
- Theunis Roux for his expert advice and assistance during manufacturing.
- My EMLab colleagues for their advice, support and friendship.
- My family and friends for their continuous support and motivation throughout my studies. I owe each of you a great deal.

The best view comes after the hardest climb.

To Andrew,
for climbing each mountain alongside me.

Contents

List of Figures

List of Tables

Nomenclature

Variables

A	Magnetic path cross sectional area	$[\mathrm{m}^2]$
A_c	RT core cross secional area	$[\mathrm{cm}^2]$
A_p	Area product	$[\mathrm{cm}^4]$
A_w	RT window area	$[\mathrm{cm}^2]$
A_{wp}	Cross sectional conductor area (primary winding)	$[\mathrm{m}^2]$
A_{ws}	Cross sectional conductor area (secondary winding)	$[\mathrm{m}^2]$
B	Flux density	$[\mathrm{T}]$
B_o	Operating flux density	$[\mathrm{T}]$
B_{sat}	Saturation flux density of material	$[\mathrm{T}]$
e_{ind}	Induced emf	$[\mathrm{V}]$
E_t	Emf/turn	$[\mathrm{V/turn}]$
$\mathcal{F}$	Magnetomotive force	$[\mathrm{A \cdot turns}]$
f	Frequency	$[\mathrm{Hz}]$
f_m	Mechanical frequency of rotor	$[\mathrm{Hz}]$
f_r	Rotor frequency	$[\mathrm{Hz}]$
f_s	Stator frequency	$[\mathrm{Hz}]$
η	Efficiency	$[\%]$
H	Magnetic field intensity	$[\mathrm{A/m}]$
i_p	Primary current	$[\mathrm{A}]$
i_s	Secondary current	$[\mathrm{A}]$
J	Current density	$[\mathrm{A/mm}^2]$
J_{max}	Maximum current density	$[\mathrm{A/mm}^2]$
K	Emf/turn constant	$[\ ]$

K_f	Waveform coefficient	[ ]
K_u	Window utilisation/fill factor	[ ]
λ_p	Primary winding flux linkage	[Wb · turns]
λ_s	Secondary winding flux linkage	[Wb · turns]
l	length	[m]
L	Inductance	[H]
L_{11}	Primary winding self inductance	[H]
L_{12}	Mutual inductance	[H]
L_{22}	Secondary winding self inductance	[H]
L_{lk}	Winding leakage inductance	[H]
L_{lkp}	Primary winding leakage inductance	[H]
L_{lks}	Secondary winding leakage inductance	[H]
L_m	Magnetising inductance	[H]
L_{mp}	Magnetising inductance as seen from primary side	[H]
L_{ms}	Magnetising inductance as seen from primary side	[H]
l_p	Mean length of turns of RT primary winding	[m]
l_s	Mean length of turns of RT secondary winding	[m]
μ_0	Permeability of air	[H/m]
μ_r	Relative Permeabillity	[H/m]
N	Number of turns	[ ]
N_p	Rotor power	[W]
N_s	Mechanical torque	[Nm]
n_m	Mechanical speed	[rpm]
n_s	Synchronous speed	[rpm]
ρ	Resistivity of winding	[Ω/m]
p	Pole number	[ ]
P_m	Mechanical power	[W]
P_o	Output power	[W]
P_s	Stator power	[W]
P_r	Rotor power	[W]
P_t	Apparent power	[VA]

$\mathcal{R}$	Reluctance	[A · turns/Wb]
R_p	Primary winding resistance	[Ω]
R_s	Secondary winding resistance	[Ω]
s	Slip	[ ]
T_m	Mechanical torque	[Nm]
T_{em}	Electromagnetic torque	[Nm]
ϕ_m	Mutual flux	[Wb]
ϕ	Magnetic flux	[Wb]
ϕ_p	Primary winding flux	[Wb]
ϕ_s	Secondary winding flux	[Wb]
ϕ_{lp}	Primary winding leakage flux	[Wb]
ϕ_{ls}	Secondary winding leakage flux	[Wb]
v_p	Primary voltage	[V]
v_s	Secondary voltage	[V]
ω_m	Mechanical angular velocity	[rad/s]
ω_s	Synchronous angular velocity	[rad/s]

Constants

$\mu_0 = \quad 4\pi \times 10^{-7}\ H/m$

$\rho_{cu} = \quad 1.72 \times 10^{-8}\ \Omega/m$

Abbreviations

2D	Two Dimensional
3D	Three Dimensional
BDFIG	Brushless Doubly Fed Induction Generator
DC	Direct Current
DD	Direct Drive
DFIG	Doubly Fed Induction Generator
FEM	Finite Element Method
IG	Induction Generator
LVRT	Low Voltage Ride-Through
MLT	Mean Length of Turn

MMF Magnetomotive Force

MW Mega Watt

PM Permanent Magnet

RT Rotary Transformer

SMC Soft Magnetic Composites

SG Synchronous Generator

Chapter 1

Introduction

Wind energy generation has seen considerable growth in recent years. At the end of 2014 the Global Wind Energy Council (GWEC) reported a global installed capacity of almost 370 GW, with wind energy accounting for the second largest renewable source after hydroelectric power [1]. The increase in wind energy capacity from 2013 - 2014 for a number of countries is shown in Figure 1.1.

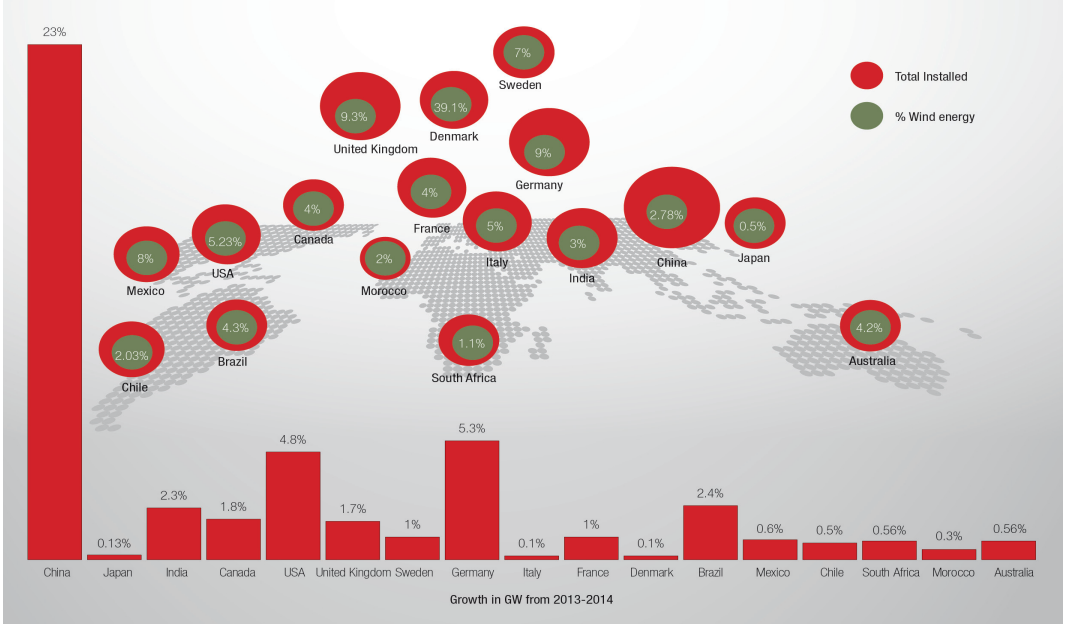

Figure 1.1: Growth in installed wind capacity for 2013-2014 and wind energy as a percentage of total capacity of each country. Compiled from data given in [1].

Denmark maintained its status as global leader with 39.1 % of the installed capacity being generated from wind. China saw the highest growth moving into 2014, with an ground breaking addition of 23 196 MW. South Africa has seen rapid development in the past couple of years, and the 560 MW installed in 2014 cements the country's status as one of the leading new markets in wind power [1].

One of the main hurdles in the growth of the sector is the high cost associated with the new technologies. The electrical generators used in these wind turbines are of prime importance in ensuring that maximum kinetic energy is harnessed, and thereby decreasing the overall cost. Two main issues that need to be addressed are the efficiency and the reliability of the generator. Currently, research is being conducted in order to maximise the efficiency and improve the reliability of the wind energy conversion system.

The generators used for wind turbines can either be fixed or variable speed. The constant speed induction generator (IG) shown in Figure 1.2(a) is becoming less prevalent as the variable speed setup offers a wider speed capability [2].

There are currently three commonly used variable speed generator topologies [2], namely,

- High speed brushless permanent magnet (PM) or IG with full converter
- Direct drive (DD) systems
- Doubly fed induction generator (DFIG)

The variable speed brushless generator has been developed with the setup shown in Figure 1.2(b). The turbine drive train consists of a gearbox, a brushless generator (either a high speed permanent magnet machine or a squirrel cage induction machine) and a fully rated converter. The setup avoids the use of slip rings, decreasing maintenance costs. However, the fully rated converter introduces higher losses than the partially rated converter setups [2].

An emerging trend is the direct drive (DD) system shown in Figure 1.2(c). The drive train consists of a synchronous generator (SG) directly coupled to the turbine with no need for a gearbox [2]. The rotor of the SG can either consist

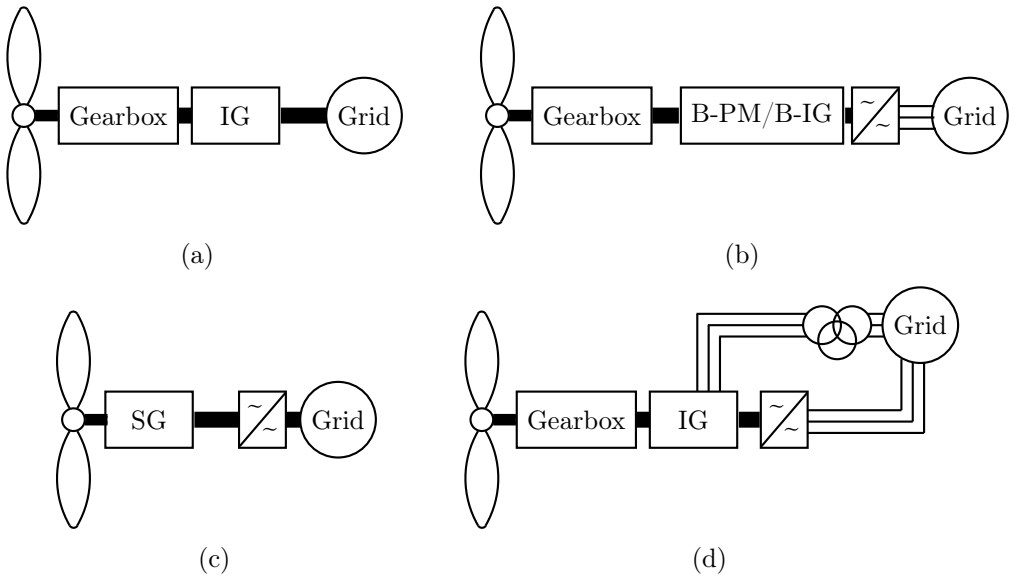

Figure 1.2: Drive train topologies. (a) Fixed speed induction generator, (b) Brushless generator with fully rated converter, (c) direct drive synchronous generator and (d) Variable speed doubly fed induction generator

of permanent magnets or a wound rotor requiring external excitation. The SG requires a fully rated converter in order to couple to the grid. The advantage of the DD is the improvement in reliability by removing the gearbox. However, the physical size of machine becomes larger as the generator has to handle the full torque of the turbine. This increase in size also leads to a higher cost. To overcome these limitations, various hybrid drive-trains have been proposed [2].

The DFIG configuration is shown in Figure 1.2(d). The drive train consists of a gearbox, a wound rotor induction machine and a power converter. With this drive train the generator has a speed range of $\pm$ 30% of the synchronous speed. The DFIG has windings on both the stator and the rotor. Access to the rotor windings allows for control of the rotor current frequency and amplitude. The power converter used for this control is connected to the rotor of the generator, and is therefore only required to handle a fraction of the rotor power, typically a third of the mechanical power. The advantages of lower initial cost and partially rated converter has made the DFIG the most widely installed system currently.

Although the DFIG is the most widely employed system, there are two dis-

advantages that have warranted further research. Firstly, the slip ring and brush assembly used to access the rotor winding. A study conducted in [3] found that the most common cause of downtime of the generator subsystem is the replacement of worn brushes. Secondly, the poor grid-fault ride-through capabilities of the DFIG [4]. Significant research has been conducted in order to improve the DFIG's fault ride-through capabilities [5–9]. In recent years, a number of studies have been conducted into the use of a brushless doubly fed induction generator (BDFIG). The concept consists of stator with two separate three phase windings, each with its own pole number, and a special rotor cage to couple both windings [10]. The BDFIG addresses both the fault ride-through characteristics and the reliability of the DFIG [11–13].

A recently proposed alternative to the BDFIG is to use a standard DFIG with a rotary transformer to replace the slip rings [14–16]. The rotary transformer (RT) can be used to inductively couple the two circuits. This avoids the mechanical contact of the slip ring as shown in Figure 1.3(a) and prevents wear of the components. The RT concept was first proposed by Gibson in 1961 for high frequency power transfer [17]. The setup consists of a standard transformer core with an added air gap to facilitate rotation as shown in Figure 1.3(b). The principle of magnetic coupling allows for contactless energy transfer over a rotating interface. Elimination of the mechanical contact leads to a decrease in maintenance and subsequent downtime of the turbine.

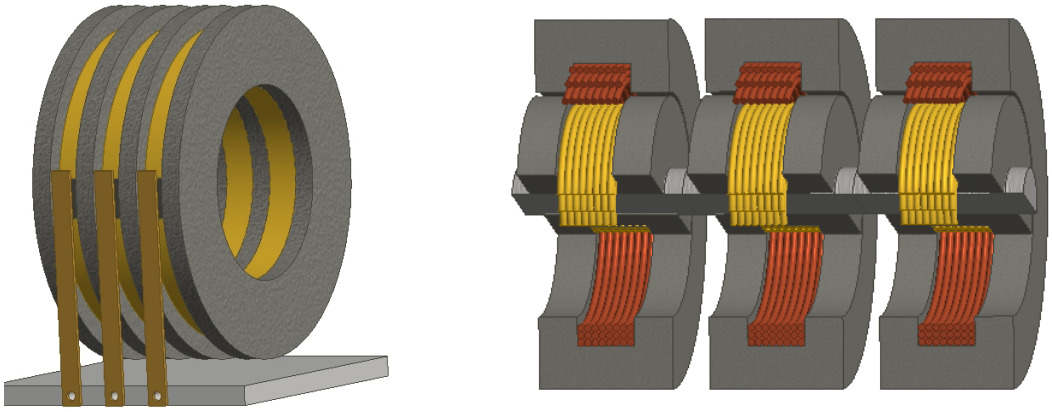

(a) (b)

Figure 1.3: (a) Slip ring and brush assembly, and (b) The proposed RT.

1.1 Literature Review

The DFIG is a well developed concept. Recently numerous studies have been conducted on the BDFIG concept. The BDFIG is attractive as it offers an alternative to slip rings whilst still making use of the DFIG advantages. The following section provides a summary of the studies conducted on BDFIG concepts.

1.1.1 Brushless Doubly Fed Induction Genearator (BDFIG)

As discussed in the previous section, there are various drive train options that eliminate the need for brushes. However, since the advantages of the DFIG's partially rated converter and low initial cost are still appealing, the brushless doubly fed induction generator (BDFIG) is advantageous.

The BDFIG consists of two stator windings, the power winding (directly coupled to the grid) and the control winding (supplied by the converter). The two stator windings each have a different pole number, which avoids coupling between the two, and each produce a separate field. Both these fields link with the specially designed rotor. The generator operates in the synchronous mode and the rotor mechanical speed is a function of the frequencies of the power and control windings currents. The generator operates at medium speeds (due to the effective higher pole number), which allows for the use of a single or two stage gearbox [18]. This is an advantage over the standard DFIG. Another advantage is the improved low voltage ride-through (LVRT) capability of the BDFIG. In a standard DFIG the stator winding is connected directly to the grid and any sudden drop in voltages leads to a loss of magnetisation in the machine and a subsequent surge in rotor current. The BDFIG has a larger series inductance and this results in a lower transient current which allows the generator to cope with the voltage dips without a crowbar circuit or extra current control that the standard DFIG requires [8].

Despite the advantages the BDFIG offers, the result is a machine that is more complex than the standard DFIG. Due to the two excitation windings, the machine is complicated to model. Several medium rating machines have been developed [11] , [19], [20]. Design and analysis of a large 6 MW machine has

been presented in [21], although it still remains to be demonstrated in practice at this power rating. An increase in size and overall machine weight is to be expected. The study in [18] shows that the weight increases by approximately 30 % for the same power density. The higher rotor inductance also impacts the reactive power management and leads to a lower efficiency [22].

There exists a need to explore additional brushless topologies, specifically a setup that allows for the simplicity of the DFIG to remain intact. The performance of these technologies can be compared to the current BDFIG so as to develop an improved DFIG drive train.

An RT can be employed along with a standard DFIG to yield a brushless generator. The following section introduces the RT concept.

1.1.2 DFIG with RT

Since the concept was first proposed, the RT has been used for a number of varying applications. Recently research has started into RTs providing coupling in DFIG setups [15,16,23]. The RT is placed on the rotor of the induction machine, and provides access to the rotor windings. For this application the operating frequency of the RT is equal to the slip frequency of the machine. This low operating frequency leads to an overall larger RT and also requires the use of a laminated core. This laminated core results in a more complicated assembly. The technique for constructing the core proposed in [16] is to divide the rotor and stator into segments. A guideline for determining number of segments is provided as well as a model for the system. The proposed design was not practically implemented, so it is not clear which material would be suitable for this application or whether the the proposed technique is practically realisable.

Another approach to this problem is to use a combination of lamination directions. The RT designed in [24] uses a combination of axial and radial laminations to limit the eddy currents in the core. The yoke sections are axially laminated while the limbs are radially laminated, as shown in Figure 1.4. Since the flux flows in the direction of the laminations in each section, eddy currents will be induced in the core. To mitigate these, the laminations contain gaps that act as high resistance eddy current barriers. These barriers are

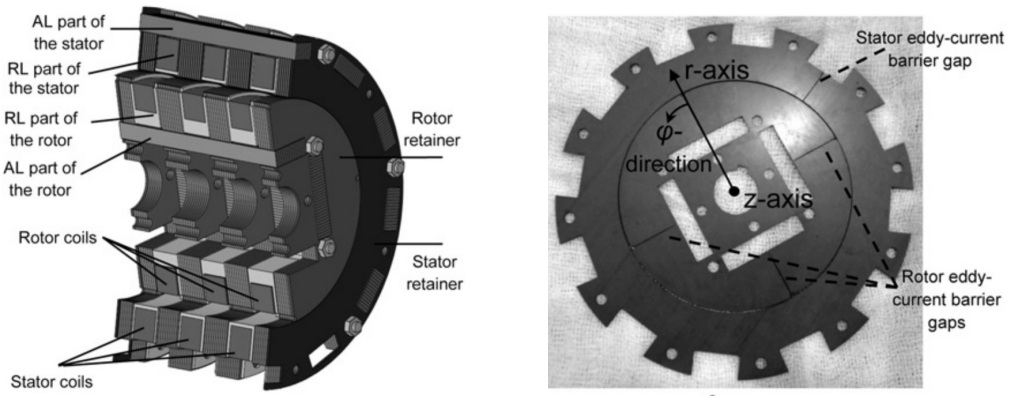

(a) (b)

Figure 1.4: Combination of axially and radially laminated core. (a) Three phase RT configuration and (b) Eddy current barriers in the laminations [24].

illustrated in Figure 1.4(b).

To address the large core area Lipo et al proposed a two phase RT to reduce the total volume. A three phase to two phase transformation can then be done. This results in a significant 35 % reduction in volume. However, this two phase RT results in an unbalance of the system which requires more complex control [23].

The study conducted in [25, 26] highlights the large size of the RT for a given power rating. For application within a DFIG drivetrain, weight is an important factor. The RT's size needs to be addressed when discussing the suitability for this application. The RTs developed by WEG for both the 90 kW and 350 kW DFIGs appear to be comparable in size to the actual induction generator [15], [14].

The prototype developed in [25] experienced core saturation at the designed operating point and had to be de-rated. However, an acceptable efficiency of 90 % was achieved at the new operating point [25, 26]. The RT developed in [27] also achieved an efficiency of 90 %. The conclusions drawn are that the large through-bore requirement resulted in an inefficient use of core and winding material. The measured full load efficiency of the unoptimised RT in [24] is 85 %, with copper loss being the main contributor. The implementation

of a RT into a DFIG drive train in the study conducted by WEG yielded an high overall system efficiency of 94.8 %. This is comparable to efficiencies of a typical transformer. The power factor is lower than in comparable DFIG's due to the inductive nature of the RT [14].

An RT is used to provide brushless excitation to a synchronous motor in an electrical vehicle in the study presented in [28]. The traditional excitation circuit and the proposed brushless adaptation are shown in Figure 1.5(a) and Figure 1.5(b) respectively. Since the supply is a DC battery, an extra inverter and rectifier stage is required for the RT. The developed RT realised extremely high efficiencies of 98.9 % (pot core) and 99.2 % (axial). The overall system efficiency is 67 % and 61 % respectively, due to the low converter efficiency. This highlights the need to compare the whole slip ring replacement system as a whole in order to accurately evaluate the suitability.

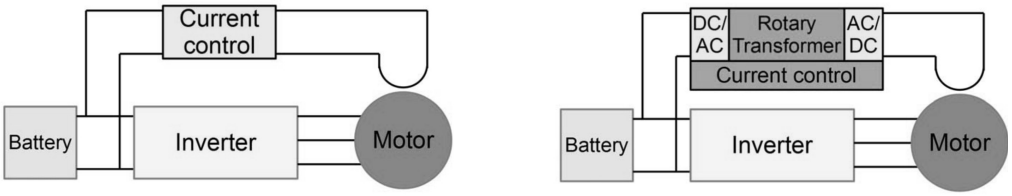

(a) (b)

Figure 1.5: (a) Excitation of the synchronous machine and (b) the proposed brushless topology with necessary converter [28].

1.2 Research Objectives

The DFIG is a popular and widely implemented generator in medium to large wind turbines. Although lower capital expenditure and the partially rated power converter makes the generator competitive, the issue of reliability is still open for investigation. The RT has been proposed to replace the slip ring assembly, thus eliminating wear and frequent maintenance. The suitability of the concept for this application has been proved in [14, 25], however challenges still remain in terms of the design procedure and the relative large size for a

given power rating.

The aim of this project is to develop a design methodology that successfully addresses the unique characteristics of the RT. The design procedure should yield the optimal minimum size while maintaining an acceptable efficiency. The developed methodology is used to design a RT which is manufactured and tested in order to evaluate the predicted performance.

1.3 Thesis Layout

The thesis is laid out as follows:

Chapter 1

The first chapter is an introduction into the project. A literature review is conducted on BDFIG topologies and RTs. The motivations for the research are highlighted and the aims of the study are presented.

Chapte 2

In this chapter, an alternative DFIG topology is considered to improve the performance of the RT. The operation of the BDFIG in this configuration is discussed in this chapter.

Chapter 3

The RT's unique operating principles are explained in this chapter. How the operation characteristics compare to that of a standard transformer is also discussed. A thorough review of the current research is conducted.

Chapter 4

An analytical model of the RT is developed in this chapter. The technique sets out to model the characteristics that are unique to the RT. This provides a starting point for the design and the model can be used for finite element method (FEM) analysis of the machine.

Chapter 5

In this chapter, a design methodology for an RT is presented. A study of scalability of RTs at increasing power levels is also conducted. A prototype is designed, using the presented methodology,that will be built and tested to verify the design process.

Chapter 6

The mechanical design of the RT is outlined in this chapter. The manufacturing procedure is involved and therefore the process is covered in detail.

Chapter 7

The designed RT is tested in order to verify the design methodology and determine the accuracy of the developed analytical model. The results of theses tests are presented and compared with the analytical and FEM analysis.

Chapter 8

The final chapter presents the conclusions of the study, along with recommendations for future research.

Chapter 2

Rotor-Tied BDFIG

The brushless generator topology considered in this study is a DFIG fitted with an RT in place of the slip rings. The proposed drive train consists of an RT on the same shaft as the induction generator's rotor. The RT assembly will transfer the three phase power of the rotor to the back-to-back converter as indicated in Figure 2.1(a). The changes to the DFIG to accommodate the RT need to be addressed, before the specific RT design considerations are discussed in detail. The operating frequency of the RT is an important design consideration, as size of the RT is inversely proportional to the frequency.

A DFIG configuration whereby the rotor, instead of the stator, is coupled to the grid has been presented by You et al in [29]. The suggested topology is indicated in Figure 2.1(b). The use of this topology allows the rotor, and therefore the RT, to operate at grid frequency (50/60 Hz) instead of the lower slip frequency (2-5% of rated). The topology also leads to a induction machine with a decreased outer diameter and higher torque-to-weight ratio [29].

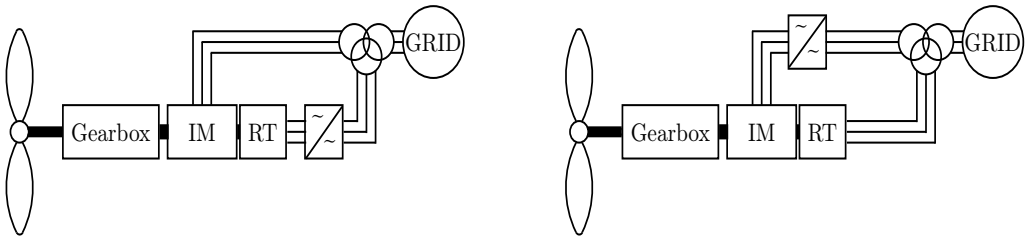

(a) (b)

Figure 2.1: (a) The stator-tied DFIG topology and (b) Rotor-tied DFIG topology.

2.1 DFIG Operation

An important feature of any grid connected generator is the ability to provide constant voltage and frequency output on the grid side. The DFIG can handle large variations in wind speeds while providing a constant frequency and voltage on the grid coupled side. Constant frequency is achieved by adjusting the frequency and amplitude of the currents fed into the rotor, so that they counteract the variation in mechanical speed of the rotor. Grid compliant voltage is maintained as long as the specific magnetic flux value remains constant. This magnetic flux value is dependent on the voltage/frequency ratio, and so the voltage applied to the rotor windings must be proportional to the necessary applied frequency. Common practice for the ratio between voltage and frequency is a value such that the reactive power at the stator side is equal to zero.

The frequency of the induced voltage that needs to be fed into the rotor in order to maintain the grid frequency on the stator, despite changes in mechanical speed is,

$$f_r = f_s - f_m, \tag{2.1.1}$$

where f_s is the frequency of the induced voltages in the stator, f_r is the frequency of the applied currents on the rotor, and f_m is the rotor's mechanical frequency, given by:

$$f_m = \frac{n_m \times p}{120}. \tag{2.1.2}$$

The interaction between the field produced by the applied rotor voltage, the mechanical rotation and the stator magnetic field is shown in Figure 2.2.
The DFIG has two modes of operation depending on the speed of the rotor: sub- and supersynchronous. The relative motion between the mechanical speed and the rotating magnetic field speed is represented by the well known slip concept,

$$s = \frac{n_s - n_m}{n_s} = \frac{\omega_s - \omega_m}{\omega_s}, \tag{2.1.3}$$

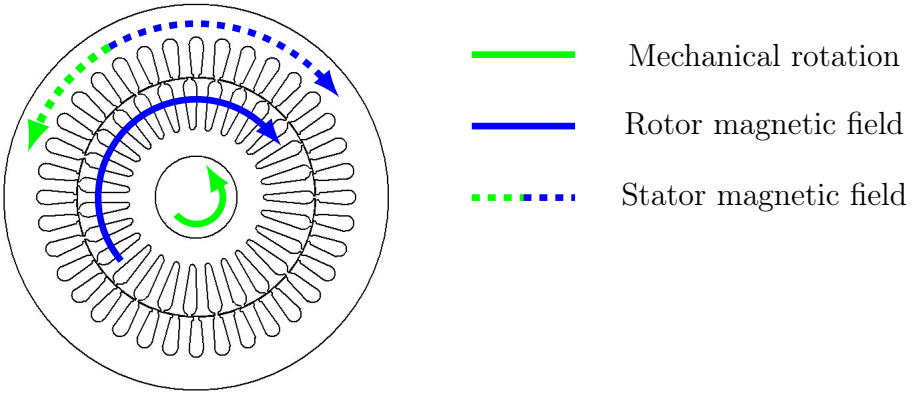

Figure 2.2: Stator magnetic field is the summation of the rotor field and mechanical rotation of the rotor.

where n_s is the synchronous speed and n_m is the mechanical speed. ω_s and ω_m are the synchronous and mechanical angular velocities respectively.

The synchronous speed for a machine with pole number, p, and frequency, f, is given by,

$$n_s = \frac{120f}{p} \tag{2.1.4}$$

Defining the positive direction as out of the generator, the power flow can be expressed by,

$$P_m = P_s + P_r, \tag{2.1.5}$$

with P_m the mechanical power from the prime mover, P_s the stator power and P_r the rotor power. Assuming a loss-less generator, at steady state equation (2.1.5) can be further evaluated as:

$$T_m\omega_m = T_{em}\omega_s + P_r, \tag{2.1.6}$$

where $T_m = T_{em}$, and T_m is the mechanical torque, ω_m is the mechanical speed, T_{em} is the developed electromechanical torque and ω_s is the synchronous speed. Rearranging equation (2.1.6) to make rotor power the subject yields,

$$P_r = T_m(\omega_m - \omega_s), \tag{2.1.7}$$

The angular velocity slip expression in equation (2.1.3) can be written as:

$$s\omega_s = \omega_s - \omega_m. \tag{2.1.8}$$

Substituting the slip expression of equation (2.1.8) into equation (2.1.7) yields an expression for the rotor power as a function of slip,

$$P_r = -sP_s \tag{2.1.9}$$

The expression for stator power as a function of slip is given by substituting equation (2.1.5) into equation (2.1.9),

$$P_s = \frac{P_m}{(1-s)}. \tag{2.1.10}$$

The direction of the power flow of both the stator and rotor depend on the slip, and thus the mechanical speed of the rotor. Evaluating equation (2.1.3) shows that the slip will be positive at speeds less than the synchronous speed, n_s. At speeds above the synchronous speed the slip will be negative. Depending on the polarity of the slip, equation (2.1.10) and equation (2.1.9) will change sign. This indicates whether power is drawn or delivered at the stator and rotor terminals. For positive slip (subsynchronous speed), power is delivered from the stator and drawn at the rotor terminals. For negative slip values (supersynchronous speed) both the rotor and the stator deliver power back to the grid. Considering a 50 Hz, 4 pole machine, a graphical representation of the regions are given in Figure 2.3.

The maximum and minimum slip values are governed by the power rating of the converter. Generally the converter is rated to handle about a third of the mechanical power. This translates into a slip range of ± 0.3.

The operation of the DFIG is adjusted for the new topology where the rotor is directly grid connected. The following section details the operating regions and characteristics of this topology.

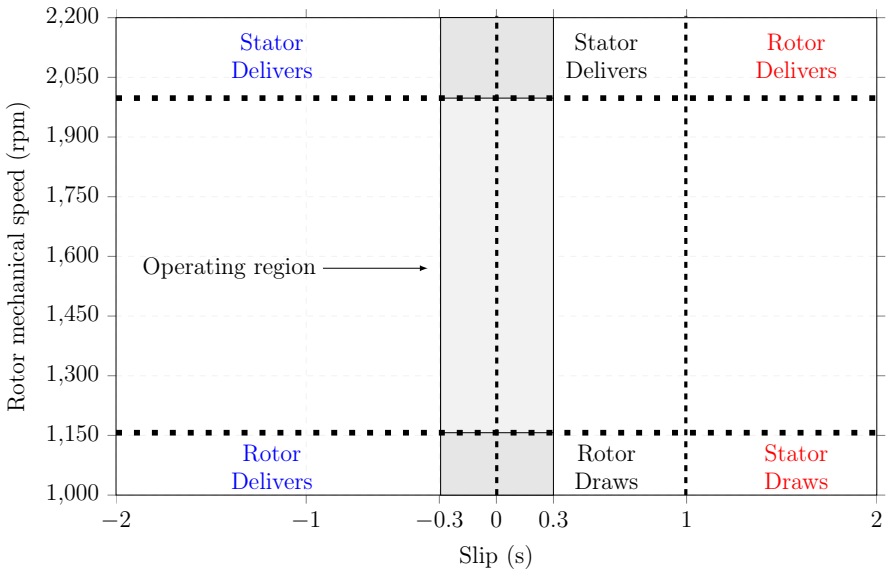

Figure 2.3: The operating region of a 50 Hz, 4 pole DFIG in the stator-tied configuration, based on the converter ratings and slip.

2.2 Rotor-tied DFIG Operation

In the rotor-tied topology the rotor is now coupled directly to the grid and carries the full power generated by the prime mover. The stator is connected to the partially rated converter. The operation in this configuration is divided into two categories: (1) The fields on the rotor and the mechanical motion are in the opposite direction, and (2) where the fields and mechanical motion are in the same direction.

2.2.1 Field and mechanical speed in opposite direction

The interactions between the magnetic fields and the mechanical rotation are illustrated in Figure 2.4. The standard slip equation is still applicable, now where the rotor field frequency is the difference between the frequency of the applied stator voltages field and the mechanical rotation. The power flow equations are given by:

$$P_s = -\frac{sP_m}{(1-s)} \tag{2.2.1}$$

$$P_s = -sP_r \tag{2.2.2}$$

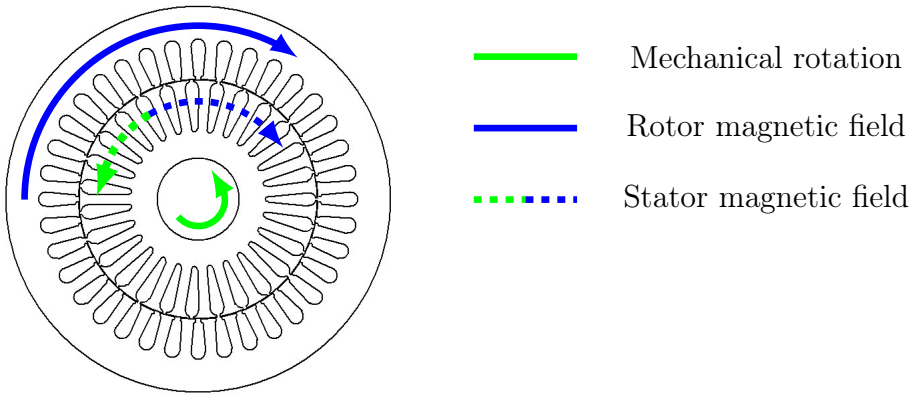

Figure 2.4: Interaction between the rotor speed and the frequency of the rotating magnetic field created by the rotor windings when the rotor rotates in the opposite direction to the applied field.

The speed regions are determined based on the converter rating. To maintain a partially rated converter, the stator power must be kept at less than a third of the developed mechanical power. The corresponding slip region is,

$$-1/2 \leq s < 1/4. \tag{2.2.3}$$

The mechanical rotor speed regions for this slip range can be determined by using the slip expression given in equation (2.1.3), so that,

$$(1 - s_1)n_s < n_m \leq (1 - s_2)n_s, \tag{2.2.4}$$

where s_1 and s_2 are the lower and upper boundaries of the slip region given inequation (2.2.3). Substitution of these boundary values yields,

$$(1.5)n_s < n_m \leq (0.75)n_s, \tag{2.2.5}$$

where n_m is the mechanical rotor speed in the opposite direction to the applied field. The frequency of the stator voltages is determined by using,

$$f_s = f_r - f_m, \tag{2.2.6}$$

The corresponding frequency range for a grid frequency of 50 Hz and generator with 'p' number of poles is given by the general expression,

$$50 - \frac{pn_{m1}}{120} < f_s \leq 50 - \frac{pn_{m2}}{120}, \tag{2.2.7}$$

The operating region the conditions described in this section is shown in Figure 2.5.

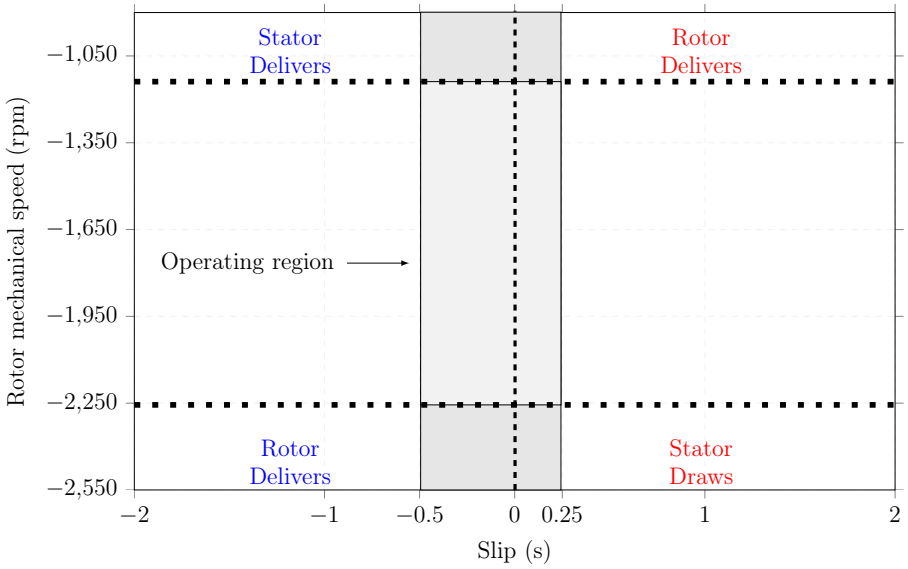

Figure 2.5: The operating region of a 50 Hz, 4 pole DFIG in the rotor-tied configuration, with the field and mechanical rotation in opposite directions

2.2.2 Field and mechanical speed in the same direction

When the rotor is rotating in the same direction as the field on the stator, the traditional slip equation no longer holds. The resultant field is a summation of the fields and the mechanical rotation, as seen in Figure 2.6.

The relationship between the speed of the applied magnetic field and the mechanical rotation is now,

$$s = \frac{n_s + n_m}{n_s}. \tag{2.2.8}$$

The corresponding relationship between the frequencies is given by,

$$f_s = f_r + f_m. \tag{2.2.9}$$

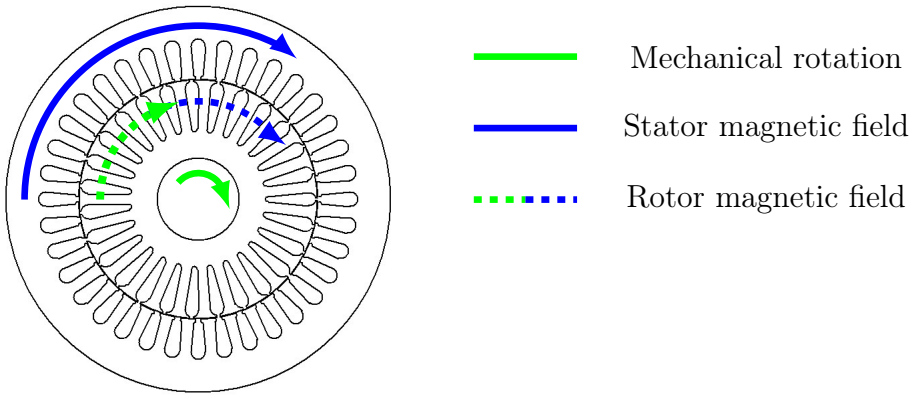

Figure 2.6: Interaction between the rotor speed and the frequency of the rotating magnetic field created by the rotor windings when the rotor rotates in the same direction as the applied field.

The power flow equations described above also need to be adjusted for the new setup. The stator power as a function of slip is,

$$P_s = \frac{sP_m}{(s-1)} - \frac{2P_m}{(s-1)}, \tag{2.2.10}$$

and the rotor power is given by,

$$P_r = \frac{P_m}{(s-1)}. \tag{2.2.11}$$

Evaluating the direction of power flow in equation (2.2.9) - equation (2.2.11) gives the following three slip regions: a) $s < 1$, b) $1 < s < 2$ and c) $s > 2$. The standard DFIG topology employs a partially rated converter on the rotor. In order to maintain a power converter (now on the stator) rated for a third of the mechanical power, it is necessary to evaluate stator power values for the slip regions above. The most suitable range for DFIG operation with a partially rated converter is,

$$7/4 < s \leq 5/2. \tag{2.2.12}$$

Substituting the limits of the slip from equation (2.2.12) the mechanical speed range can be determined as,

$$(s_1 - 1)n_s < n_m \leq (s_2 - 1)n_s, \tag{2.2.13}$$

$$(0.75)n_s < n_m \leq (1.5)n_s, \tag{2.2.14}$$

where n_m is the mechanical rotor speed in the same direction as the applied field. For a 50 Hz machine with 'p' number of poles, the corresponding frequency range of the stator voltages is,

$$50 + \frac{pn_{m1}}{120} < f_s \leq 50 + \frac{pn_{m2}}{120}, \tag{2.2.15}$$

When the slip is less than 2, the stator draws power and the rotor delivers power to the grid. This can be seen as exactly the same as the subsynchronous region in the conventional stator-tied configuration. Conversely, when the slip is greater than 2, both the rotor and stator deliver power to the grid, analogous to the supersynchronous operation in the stator-tied configuration. The operating regions for this configuration are presented in Figure 2.7. For this operation mode the stator frequency will have a range of [87.5, 125] Hz, from equation (2.2.9).

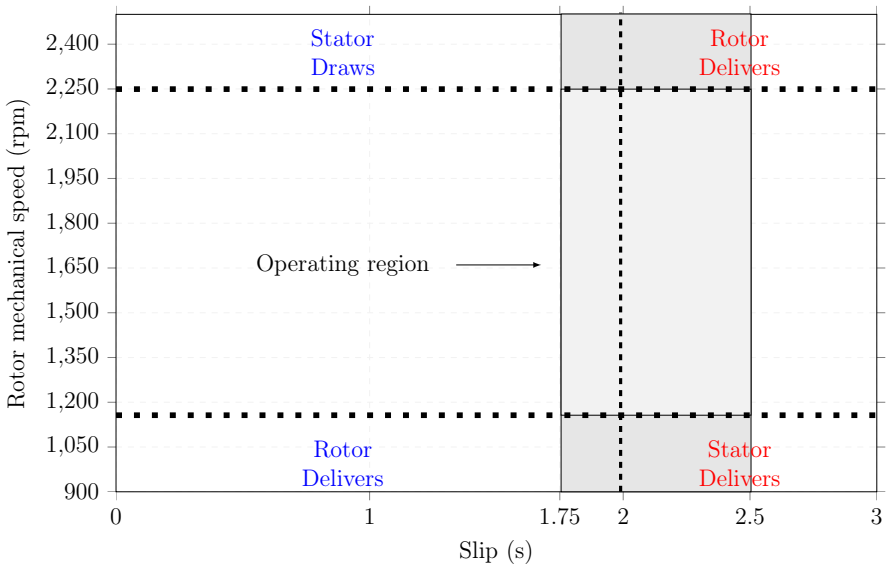

Figure 2.7: The operating region of a 50 Hz, 4 pole DFIG in the rotor-tied configuration, with the field and mechanical rotation in the same direction

A summary comparison between the stator-tied and rotor-tied configurations is presented in Table 2.1.

Table 2.1: Operating regions for the stator- and rotor-tied configurations

Stator-tied		Rotor-tied			
		Same direction		Opposite direction	
Slip	Power flow	Slip	Power flow	Slip	Power flow
$s > 0$	Stator delivers Rotor absorbs	$2.5 \geq s > 2$	Stator delivers Rotor delivers	$s < 0$	Stator delivers Rotor delivers
$s < 0$	Stator delivers Rotor delivers	$2 > s \geq 1.75$	Stator absorbs Rotor delivers	$s > 0$	Stator absorbs Rotor delivers

2.2.3 Case Study

The following section presents a short analysis of a 4 pole, 3 kW induction machine in the rotor-tied configuration. A design of a wound rotor induction machine is conducted. The design procedure is presented in Section 8.2.

The machine model is used to simulate the operation in the rotor-tied configuration.The operating regions are defined based on the principles developed in the previous section, and a number of simulated results are presented in order to verify the theoretical expressions.

The FEM software JMAG is used for the analysis. The expressions in Section 2.2.2 indicates that the operation will introduce frequencies on the stator that are higher than the grid frequency. This will affect the design and operation of the induction machine. The induction machine in the rotor-tied configuration is run at a mechanical speed of 1125 rpm, in the same direction as the field and the frequency is as predicted at 87.5 Hz as shown by Figure 2.8. The same is done at a higher speed of 2250 rpm, the frequency of 125 Hz shown in Figure 2.9 correlates with the analytical analysis value.

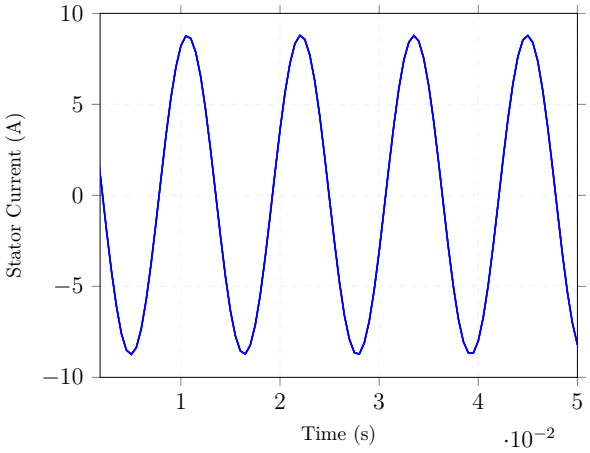

Figure 2.8: Stator current for mechanical speed of 1125 rpm in the same direction.

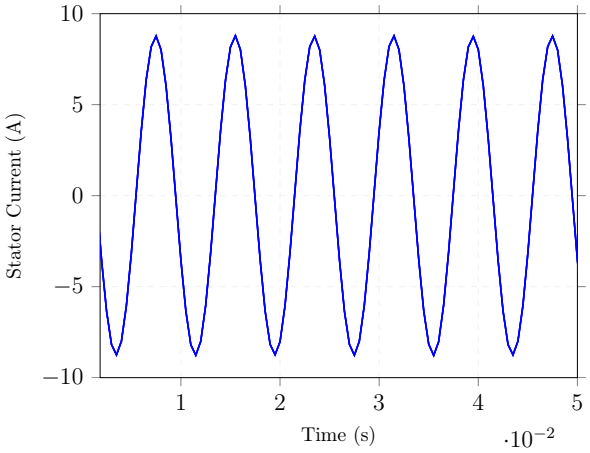

Figure 2.9: Stator current for mechanical speed of 2250 rpm in the same direction.

2.3 Summary

For application with a RT, the DFIG configuration is changed to have the rotor grid connected, while the stator is coupled to the back-to-back converter. This allows for a higher operating frequency on the rotor, and subsequently for the RT. This a beneficial feature in terms of the RT's overall size. There are two distint modes of operation for the rotor-tied DFIG: (1) The mechanical rotation and applied field are in the opposite direction and, (2) The mechanical rotation and field are in the same direction. Mode (1) is analogous to the

standard stator-tied operation region, while mode (2) introduces a new speed and frequency range that requires further investigation.

Chapter 3

Rotary Transformer Design Considerations

The RT has a number of unique properties as mentioned in Section 1.1.2. Half of the RT's core is required to rotate around the central axis. This requirement introduces an air gap between the primary and secondary sides of the transformer. This unique geometry together with the air gap leads to a more complicated transformer design. For the proposed application in a DFIG, the size and efficiency of the RT are of particular interest. In this chapter, the most important design considerations of the RT are presented. Different design aspects are explained in each section and recommendations based on current research, are given.

3.1 Power rating and transformer loadings

Similar to conventional transformers, there are two loading variables used in the RT design, the magnetic and the electrical loadings. The magnetic loading takes the form of the average operating flux density, B_o, of the core material. This value is dependent on the type of ferromagnetic material as well as the allowable core loss. Current density, J, of the windings defines the electrical loading and is similarly related to the chosen winding material and the desired conductive loss value.

The power rating of the RT is determined by the system in which it is placed. For implementation in a DFIG the RT is required to carry the rotor power of

the generator. The rated phase voltage and line current for the designed RT needs to match that of the DFIG rotor.

3.2 Loss mechanisms

The losses in the RT consist of three components: core loss, conduction losses and frictional wind loss. Core losses occur within the ferromagnetic material of the core, and take the form of hysteresis and eddy current losses. When an alternating magnetic field is applied to a material, the magnetic domains line up with this field; this is the mechanism of magnetising the core. Increasing the strength of the external magnetic field ensures that all the domains orient themselves so as to line up with the field. Once the majority of the domains in the iron are in line, increasing the strength of the external field cannot increase the flux further. This mechanism is known as saturation.

Aligning the magnetic domains requires energy, and on each cycle of alternating current energy is expended to reorientate these domains. If the flux in the core is graphed against the magnetomotive force (mmf), the result is nonlinear relationship illustrated by Figure 3.1. The non-linearity exists because the flux in the core is not only dependent on the applied current, but also on the remaining amount of flux in the core. The area enclosed by this flux curve relates directly to the amount of energy used in the magnetisation cycle, and is known as the hysteresis loss.

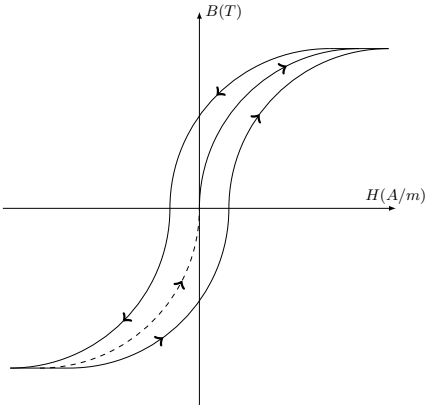

Figure 3.1: Hysteresis loop

The second source of core loss is the induced eddy currents in the material. The application of time varying electric fields in the core induces currents in the conductive core material. These currents are circular in nature and produce a flux that opposes the change in flux density. The energy lost due to eddy currents is related to the length of the current's path. In order to limit eddy current losses at low frequency operation the core is constructed out of thin laminations that are insulated from one another. Both hysteresis and eddy current losses result in heating of the core, and care needs to be exercised in order to minimise this loss.

Conduction losses in the winding present another set of losses outside of the transformer's core the winding losses are proportional to the square of the current flowing in the winding. Choosing a suitable cross sectional wire area for the rated current will keep the current density at acceptable levels, so as to minimise conduction losses.

3.3 Efficiency

In DFIGs, standard slip ring and brush assemblies offer superior efficiencies. In order for the RT to be a viable coupling, its efficiency should be comparable to that of a slip ring assembly.

Typical transformers offer high efficiencies well over 90 %. The RT's efficiency increases with an increase in power rating, a characteristic shared with standard transformers. A comparison is done between the standard and RT efficiency in [30]. As the rated power increases, the deviation in efficiency between a standard and RT with the same specifications reduces to within 2 %, as indicated by the curves in Figure 3.2.

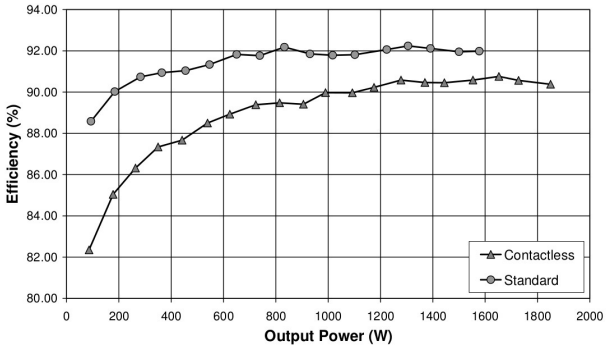

Figure 3.2: Efficiencies of standard and RT designs, as a function of rated output power [30].

The RT developed by WEG in [14] for a 90 kW DFIG yielded an high overall system efficiency of 94.8 %. This is comparable to efficiencies of a typical transformer. In order to maximise the efficiency of the RT it is necessary to keep the losses mentioned in Section 3.2 to a minimum.

3.4 RT configuration

The most obvious constraint in the design of an RT is the fact that it needs to rotate freely. This rotation should not have an effect on the RT's performance. This can be assured by maintaining a constant flux path over a full rotation. The two configurations, axial and radial, proposed by Landsman and shown in Figure 3.3(a) and Figure 3.3(c) respectively, facilitate a constant flux path [31]. The axial consists of a secondary core within a larger primary core, while in the radial the primary and secondary are face-to-face. The naming of the configurations refers to the air gap positioning. Figure 3.3(b) and Figure 3.3(d) each illustrate a 2D section of the core, showing the positioning of the cores and windings as well as indicating the flux path.

The RT requires a through-bore so that it can be mounted on a shaft. The diameter of this shaft is a decision that is based on the weight of the RT assembly as well as the shaft size of the load to which the RT will be coupled. This requirement leads to an overall larger assembly and increased mean length of turn (MLT) for the windings as can be seen in Figure 3.3. This increase in size and MLT results in the core and winding material being used inefficiently [32].

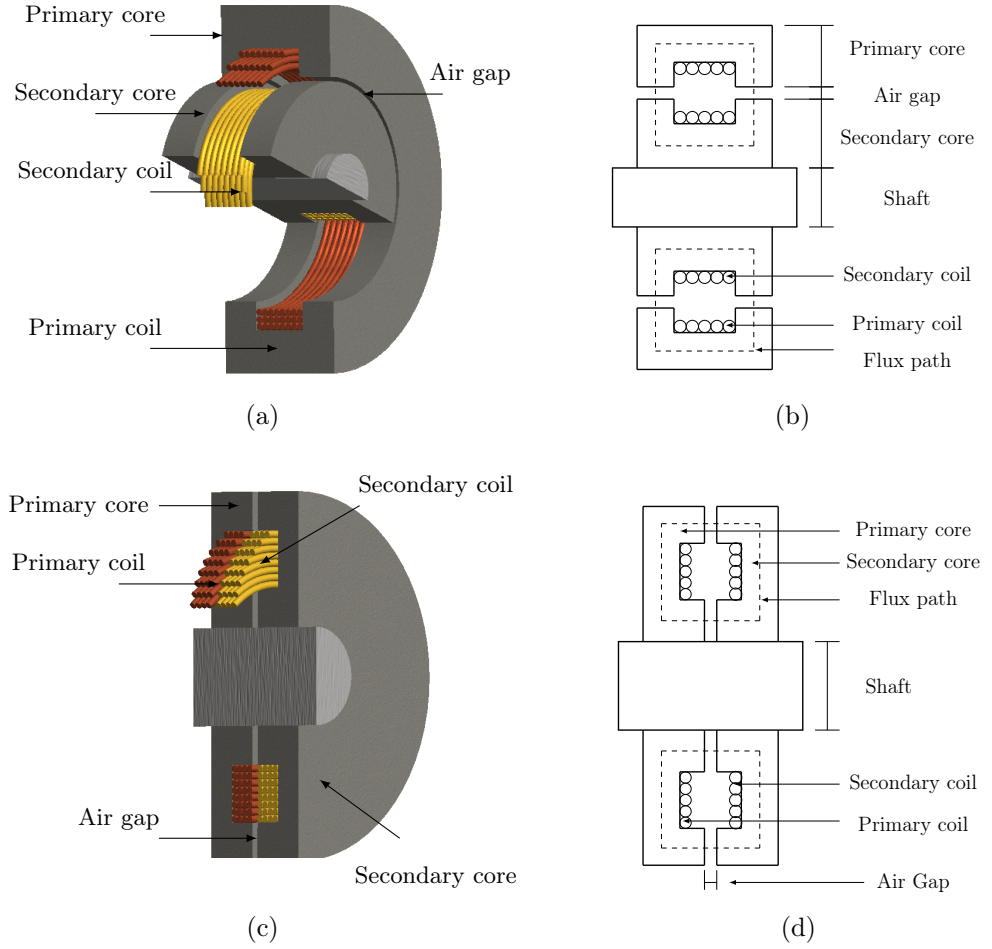

Figure 3.3: Two possible rotary transformer configurations: (a) Axial and (c) Radial. The flux paths, primary and secondary sides for each are shown in (b) and (d) respectively.

The choice of configuration is a trade-off based on the requirements and constraints of the application. Both configurations offer windings that are permanently aligned during rotation, and hence there is no additional torque applied to the shaft by the RT. The radial design does however result in an axial force being applied to the shaft due to the magnetic force existing between the two windings [15].

The best coupling between windings is offered by the axial setup, and this led to the development of an RT with a radial core, with axial windings [33], as demonstrated in Figure 3.4. This configuration takes advantage of the simplicity of the radial pot core setup and the low leakage inductance of the

axial winding.

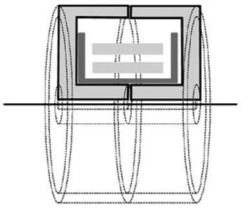

Figure 3.4: Combination of axial winding and radial core [33].

3.5 Operating frequency

For DFIG applications, the RT will have a low operating frequency: well below 50/60 Hz for a stator-tied DFIG and 50/60 Hz for a rotor-tied DFIG. This will lead to higher eddy losses due to higher eddy current flowing in the RT. Therefore, the core needs to be laminated. The lamination is dependant on the flux path in the core, as seen in Figure 3.3. The core needs to be radially laminated to curb the eddy current formation.

The difference between the outer and inner diameters of an RT with a constant lamination thickness results in a large space between laminations at the outer circumference of the core as shown by Section 3.5. This spacing leads to physically less material in the core which makes the RT more susceptible to magnetic saturation at the rated voltage. The geometric equations used to design the dimensions of the core in [14] take this spacing into account. The RT built in [23] is assembled in groups of laminations that lie flush with one another, with large air gaps between the bundles. This is done to simplify the construction, but an increase in leakage reactance is observed.

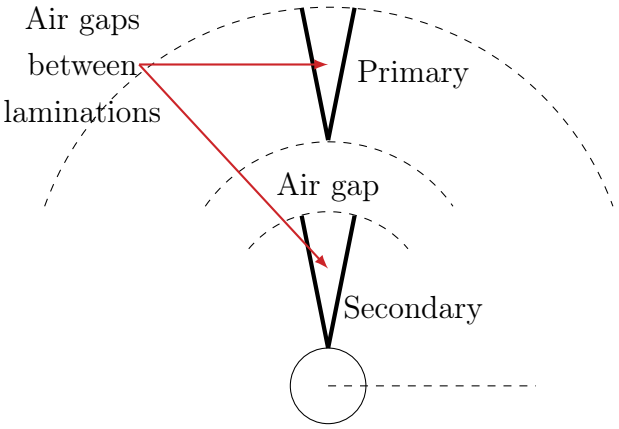

Figure 3.5: Spacing between radial laminations in the primary and secondary sides of the RT core.

3.6 Air gap

The necessary air gap between the primary and secondary core introduces a number of changes to the RT's characteristics and operation. The two main effects of this air gap are low magnetising inductance and high leakage inductance.

The cause of the lowered magnetising inductance is the inversely proportional relationship between inductance and the magnetic reluctance of the core. The reluctance of a magnetic flux path is dependent on the length (l) and the area (A) of the path as well as its relative permeability (μ_r) such that,

$$\mathcal{R} = \frac{l}{\mu_0 \mu_r A}. \tag{3.6.1}$$

The inductance, L, is a function of this reluctance and the square of the turn number, N, yielding,

$$L = N^2 \frac{1}{\mathcal{R}}. \tag{3.6.2}$$

From (3.6.1) and (3.6.2), it is clear that the reluctance of the air gap is much higher than that of the core, due to the low permeability of air, and this higher reluctance results in a lower inductance. The magnetising current will increase

as a result.

The effect described above can be observed by evaluating the simplified BH curves of the RT shown in Figure 3.6. The air gap affects the slope of the BH curve. The slope of the curve represents the relationship between the magnetic field intensity and the flux density. As the gap length increases the slope of the graph decreases, and this indicates that a larger magnetising current is needed to maintain the same flux in the core [26].

The geometry of the core also results in a larger separation between the primary and secondary windings. This separation results in a higher leakage inductance. From the study conducted in [33], the magnetising and leakage inductances are graphed as a function of the air gap length, shown in Figure 3.7. The important characteristic to note is that the magnetising inductance is affected by the change in air gap, while the leakage inductance is only a function of the separation of the windings and Figure 3.7 exhibits only a slight variation as the air gap increases.

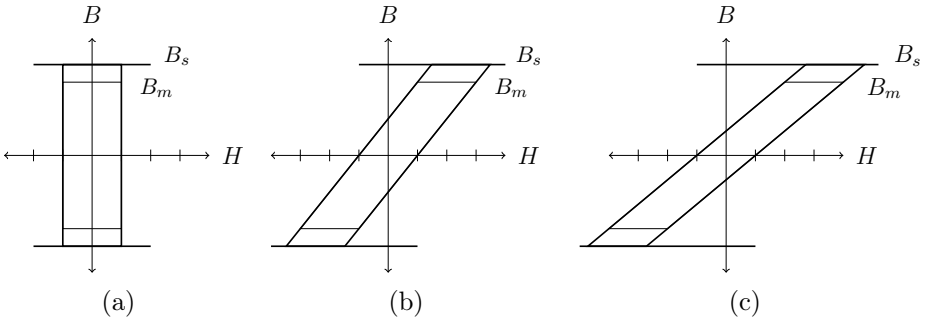

Figure 3.6: The effect of the air gap on the BH curve of the core material: (a) The BH curve for an ideal transformer, (b) and (c) exhibiting a more gradual BH curve as the air gap length increases [26].

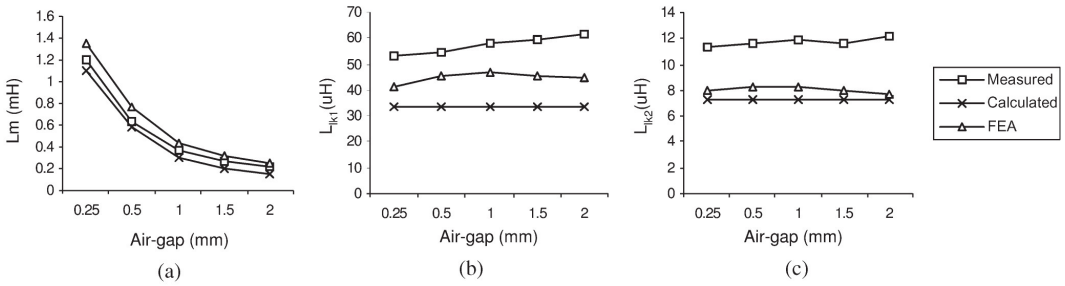

Figure 3.7: Effect of the air gap length on a) Magnetising inductance, b) Primary leakage inductance and c) Secondary leakage inductance for an adjacent pot core transformer. [33]

3.7 Effect of rotation

Both the RTs in [25, 30] were tested under stationary and rotating operation.

The curve in Figure 3.8(a) shows that the measured magnetising inductance remains relatively constant for the full rotation. This result is to be expected as long as the RT is properly constructed so that the air gap length is maintained throughout.

The measured leakage inductance is more affected by the rotation. The minimum leakage occurs when the coils are the most effectively coupled. For the RT developed in [30] this coupling occurs when the end windings of both coils line up. On the contrary, inspection of the curve in Figure 3.8(b), shows the maximum leakage of the RT in [25] was measured at the start point. This

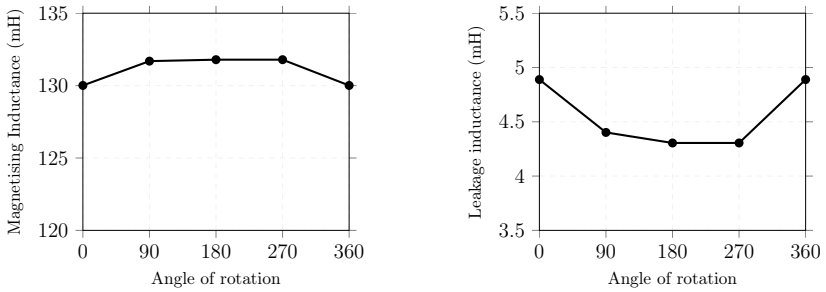

Figure 3.8: Effect of rotation on (a) Magnetising and (b) Leakage inductance

point is where the coils line up. This unexpected result is largely due to the manner in which the end winding was removed from the coil. From this it is clear that the maximum coupling point is largely dependant on the specific RT's windings and construction.

3.8 Size

The nacelle of the wind turbine has a limited amount of space and weight restrictions. The RT needs to have a high power density so that the size is suitable for this application.

As mentioned in Section 3.5 the geometry of the RT leads to a non optimal use of core material, especially in the case of low frequency operation which requires laminated cores. However, the main hindrance in terms of size is the low operating frequencies required in the DFIG application. The size of a transformer is inversely proportional to the frequency. This has made the RT favourable in the high frequency applications in [27, 28, 30, 33–36]. The proposed solution is to raise the operating frequency of the RT by operating the DFIG in the rotor-tied configuration has been presented in Chapter 2.

3.9 Summary

This chapter highlights the important design aspects of the RT. Good efficiencies can be achieved, so long as the loss mechanisms are addressed, specifically the higher conduction losses. The introduction of an air gap results in a higher magnetising inductance of the RT core, consequently raising the magnetising current and increasing conduction losses. The magnetising inductance is constant during rotation provided that the air gap length remains constant. Increased separation between primary and secondary windings results in a higher leakage inductance which varies during rotation. Both the magnetising and leakage inductance adverse affects can be minimised by use of a suitably small air gap length.

The alignment of the cores in the axial configuration ensures that no additional forces are applied on the shaft. The combination between the round geometry and the need for a laminated core results in a non-optimal use of material, air

gaps between the laminations and a complicated mechanical assembly. Operation of a RT at low frequency results in a larger required core area. However, the frequency can be raised by using the DFIG in the rotor-tied configuration.

Chapter 4

Analytical Model of Rotary Transformer

During the design procedure, it is necessary to develop an accurate analytical model of the RT. The geometry of the RT introduces a number of unique characteristics, as discussed in Chapter 3. A properly developed model allows for a good prediction of performance, and results in an improved analysis and simulation of the machine.

The chosen method to develop the model for the RT is the widely used, duality principle. The basis of this principle is the ability to represent a magnetic circuit as an equivalent electrical circuit. The flux paths in the RT are identified and a reluctance model is then built. This reluctance network is converted into an electrical model from which certain parameters can be defined. For the RT, as mentioned in Section 3.6, the two areas of concern are the leakage and magnetising inductances. In the following chapter an axial RT model is developed to evaluate these inductances.

4.1 RT Equivalent Circuit

The RT can be modelled using the standard transformer equivalent circuit shown in Figure 4.1. The following sections detail the process for determining each of these equivalent circuit components.

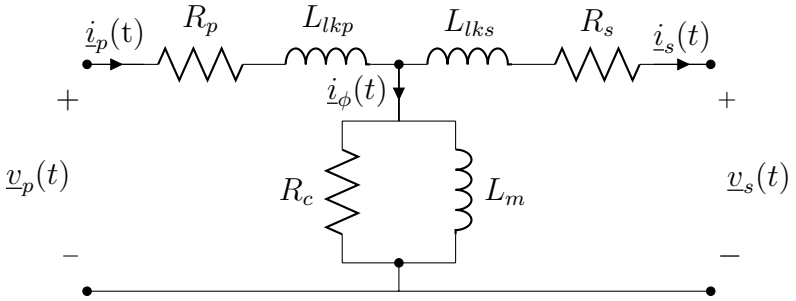

Figure 4.1: RT equivalent circuit

4.1.1 Winding resistances

The simplest components to determine are the winding resistances. The primary and secondary resistances, R_p and R_s, can be calculated using the properties of each coil, so that,

$$R_p = \frac{N_p l_p \rho}{A_{wp}}, \tag{4.1.1}$$

$$R_s = \frac{N_s l_s \rho}{A_{ws}}; \tag{4.1.2}$$

where, N_p and N_s are the number of primary and secondary turns, l_p and l_s are primary and secondary winding MLT, ρ is the material resistivity, and A_{wp} and A_{ws} are the cross sectional conductor areas of the primary and secondary winding respectively.

4.1.2 RT Inductances

Calculating leakage inductances, L_{lkp} and L_{lks}, as well as the magnetising inductance L_m, is more involved and requires the use of a magnetic circuit derived from first principles.

In a transformer Faraday's law can be used to determine the induced voltage as a function of the number of turns, N_p, and the flux ϕ, that is,

$$e_{ind} = N_p \frac{d\phi}{dt}. \tag{4.1.3}$$

The magnetomotive force (mmf) applied to the core is given by the ampere-turn product. This is a function of the magnetic field intensity, $\underline{H}$, and the element of length along the path of integration, $\mathrm{d}l$, given by,

$$\underline{\mathcal{F}} = N_p \underline{i} = \int \underline{H}\, \mathrm{d}l. \tag{4.1.4}$$

where $\underline{\mathcal{F}}$ is the mmf, N_p is the primary winding's number of turns and $\underline{i}$ is the current in the conductor.

The total flux enclosed in an area, A, is

$$\phi = \int B\, \mathrm{d}A. \tag{4.1.5}$$

where B is the flux density. If this flux density is assumed constant throughout the area, then equation (4.1.5) can be reduced to

$$\phi = BA. \tag{4.1.6}$$

The mmf is analogous to the voltage source in an electric circuit, as it is the source of the flux. The relationship between mmf and flux is

$$\underline{\mathcal{F}} = \phi \mathcal{R}, \tag{4.1.7}$$

where $\mathcal{R}$ is the reluctance of the magnetic path and is the magnetic equivalent of the resistance of the circuit and given by,

$$\mathcal{R} = \frac{l}{\mu A}. \tag{4.1.8}$$

with μ being the permeability of the material, while l is the length of the magnetic path and A is area of the path respectively.

The inductance of a winding can in general be expressed as,

$$L = \frac{N^2}{\mathcal{R}}. \tag{4.1.9}$$

where N is the number of turns in the winding, and $\mathcal{R}$ is the reluctance of the magnetic circuit. Applying this principle to the self inductance of the primary winding, L_{11}, it is shown to be proportional to the square of the

primary winding number of turns, N_p and inversely proportional to the total reluctance of the circuit, $\mathcal{R}_{total}$, such that,

$$L_{11} = \frac{N_p^2}{\mathcal{R}_{total}}. \tag{4.1.10}$$

Not all the flux developed in the primary winding passes through to the secondary winding. The developed flux can be expressed in two separate parts. The flux which links both windings is known as the mutual flux, ϕ_m, and the leakage flux is that which links only its own coil. The total flux in each winding can then be given by,

$$\phi_p = \phi_m + \phi_{lp}, \tag{4.1.11}$$

$$\phi_s = \phi_m + \phi_{ls}. \tag{4.1.12}$$

where ϕ_{lp} and ϕ_{ls} are the primary and secondary leakage fluxes respectively. With primary and secondary winding's number of turns N_p and N_s respectively, the flux linkages can be expressed as,

$$\lambda_p = N_p\phi_m + N_p\phi_{lp}. \tag{4.1.13}$$

$$\lambda_s = N_s\phi_m + N_s\phi_{ls}. \tag{4.1.14}$$

Considering the circuit in Figure 4.1, the terminal voltages can be expressed as a function of the inductances and resistances,

$$\begin{bmatrix} \underline{v}_p(t) \\ \underline{v}_s(t) \end{bmatrix} = \begin{bmatrix} L_{11} & L_{12} \\ L_{21} & L_{22} \end{bmatrix} \frac{d}{dt} \begin{bmatrix} \underline{i}_{p(t)} \\ \underline{i}_{s(t)} \end{bmatrix} + \begin{bmatrix} R_p \\ R_s \end{bmatrix} \begin{bmatrix} \underline{i}_{p(t)} \\ \underline{i}_{s(t)} \end{bmatrix} \tag{4.1.15}$$

where L_{11} and L_{22} represent the self inductance of the primary and secondary windings respectively. $L_{12} = L_{21}$ and represents the mutual inductance between the windings. R_p and R_s are the primary and secondary winding resistances respectively.

The self inductances of the primary and secondary windings above are divided into two components: magnetising and leakage inductances. These are the actual inductances modelled in the equivalent circuit in Figure 4.1 as L_m and L_{lkp} or L_{lks}. The self inductances can be written as the sum of these two components,

$$L_{11} = L_{mp} + L_{lkp}, \tag{4.1.16}$$

$$L_{22} = L_{ms} + L_{lks}. \tag{4.1.17}$$

The magnetising inductance component, L_m, is proportional to the energy needed in order to magnetise the RT's core. L_{mp} refers to the magnetising inductance when the transformer is magnetised from the primary and likewise L_{ms} when magnetised from the secondary. The mutual inductance, L_{12} is the portion of this flux that links both windings. This inductance is a function of the number of primary and secondary turns as shown by,

$$L_{mp} = \frac{N_p}{N_s} L_{12}. \tag{4.1.18}$$

The magnetising and leakage inductances need to be computed in order to complete the equivalent circuit in Figure 4.1. The magnetising inductance can be determined by calculating the necessary reluctances, and the leakage inductance is calculated as the energy stored in the windings and the air gap. The procedure for both is outlined in the following sections.

4.1.2.1 Magnetising Inductance

The inductances introduced in the previous section can be calculated based on the reluctances of the magnetic circuit. Figure 4.2(b) shows the reluctance network of an axial RT.

From the network displayed in Figure 4.2(b) and the principle introduced in equation (4.1.9), the magnetising inductance as seen from the primary side, L_{mp}, can be calculated as,

$$L_{mp} = \frac{N_p^2}{\mathcal{R}_{p1} + \mathcal{R}_{p2} + \mathcal{R}_{p3} + \mathcal{R}_{g1} + \mathcal{R}_{g2} + \mathcal{R}_{s1} + \mathcal{R}_{s2} + \mathcal{R}_{s3}}. \tag{4.1.19}$$

As shown in Figure 4.2(b), the core is separated into sections and each has a reluctance that is function of its length, cross sectional area and permeability. For a standard transformer the cross sectional area is rectangular and the geometry is simple. The unique nature of the RT's core means that the geometric equations governing the cross sectional area have to be carefully evaluated. A

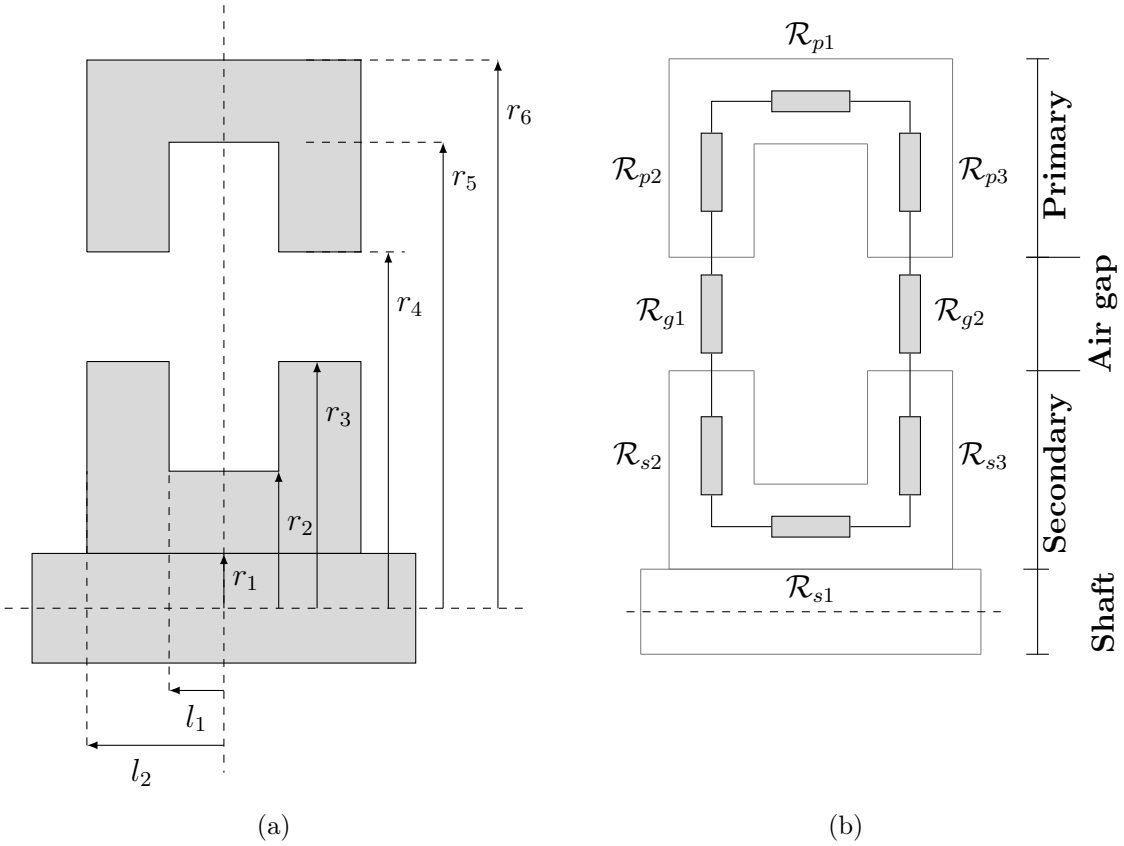

Figure 4.2: Axial transformer model. (a) Geometry of the core and (b) Reluctance network.

3D section of the RT's core is shown in Figure 4.3(a).

The arrows indicate the direction of the flux flowing in the core. When the flux is flowing axially, in sections (1) and (3), the core cross sectional area is characterised by a ring shape as shown in Figure 4.3(b). Section (2) represents radial flux moving through the air gap and the legs of each core half. The cross sectional area in this region is rectangular with geometry as shown by Figure 4.3(c).

The geometry is evaluated using cylindrical coordinates due to the RT's shape. The cylindrical axis is indicated in Figure 4.3(a), where r is the radial component, z is the axial component and θ is the angle of rotation about the z axis.

The areas inscribed by the circular cross section in Figure 4.3(b) are a function

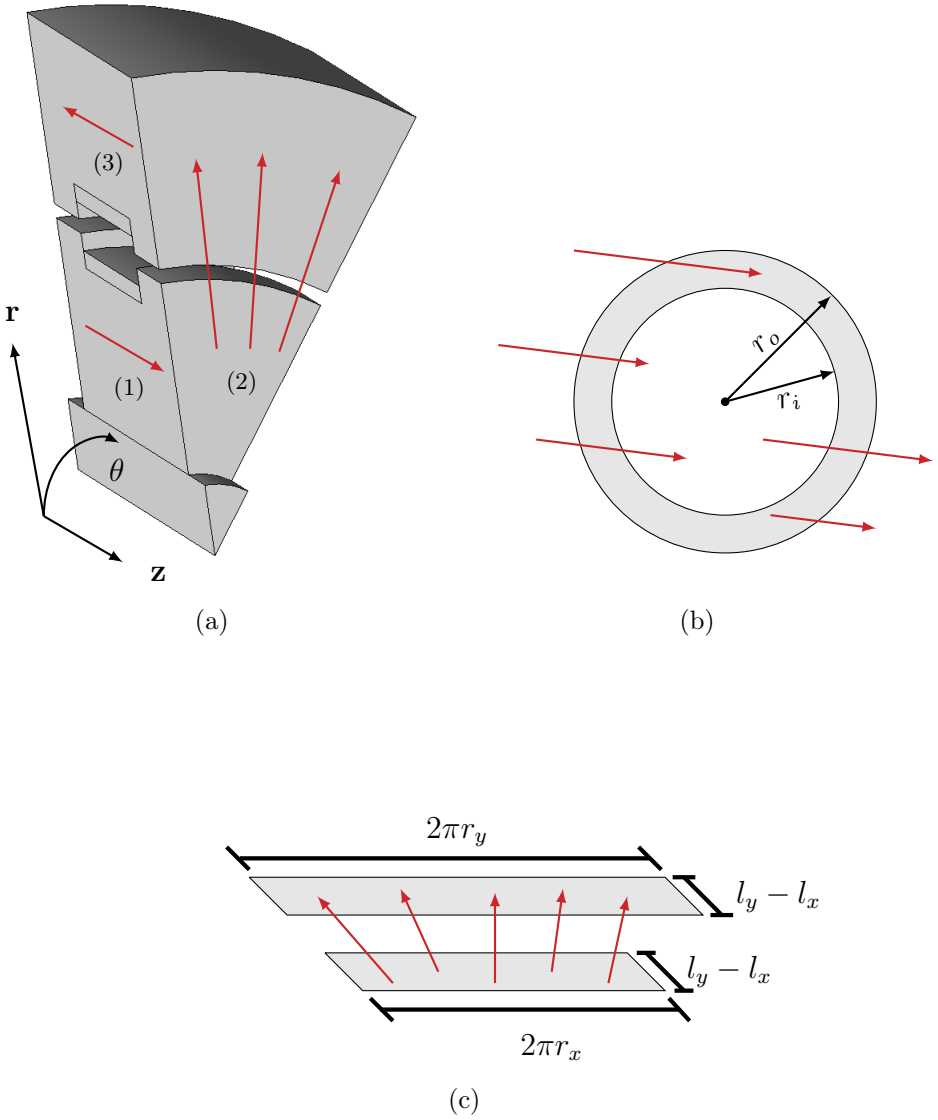

Figure 4.3: Representation of the flux path direction in the RT. (a) 3D section of the core indicating (1) the path parallel to the shaft, in the secondary, (2) the radial path across the air gap and (3) the path in the primary that runs parallel to the shaft. (b) 2D cross section of regions (1) and (3). And (c) 2D cross section of region (2).

of the primary and secondary yoke radii (shown in Figure 4.2(a)) and is given by

$$A_{p1} = \pi(r_6^2 - r_5^2), \tag{4.1.20}$$

$$A_{s1} = \pi(r_2^2 - r_1^2). \tag{4.1.21}$$

The corresponding primary and secondary yoke reluctances are as shown in Figure 4.2(b). These reluctances can be calculated using equation (4.1.8) with equation (4.1.20) and equation (4.1.21) to yield,

$$\mathcal{R}_{p1} = \frac{2l_1}{\mu_r \mu_0 \pi(r_6^2 - r_5^2)}; \tag{4.1.22}$$

$$\mathcal{R}_{s1} = \frac{2l_1}{\mu_r \mu_0 \pi(r_2^2 - r_1^2)}. \tag{4.1.23}$$

where μ_r is the relative permeability of the iron core and μ_0 is the permeability of air.

The radial reluctance components, $\mathcal{R}_{p2}$, $\mathcal{R}_{p3}$,$\mathcal{R}_{s2}$ and $\mathcal{R}_{s3}$ have cross sectional areas as represented in Figure 4.3(c). Evaluation of the core section in Figure 4.3(a) indicates that for flux in the radial direction, the core area changes as a function of the radius r. This variation in area needs to be taken into account when calculating the radial reluctances. The modelling method proposed in [37] uses the standard triple integral expression for the volume of a cylinder. The enclosed volume, in cylindrical components, is then,

$$Volume = \int\int\int r \, \mathrm{d}r\mathrm{d}\theta\mathrm{d}z. \tag{4.1.24}$$

In terms of area, equation (4.1.24) becomes,

$$Area = \frac{\int\int\int r \, \mathrm{d}r\mathrm{d}\theta\mathrm{d}z}{length}. \tag{4.1.25}$$

The change in geometry for the radial region (2) is indicated in Figure 4.3(c). Evaluation of equation (4.1.25) for an angle of rotation θ_1 to θ_2, change in radius from r_x to r_y and axial length of l_x to l_y, yields:

$$A_x = \frac{\int_{l_x}^{l_y} \mathrm{d}z \int_{\theta_1}^{\theta_2} \mathrm{d}\theta \int_{r_x}^{r_y} r \,\mathrm{d}r}{r_y - r_x}. \tag{4.1.26}$$

The integrals in equation (4.1.26) are evaluated for the radial sections of the RT with primary radial reluctances of $\mathcal{R}_{p2}$ and $\mathcal{R}_{p3}$. The geometry of these radial sections is indicated in Figure 4.2. The corresponding areas of these radial sections are A_{p2} and A_{p3}, and can be calculated with the use of equation (4.1.26) to give,

$$A_{p2} = A_{p3} = \frac{(l_y - l_x)(2\pi)(1/2(r_y^2 - r_x^2))}{(r_y - r_x)}. \tag{4.1.27}$$

Using the geometry shown in Figure 4.2(a), equation (4.1.27) resolves to:

$$A_{p2} = A_{p3} = \frac{\pi(l_2 - l_1)(r_5^2 - r_4^2)}{(r_5 - r_4)}. \tag{4.1.28}$$

Similarly for the radial regions in the secondary core, $\mathcal{R}_{s2}$ and $\mathcal{R}_{s3}$,

$$A_{s2} = A_{s3} = \frac{\pi(l_2 - l_1)(r_3^2 - r_2^2)}{(r_3 - r_2)}. \tag{4.1.29}$$

Using the resultant areas, together with equation (4.1.8), gives the following reluctances for the radial sections:

$$\mathcal{R}_{p2} = \mathcal{R}_{p3} = \frac{(r_5 - r_4)}{\mu_r \mu_0 \pi (l_2 - l_1)(r_5 + r_4)}, \tag{4.1.30}$$

and

$$\mathcal{R}_{s2} = \mathcal{R}_{s3} = \frac{(r_3 - r_2)}{\mu_r \mu_0 \pi (l_2 - l_1)(r_3 + r_2)}. \tag{4.1.31}$$

The method proposed in [37] consists of including the fringing field into the air gap calculation. The result is not completely accurate, but attempts to model

the effects of fringing flux. The technique used increases the area of the air gap to account for fringing. This is done by adding the length of the air gap to either side of the air gap region, so that:

$$l_2' = l_2 + l_{gap} = l_2 + (r_4 - r_3). \tag{4.1.32}$$

The air gap reluctance with adjusted area is now given by:

$$\mathcal{R}_{g1} = \mathcal{R}_{g2} = \frac{(r_4 - r_3)}{\mu_0 \pi (l_2' - l_1)(r_4 + r_3)}. \tag{4.1.33}$$

The model needs to be further developed to take into account the effect of the non-ideal tangential laminations. The spaces between the rotor laminations at the air gap result in an overall larger air gap. This is modelled by updating equation (4.1.33) so that the length of the path through the air gap, along with the area, is increased by the air gap length to give:

$$\mathcal{R}_{g1} = \mathcal{R}_{g2} = \frac{2(r_4 - r_3)}{\mu_0 \pi (l_2' - l_1)(r_4 + r_3)}. \tag{4.1.34}$$

It is also necessary to model the air gaps between the laminations in order to get an accurate value for the magnetising inductance. This can be done by using an adjusted stacking factor for the core. Stacking factor is a measure of the percentage of active material in a defined region.

On the secondary side of the RT, the laminations are closest together at the shaft and more spread out at the air gap. The opposite is true for the primary, where the air gap is the inner radius and here the laminations lie flush, spreading out towards the outer radius as shown in Figure 4.4. The stacking factor for each of the regions is calculated by,

$$Stacking factor = \frac{actual\ area\ filled\ by\ lamination}{theoretical\ area\ of\ the\ region}. \tag{4.1.35}$$

Once the geometry of the RT is set and the lamination thickness chosen, the stacking factor evaluation can be done. The factor is then applied to the area calculation of the region, thereby decreasing the active area to account for the air gaps between laminations.

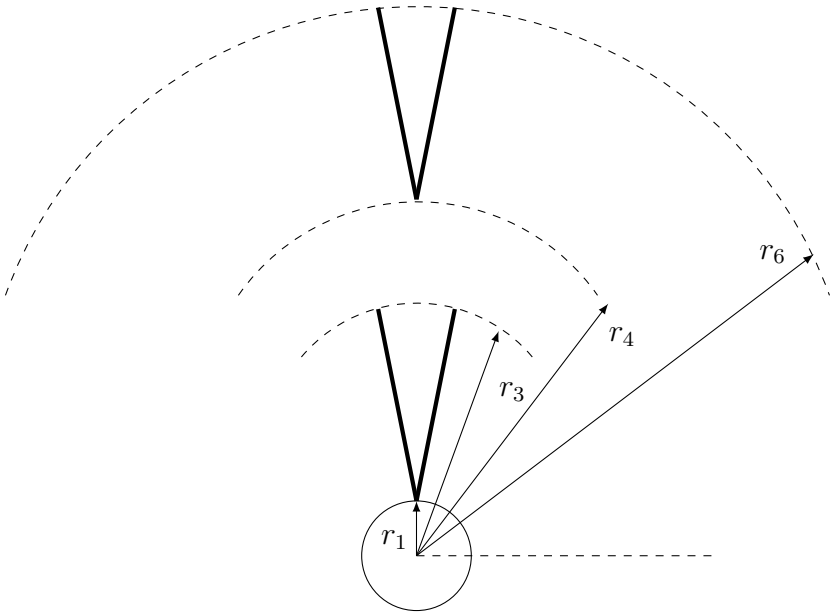

Figure 4.4: Air gap spacing between laminations in the primary and secondary sides of the RT core.

4.1.2.2 Leakage Inductance

The leakage flux lines in the RT are not known, and so modelling with reluctances results in inaccuracies. For that reason, the leakage inductance can be calculated as the amount of energy stored in the windings and the air gap [32]. The energy stored, W_m, can be determined by evaluating the field intensity $\underline{H}$ and flux density, B, within a volume v, such that,

$$W_m = \int \frac{1}{2}\underline{H}B \, \mathrm{d}v, \tag{4.1.36}$$

and equation (4.1.36) can be expressed as a function of the leakage inductance, L_{lk}, so that,

$$W_m = \frac{1}{2}L_{lk}\underline{i}(t)^2, \tag{4.1.37}$$

where $\underline{i}(t)$ is the current flowing through the winding.

Evaluating the leakage field from the perspective of the primary side, the field intensity in the air gap can be given as

$$\underline{H}_g = \frac{N_p \underline{i}_p(t)}{l_{gap}}, \tag{4.1.38}$$

where l_{gap} is the length of the air gap. Using the geometry as presented in Figure 4.2 the air gap field intensity is

$$\underline{H}_g = \frac{N_p \underline{i}_p(t)}{(r_4 - r_3)}. \tag{4.1.39}$$

In the windings themselves, the length of the coils effects the field intensity, so that the axial (z-direction) field intensity in the primary is given by,

$$\underline{H}_p(z) = \frac{N_p \underline{i}_p(t)}{2l_1} \frac{z}{(r_5 - r_4)}. \tag{4.1.40}$$

A similar expression can be given for the secondary winding;

$$\underline{H}_s(z) = \frac{N_s \underline{i}_s(t)}{2l_1} \frac{z}{(r_3 - r_2)}. \tag{4.1.41}$$

Once all the field intensities are known, the leakage inductance can be calculated. Assuming there is no saturation,equation (4.1.36) can be re-evaluated for the average energy stored, so that

$$W_m = \frac{1}{2}\mu_0 \underline{H}^2 \cdot v, \tag{4.1.42}$$

where $\underline{H}$ is the field intensity and v refers to the volume in which the field exists.

Combining all the field intensities, equation (4.1.39)-equation (4.1.41), and substituting into equation (4.1.42), the total energy stored is found. This expression is then substituted into equation (4.1.37) to yield the leakage inductance,

$$L_{lkp} = \frac{\pi(r_5 + r_2)N_p^2}{2l_2}\left[(r_4 - r_3) + \frac{(r_5 - r_4) + (r_3 - r_2)}{3}\right]. \tag{4.1.43}$$

4.2 Summary

An analytical model is developed for an axial RT in this chapter. The standard transformer equivalent circuit is used as starting point. The winding resistances are simple to evaluate as a function of the winding dimensions and resistivity. Reliable modelling of the magnetising and leakage inductances of the RT is imperative during the design to prevent the adverse affects thereof. The procedure followed is based on the duality principle, such that the magnetic circuit can be used to determine the necessary inductances. During the calculation of these inductances the non idealities introduced by the air gap are modelled, along with the air gaps present between the laminations of the core.

Chapter 5

RT Design

The designed RT configuration consists of three separate axial RTs on a common shaft. The assembly's shaft is connected to the shaft of the induction machine. The windings are connected between the two, and each RT unit handles a single phase from the induction machine. This topology is shown in Figure 5.1.

The basic operating principle of an RT is inductive power transfer, just like a standard transformer. Therefore, the design process of the RT can be based on conventional transformer design techniques. The RT has certain unique characteristics that affect its operation. The most obvious of these is the difference in geometry related to the fact that the RT is required to rotate. The consequential air gap also affects the operation of the RT, and these issues

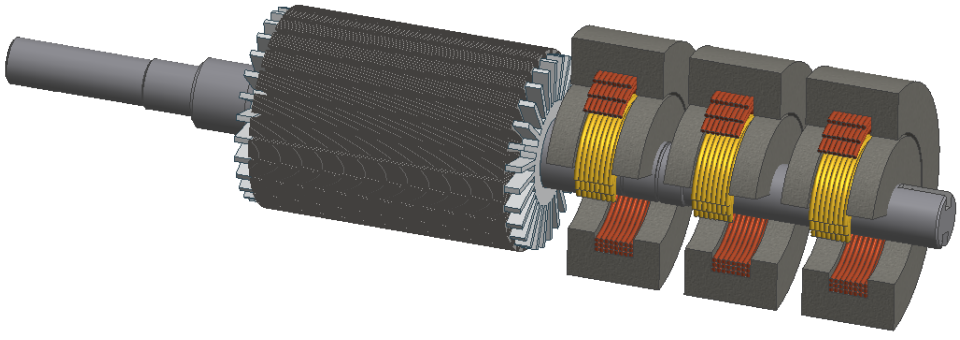

Figure 5.1: Three phase RT assembly alongside the induction machine rotor.

need to be addressed during the design process. The initial study conducted in [25] seeks to design a RT prototype and evaluate the effects of an air gap in the core. In the study, the design procedure for a standard transformer is followed. While the study highlights the considerations to be made for the RT application, no clear mitigation methods are put in place for these effects. The outcome of the study highlights key areas that need to be addressed during the design phase, namely:

- Low magnetising inductance due to air gap
- High leakage inductance due to separation of windings
- Apparent saturation of core material
- Non-optimal size

Thorough investigation has been conducted into the cause and effects of the first two nonidealities mentioned above, as shown in Chapter 3.

The following sections presents an analytical design methodology for a RT with the purpose of incorporating mitigation factors into the design process. Using the methodology presented, a short study of the RT's suitability for application in larger machines is conducted. A prototype RT is then designed for application with a 3 kW induction machine, to verify the design methodology and evaluate the RT's performance.

5.1 Outline of Optimal RT Design

The two governing constraints of the transformer's suitability to replace slip ring and brush assemblies are size and efficiency. The analytical design methodology presented in this section is based on simultaneously minimising the size and maximising the efficiency of the RT. The framework of the method is based on conventional transformer design and optimisation strategies and additional steps are incorporated that govern the new constraints. It is imperative to evaluate the design's parameters as well as the effects of the air gap during the design procedure. This is done with the use of an equivalent model, developed

in Chapter 4, as well as Finite Element Method (FEM) analysis.

In order to develop a strategy for minimising the size of the RT, the design parameters that affect the size need to be identified. For this purpose, the transformer's area product, A_p is used. The area product is a representation of a transformer's power handling capability, and is defined as the product of the core cross sectional area, A_c and the window area, A_w. The required area, in cm^4, for a transformer with a certain power rating and loadings is,

$$A_p = \frac{P_t(10^4)}{K_f K_u B_o J f}, \tag{5.1.1}$$

where P_t is the apparent power, K_f is the waveform coefficient (4.44 for sine wave), K_u is the window utilisation factor, B_o is the operating flux density, J is the current density and f is the frequency.

From equation (5.1.1) it is clear that for a transformer with a given power rating, the size is inversely proportional to the magnetic and electric loadings (B_o and J), as well as the operating frequency. Since the RT is connected to the rotor of the DFIG, the rotor-tied configuration results in a RT with operating frequency of 50 Hz instead of the low slip frequency of $(2-5)\%$ of rated frequency. This leads to a reduction in the overall size of the RT. It is important to note that in the rotor-tied configuration the RT needs to be rated for the full electrical power. In the original stator-tied configuration it would only be required to transfer about a third of the mechanical power. The alternative DFIG topology is discussed further in Chapter 2.

The underlying principle of maximising the transformer's efficiency is based on a method described in [38], whereby a flux density operating point is chosen such that both core and copper losses are minimised. Figure 5.2 illustrates the copper and core losses as a function of flux density, for both low (50 Hz) and high (50 kHz) frequencies. For low and high operating frequencies there exists a point with minimum total losses; Point A at high frequencies and point B for low frequencies. However, it is often the case that this minimum loss point corresponds to a flux density value that is above that saturation flux density of the core material. If this is the case, the method proposed by Hurley in [38] is to choose the operating flux density at point C so that it is equal to the material's saturation flux density, the highest suitable value. Depending on the

loading of the transformer this point can be adjusted to a lower flux density, such as point E, if necessary. However, this will lead to an increase in losses as seen in Figure 5.2.

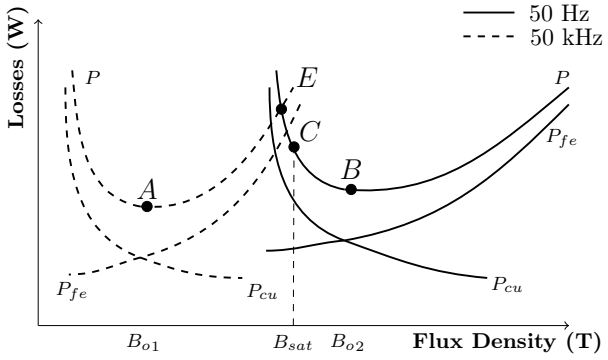

Figure 5.2: Iron and copper losses at different frequencies and the corresponding optimal flux densities, figure regenerated from [38].

5.2 Design Methodology

The following section presents an analytical design methodology for an RT of minimum size and maximum efficiency. The flow chart in Figure 5.3 represents the main stages of the design, and the following sections provide details for each stage.

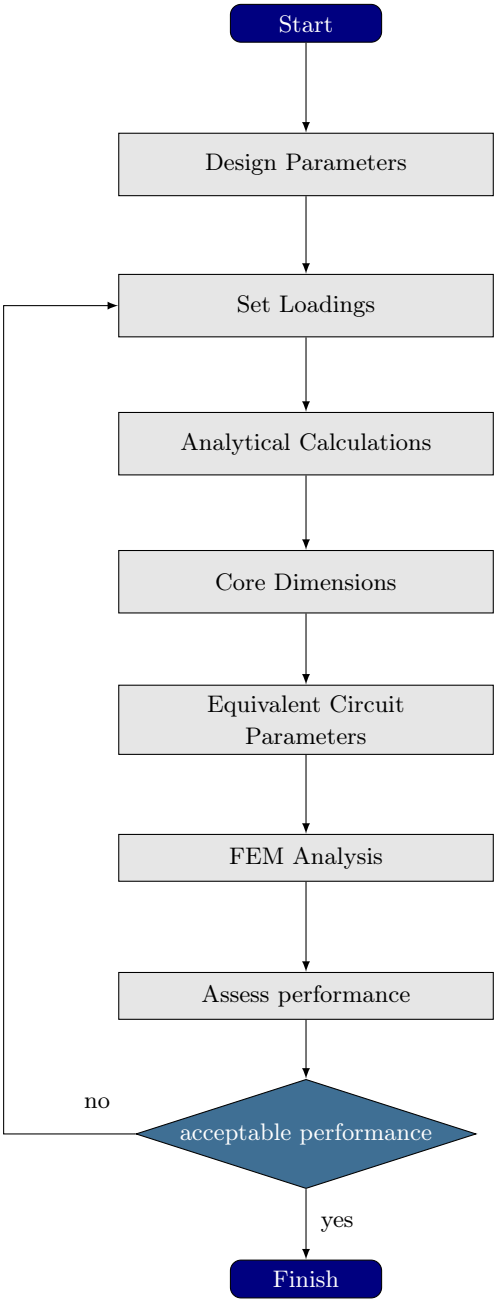

Figure 5.3: Flow chart illustrating the RT design outline

5.2.1 Design parameters and loadings (Step 1 & 2)

The design procedure starts with identifying the transformer's desired rating and parameters. The power rating is based on the full rated value of the induction machine that the RT would typically be connected to.

Initially, the loadings are set to a maximum. This results in the minimum RT size as can be seen from equation (5.1.1). As discussed in Section 5.2.1, the loadings determine the efficiency of the transformer. To keep within the acceptable range of efficiency, the maximum current density is typically set to be in the region 4 - 6 A/mm^2. The principle outlined in Section 5.1 calls for the maximum magnetic loading to equal the saturation flux density. The steps that follow are an iterative process of lowering the loadings until an acceptable efficiency is achieved. This results in a balance between minimum size and maximum efficiency. The results of the studies presented in Section 3.3 indicate that an efficiency of over 90 % is achievable for an RT. This will help in the selection of the minimum efficiency constraint for the design.

5.2.2 Analytical calculations (Step 3)

Once the main design parameters are set and the loadings are chosen, analytical design methods are used to determine the remaining variables.

Substituting the fixed design parameters into equation (5.1.1), the required area product (A_p) can be calculated. This value can be written as,

$$A_p = A_c A_w, \tag{5.2.1}$$

so that A_p is the product of the core area A_c and window area A_w. Both of these dimensions are unknown and it is necessary to use an approximation to set one of the constraints. The empirical relationship presented in [39] gives a ratio between emf/turn (E_t) and the output power(P_o) for a set of standard transformer types, that is,

$$E_t = K\sqrt{P_o}, \tag{5.2.2}$$

where K = 1.0 - 1.2 for a single phase shell type transformer. Although this is not the most accurate method, it provides a reasonable starting point for the design. Substituting the emf/turn value into the rearrangement of Faraday's law, given by,

$$A_c = \frac{E_t}{B_o f K_f}, \tag{5.2.3}$$

the core area (A_c) can be calculated. The window area is then obtained by

dividing the area product by the calculated core area. The primary number of turns can be calculated as,

$$N_p = \frac{V_p}{A_c B_o f K_f}. \tag{5.2.4}$$

The secondary number of turns is determined by the desired turn ratio,

$$\frac{V_p}{V_s} = \frac{N_p}{N_s}. \tag{5.2.5}$$

Once the number of turns has been set, there exists enough information to set the dimensions of the RT.

5.2.3 Core dimensions (Step 4)

There are two main constraints that need to be addressed when deciding on the geometry of the transformer, namely; the air gap and the separation of windings.

The findings in Section 3.6 show that the air gap has to be as small as practically possible, so as to maximise the magnetising inductance. A minimum air gap length is also beneficial in terms of winding separation. However, the main factor of windings separation is the window geometry. If the window is narrow and deep, overall the windings are further apart and the leakage inductance will be high. It is therefore beneficial to design the window in such a way that it is far wider than it is deep, ie: have less layers each with more number of turns.

The RT's core is constructed using flat laminations placed radially along the shaft. The result is less active material at the outer diameter of the core. The discontinuity needs to be factored in during the design. This is addressed by adjusting the analytical model to represent the air gaps between laminations as presented in Section 4.1.

The geometric equations governing the relationship between the RT's outer diameter and length are proposed by Ruviaro in [14]. The dimensions of the RT are shown in Figure 5.4. The material discontinuity is taken into account by working relative to the inner core diameters where the laminations are completely flush and there are no gaps. These diameters are indicated in Figure 5.4 as D_{si} and D_{pi} for secondary and sides, respectively. In this way, the calculated

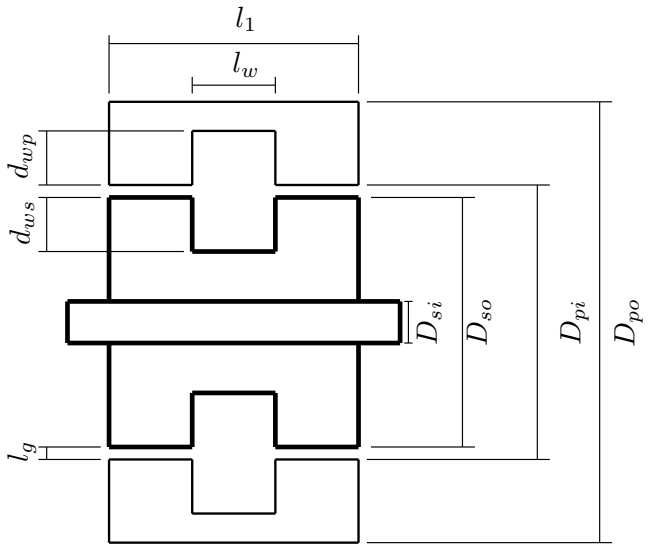

Figure 5.4: RT geometry.

area is larger than the results from the standard geometric relationships.

Another point of interest is the relationship between the inner shaft diameter and the RT's outer diameter and length. The relationship is presented in [26], where it is observed that as the shaft diameter is increased, the outer diameter, D_{po}, remains fairly constant while the outer length of the transformer, l_1, is effectively decreased. This relationship is illustrated in Figure 5.5. The relationship highlights the advantage of using a large shaft diameter to decrease the overall length and effectively minimise the size of the RT. The optimal point is chosen where the outer diameter is a minimum, indicated by point X in Figure 5.5.

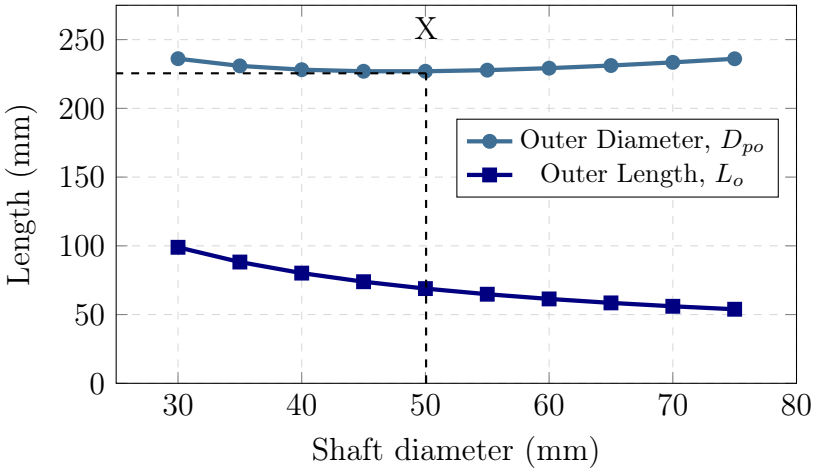

Figure 5.5: Change in 1.2 kVA single phase RT's outer diameter D_{po}, and length, l_1, with changing inner shaft diameter [26].

Keeping the above considerations in mind, the dimensions of the RT indicated in Figure 5.4 can be calculated. The window area needed for the windings is calculated based on the calculated number of turns, the current density and a suitable fill factor. The secondary core's outer diameter, D_{so}, is a function of the inner diameter, D_{si}, and the minimum core cross sectional area, A_c, as follows

$$D_{so} = \frac{2A_c}{\pi D_{si}} + (D_{si} + 2d_{ws}). \tag{5.2.6}$$

Similarly, the primary core's outer diameter is

$$D_{po} = \frac{2A_c}{\pi[D_{po} + 2l_g]} + (D_{so} + 2l_g + 2d_{wp}). \tag{5.2.7}$$

At this point the air gap length l_g is taken as the initial estimated value, until FEM analysis is carried out. The outer widths of the RT, both primary and secondary, are equal and calculated as

$$l_1 = \frac{2A_c}{\pi D_{si}} + (l_w), \tag{5.2.8}$$

once again a function of the secondary core's inner diameter and cross sectional area. l_w is the length of the window, which can be calculated from the window

area, A_w, with equation (5.2.1). A ratio of winding depth to winding length is chosen, based on the effect of the leakage inductance, as mentioned previously- a window that is longer than it is deep assists in decreasing leakage inductance.

Once the core dimensions have been calculated the model can be accurately built and used for the FEM analysis.

5.2.4 Parameter determination and FEM Analysis (Step 5 & 6)

The magnetising and leakage inductances are important considerations in the RT design. The equivalent circuit of the RT is initially developed using the method presented in Chapter 4. The parameters are used to build a model that can be analysed in FEM. The FEM analysis is then used to verify the values obtained from the analytical design. The model used in FEM analysis needs to be 3D to accurately model the inductances. Magnetising inductance is a function of the air gap length, as shown in Figure 3.7. The air gap length is chosen based on the magnetising inductances for that air gap length, and the practicality of constructing the RT.

Once the air gap is fixed the model is complete and can be used to verify the operation of the RT. The first operation condition tested is the RT connected in open circuit. This results in the highest flux density in the core and serves as an indication of the operating voltage at which the transformer's core will saturate. This is fundamental to the design as the core area is being minimised. If the FEM analysis indicates that the transformer is outside of the linear operating region at rated voltage, it is necessary to reduce the desired flux density. By doing so, the design procedure will yield a larger core. Once an acceptable size core is reached, the remaining operating conditions are analysed, with a focus on obtaining the core and copper losses of the RT. The core and copper losses can be reduced by lowering the magnetic and electrical loadings respectively if the efficiency is not within an acceptable range.

The detailed summary of the entire design procedure is outlined in Figure 5.6.

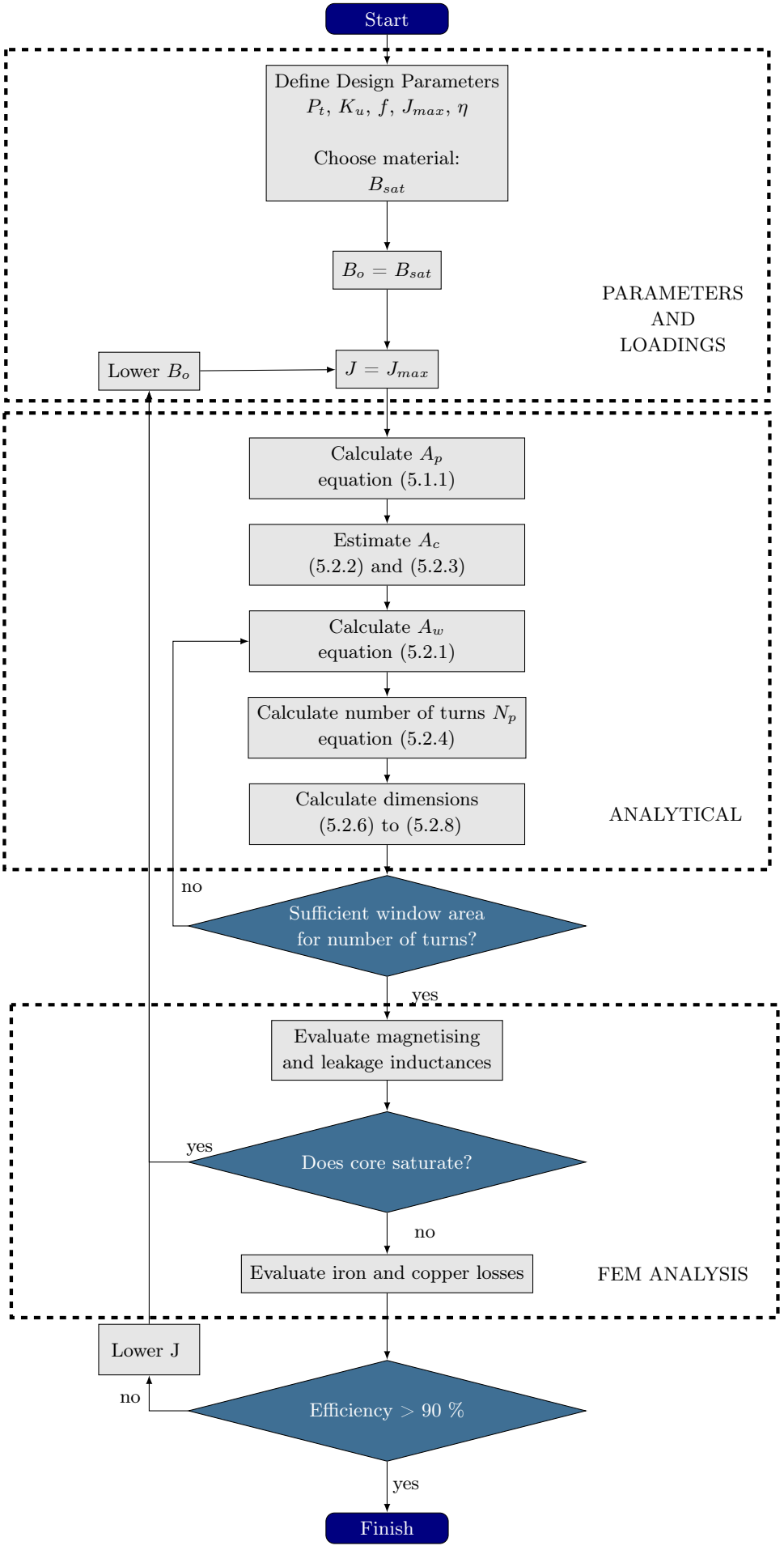

Figure 5.6: Flow chart illustrating the optimal design procedure

5.3 Scalability Study

This section presents a short study conducted to investigate the RT's size at medium and large power levels. At higher power levels, the slip rings also increase in size and require additional cooling mechanisms. It is therefore necessary to evaluate at which power level the RT becomes an advantage in terms of size.

The design procedure is used to design a single phase RT for a 3 kW, 400 kW and 1 MW induction generator. The useful relationship between shaft diameter and length has been demonstrated in the previous section. This relationship holds for all of these power levels as shown in Figure 5.7. The length and diameter of the RT assembly is then compared to the dimensions of commercially available induction generators.

The dimensions of the RT assembly accounts for 3 single phase units. The dimensions given of the induction generators include the machine housing. For an more fair comparison the RT dimensions are adjusted using a factor to account for the external housing. A factor of 15 % is chosen and is based on experience during the building of the prototype in [25].
The values of the main dimensions illustrated in Figure 5.8 are presented in Table 5.1. The results of the 1 MW setup reveal that the transformer is smaller than the IG both in terms of outer diameter and overall length. This indicates

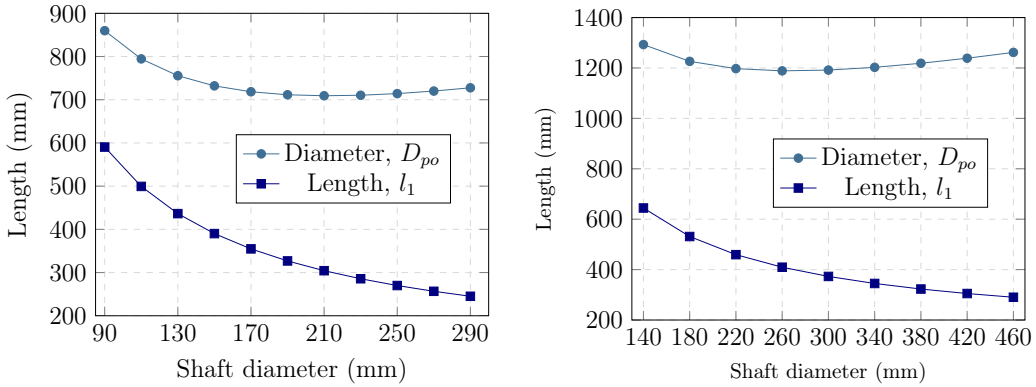

Figure 5.7: Change in (a) 400 kVA and (b) 1 MVA single phase transformer's outer diameter D_{op}, and length l_1, with changing inner shaft diameter [26].

the RT's favourable size at high power levels. A more accurate and revealing study would be to compare the RT dimensions against the size of the slip ring and brush assemblies that are used at the various power levels. At the higher power ratings, the RT size might well have an advantage as the slip rings require large cooling systems. More investigation is needed into RT cooling mechanisms at high power levels. It proved difficult to get the dimensions for the slip ring and brush assemblies alone, and so these results can not be compared.

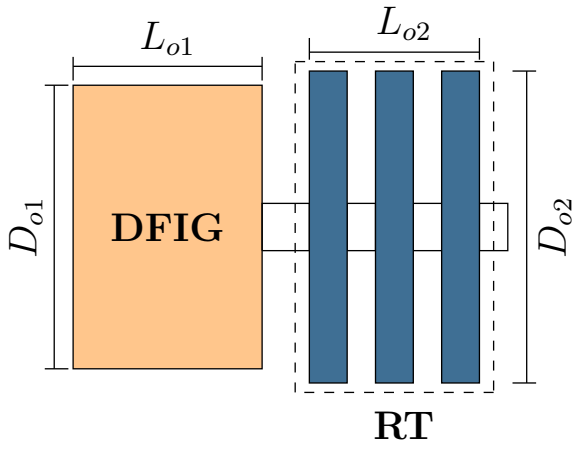

Figure 5.8: Outer diameters and lengths for both the DFIG and the rotary transformer, RT.

Table 5.1: Rotary transformer dimensions at various power levels [26].

	Outer diameter, D_o	Overall length, L_o	Unit
3 kW			
IG	244	431	mm
Rotary transformer	212.26	206.67 (68.89 × 3)	mm
400 kW			
IG	863	1677	mm
Rotary transformer	859.77	1171 (590.5 × 3)	mm
1 MW			
IG	1590	2505	mm
Rotary Transformer	1292.83	1932 (644 × 3)	mm

5.4 1.2 kVA Prototype RT

The proposed design procedure is applied to develop an RT for application with a 3 kW induction machine. The outcome of the design and testing will serve as verification of the developed design methodology.

5.4.1 RT Ratings and Loadings

The rating of the RT is based on induction machine's ratings. A single phase RT is required to handle the per phase power of the induction machine. Using the full load current and phase voltage of a standard 3 kW WEG induction motor, the power rating of the single phase RT is determined as 1.2 kVA. It is only necessary to design a single phase RT, as each unit of the three units is identical and can simply be duplicated. The operating frequency of the RT is 50 Hz.

The electrical and magnetic loadings are initially set to the maximum values as described in Section 3.1. The maximum current density, J_{max} is set at 5 A/mm^2. The window utilisation constant, K_u or fill factor is set at a conservative 0.4. The magnetic loading is set according to the saturation flux density of the magnetic steel used. The core of the RT is constructed using laminations of M400-50A magnetic steel with a magnetisation curve as shown in Figure 5.9.

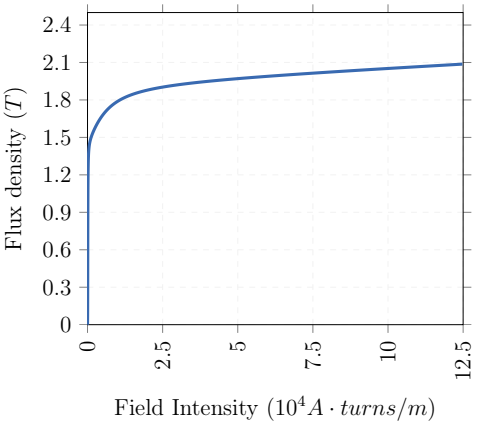

Figure 5.9: Magnetisation curve for M400-50A steel [40].

5.4.2 Core Area and Number of Turns

The required area product for the chosen ratings and loadings is determined using equation (5.1.1). The window area, A_w, and core cross sectional area, A_c, are calculated using the analytical equations (5.2.1) to (5.2.5). To evaluate the required window area for the number of turns, the current density and fill factor is needed. The results of this analytical design section are given in Table 5.2.

The RT designed in [25] has a power rating of 1 kVA. The core cross sectional area, A_c, is 114 cm^2. The new design methodology yields an cross sectional area of almost three times less, for a higher power rating.

Table 5.2: Designed Values

Symbol	Parameter	Value	Unit
A_p	area product	409.86	cm^4
A_c	core area	38.88	cm^2
A_w	window area	10.54	cm^2
V_p	primary rms voltage	230	V
N_p	primary turns	190	-

5.4.3 Core Dimensions

Using equations (5.2.6) to (5.2.8) the dimensions are calculated. An optimal shaft diameter is chosen as 50 mm from the curves presented in Figure 5.5. The air gap length is initially set to a conservative 0.5 mm. The full set of dimensions as shown in Figure 5.10 for the single phase RT is given in Table 5.3.

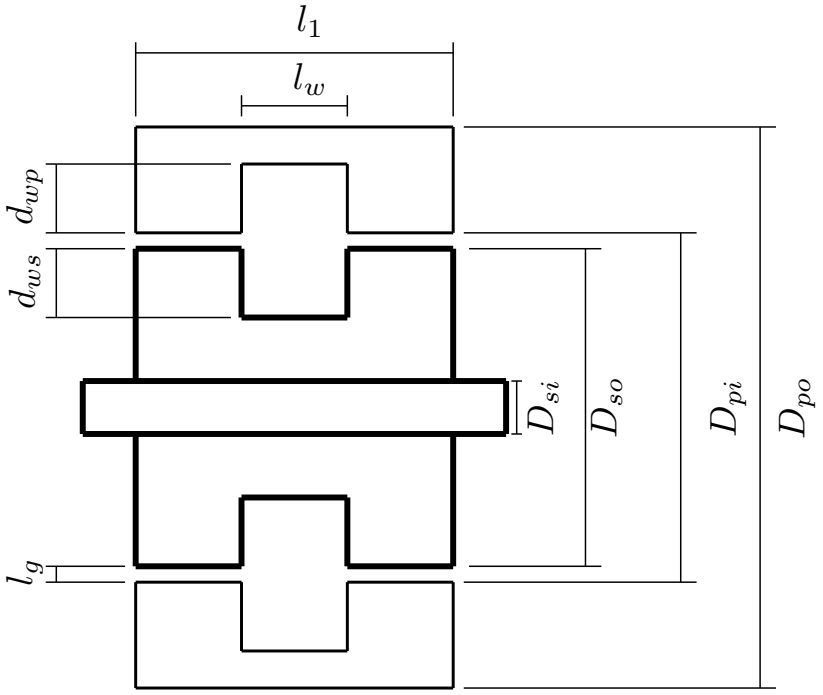

Figure 5.10: Rotary transformer geometry.

Table 5.3: Dimensions of 1.2 kVA axial RT

Secondary Side			
D_{si}	50 mm	l_w	13.27 mm
D_{so}	126.04 mm	l_g	0.5 mm
d_{ws}	39.76 mm	l_1	89.27 mm
Primary Side			
D_{pi}	127.04 mm	D_{po}	169.66 mm
d_{wp}	13.27 mm		

5.4.4 Equivalent Circuit Model

The values from the initial analytical calculations are summarised in Table 5.2. These values, along with the dimensions given in Table 5.3, are used to build a model that is implemented in the FEM package JMAG.

The FEM analysis of the magnetising and leakage inductances is conducted. The primary magnetising inductance as a function of air gap length is investigated to identify an optimal maximum magnetising inductance. The magnetising inductance plotted against the air gap length is shown in Figure 5.11. From these results an optimal air gap length of 0.4 mm is chosen, which offers a good trade-off between higher magnetising inductance and an air gap length that is practically achievable. The dimensions presented in Table 5.3 are updated to reflect the decrease in air gap.

The leakage inductances as a function of air gap length are evaluated through FEM analysis and shown in Figures 5.12(a) and 5.12(b). There is a slight variation as a function of air gap length. From the graphs it is clear that the air gap of 0.4 mm yields a suitably low leakage inductance.

The full set of inductances for the design, with an air gap of 0.4 mm is shown in Table 5.4.

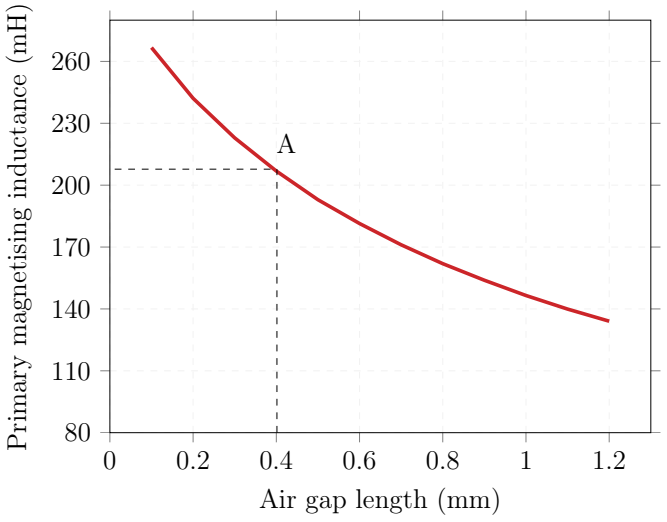

Figure 5.11: Primary magnetising inductance as a function of the air gap length

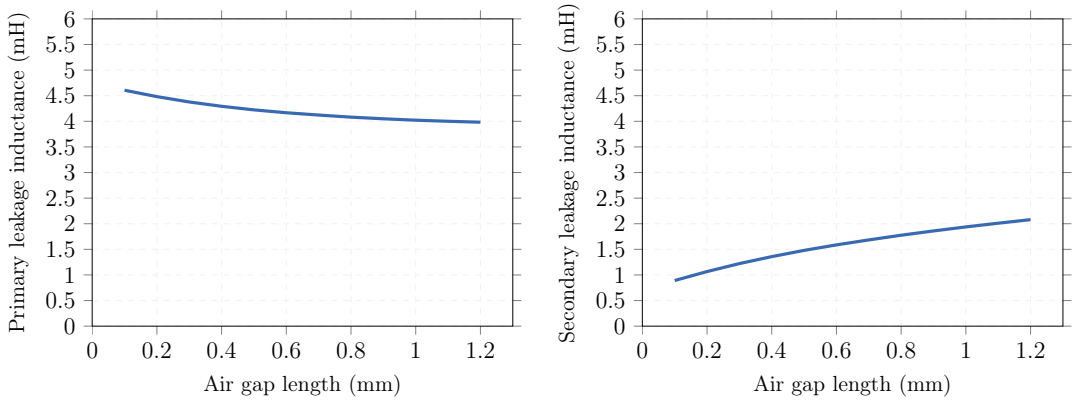

(a) (b)

Figure 5.12: Primary (a) and secondary (b) leakage inductances as a function of air gap length.

Table 5.4: Inductances of design

	Analytical	Analytical with error correction	FEM	Unit
L_{mp}	550.72	276.69	206.85	mH
L_{lkp}	5.57	5.57	4.29	mH

The magnetising inductance is susceptible to the effects of the air gaps between the laminations. If the air gaps between the laminations are not taken into account by using the stacking factor of the core as explained in Section 4.1.2.1, the value for magnetising inductance is about 3 times the simulated value. The analytical model that accounts for the spacing (analytical with error correction), corresponds better to the FEM result, but there is still room for improvement. A summary of the stacking factors used in the design are shown in Table 5.5. The factors are estimated using the method presented in Section 4.1.2.1. Error correction is not needed for the analytical values of primary leakage inductances, as they are not as affected by the air gaps between the core laminations. The leakage inductance is only affected by the main air gap of the core, which has already been accounted for as explained in Chapter 4. The analytical value of the primary leakage inductance, L_{lkp}, and the FEM

correspond reasonably well.

Table 5.5: Stacking factor percentage of core sections

Section	Stacking Factor
Primary axial	40%
Primary radial	50%
Secondary axial	75%
Secondary axial	60%

Once the air gap length is fixed based on the inductances, the model is used to simulate the operation of the transformer. The most important test is determining whether the reduced size of the designed core is large enough to handle the power rating without the core saturating. FEM simulation can be used to check the flux density at the designed operating point, and the current and voltage waveforms can be inspected for saturation effects. However the most comprehensive method of determining the transformer's performance is the no load characteristic curve.

Initially, a section analysis is done to evaluate the magnitude of the magnetic flux density in the core. The highest flux density occurs under no load operation. The simulation is run at rated voltage with the secondary winding of the transformer open. The circuit condition used for the simulation is shown in Figure 5.13.

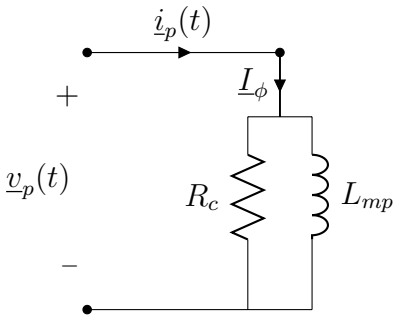

Figure 5.13: Equivalent circuit of RT no-load operation.

The magnetisation curve shown in Figure 5.9, for the M400-50A magnetic steel used, shows that the saturation flux density is 1.8 T. The maximum value from the simulation is found to be 1.33 T, which is well below the maximum threshold. The contour plot of the flux density under no-load condition, at rated voltage of 230 V, is given in Figure 5.14. The maximum flux density occurs at the inner corners of the secondary core. This can be explained by the fact that although the secondary side has a wider yoke, the active material percentage is lower than on the primary side, due to the lamination separation.

To obtain the no load characteristic curve, the applied voltage is increased incrementally up to 110 % of the rated value. This primary voltage is plotted as a function of the developed primary current. The resulting curve for the design is shown in Figure 5.15. The initial linear region indicates the ideal region of operation. The rated voltage should sit below the knee of the graph. As the

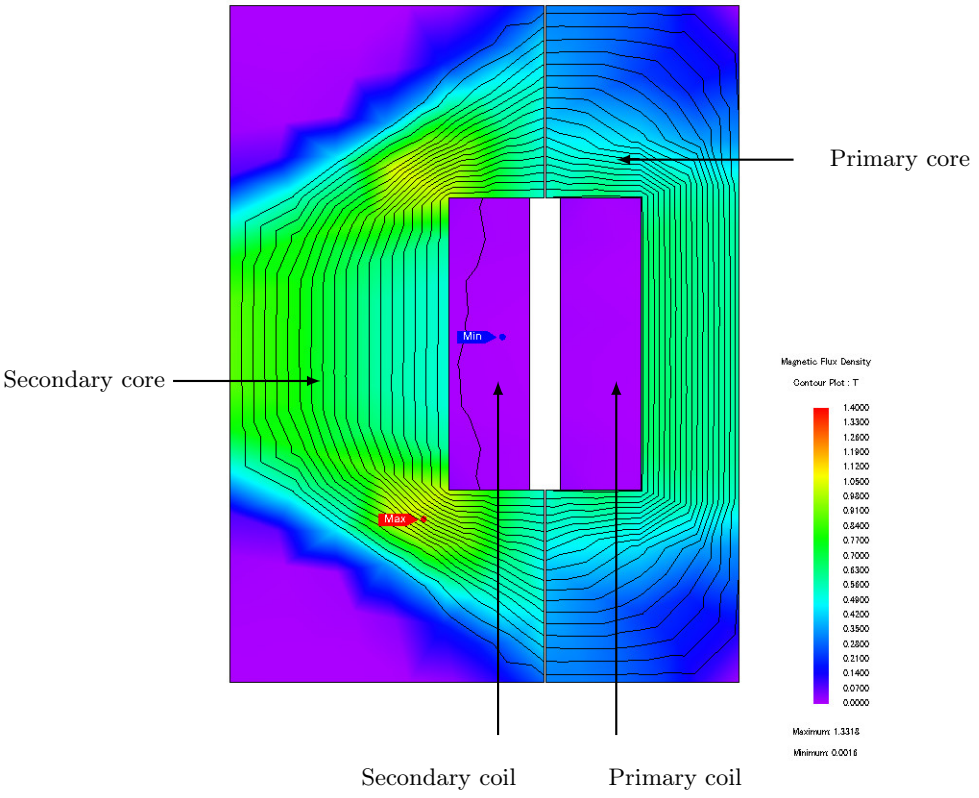

Figure 5.14: Open circuit flux density plot from JMAG simulation

voltage is increased beyond the linear region, the current will start to increase much quicker, indicating saturation of the transformer core. The rated voltage for the design, 230 V, is indicated on the graph in Figure 5.15 and it is clear that it lies well within the linear region.

The voltage and current waveforms for no load operation at the rated voltage are shown in Figure 5.16. There is no distortion of the sinusoidal curve, confirming the RT is operating in the linear region and core saturation is avoided.

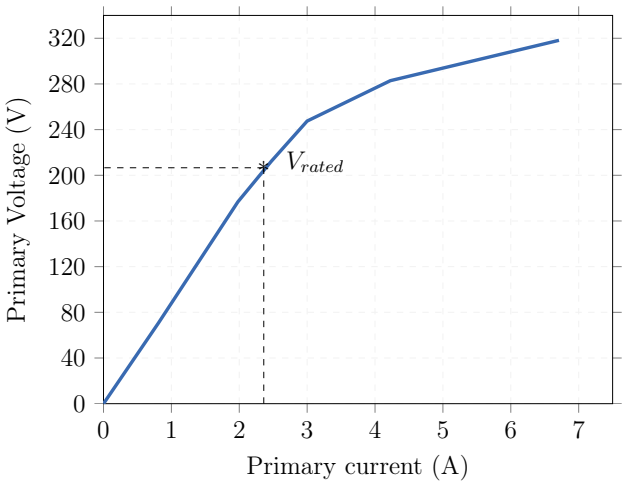

Figure 5.15: Simulated open circuit characteristic curve of the transformer.

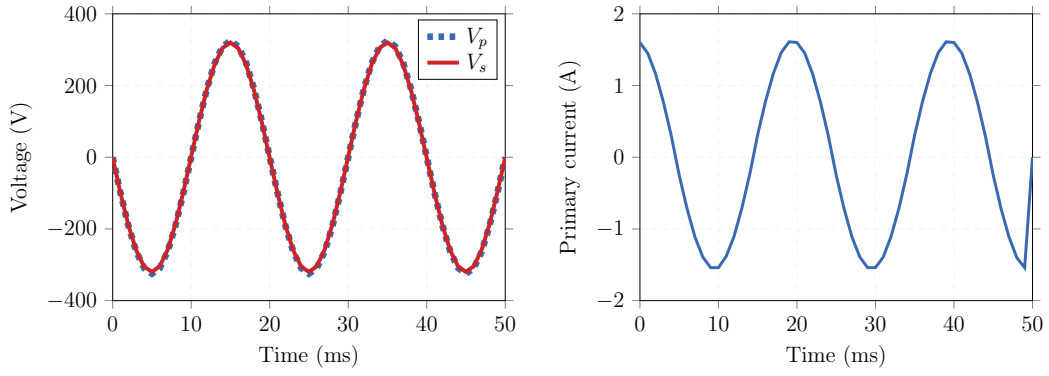

Figure 5.16: Simulated waveforms at the rated no load operating point. (a) Primary and secondary voltage (b) Primary current.

The RT's voltage and current waveforms under full load conditions are also simulated and presented in Figure 5.17(b) and Figure 5.17(b) respectively.

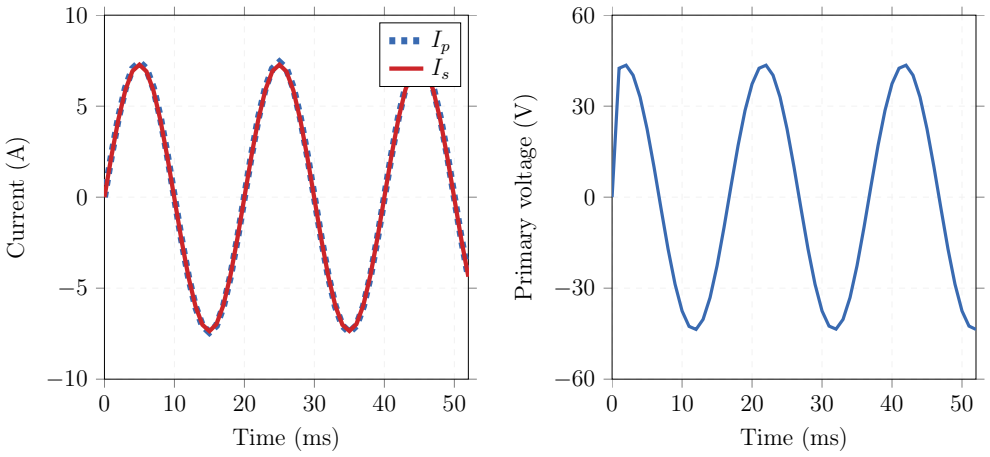

(a) (b)

Figure 5.17: Simulated waveforms at the full load operation (a) Primary and secondary full load current (b) Primary voltage.

5.4.5 Summary

A methodology to design a minimum size RT, for a given power rating, is presented. The design process makes use of the model developed in Chapter 4. The design results in an RT that is considerably smaller than a previously built prototype, yet also offers better performance. This is largely due to the developed analytical model being able to account for the unique characteristics of the RT.

An investigation into the size of the RT at increasing power levels is conducted. The RT design is scalable and the size is suitably smaller than the induction machine at the higher power levels. The developed methodology is then used to design a 1.2 kVA RT that will be built and tested to verify the outcome of the design procedure.

Chapter 6

Mechanical Design and Assembly

The RT has a more complicated mechanical design than that of a standard transformer. The following section details the mechanical design process and manufacturing of the RT.

The primary (outer) side of the RT, shown in Figure 6.1(a), remains stationary. The secondary (inner) side, shown in Figure 6.1(b), is mounted within the primary, on a shaft that is free to rotate. The full assembly is presented in Figure 6.2.

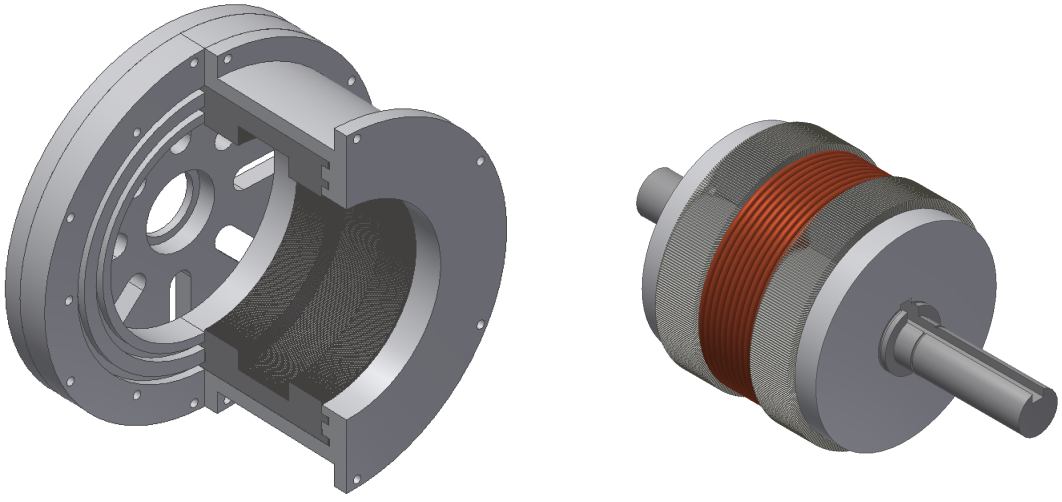

(a) (b)

Figure 6.1: (a) The primary side assembly, and (b) the secondary side RT assembly

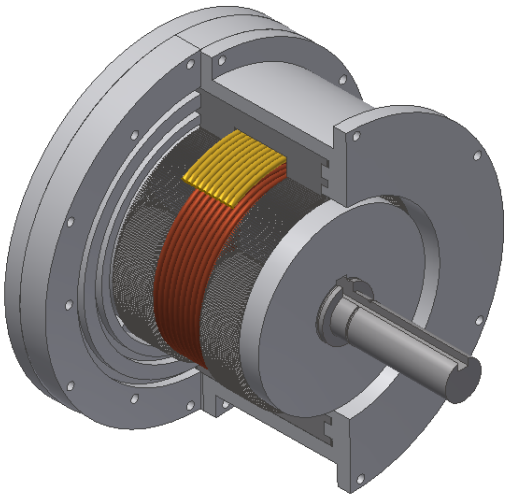

Figure 6.2: Cross sectional view of the complete RT assembly. The secondary side of the RT from Figure 6.1(b) is mounted inside the primary side shown in Figure 6.1(a).

The sizing of the shaft and the core is determined by the electrical design in Section 5.4.3. The mechanical design of the structural housing is carried out and the RT is constructed. The technical drawings for each component are available in Section 8.2. The following section details the construction process.

6.1 Secondary (Inner) Portion of RT

The RT's core needs to be constructed using steel laminations placed radially around the shaft and be held securely in place. The previous prototype built in [25] proved complicated to assemble and the achieved stacking factor of the laminations, especially on the inner secondary core section, was very low as shown in Figure 6.3.

From the previous work it is evident that the large air gaps between the laminations cause problems during the RT's operation. In order to overcome this limitation, smaller laminations are placed between the existing laminations. The sizing and placement of these laminations are indicated in Figures 6.4(c) and 6.4(d), respectively. The laminations contain two square ledges which are used to secure them to the end plates.

Figure 6.3: Prototype RT developed in [25]

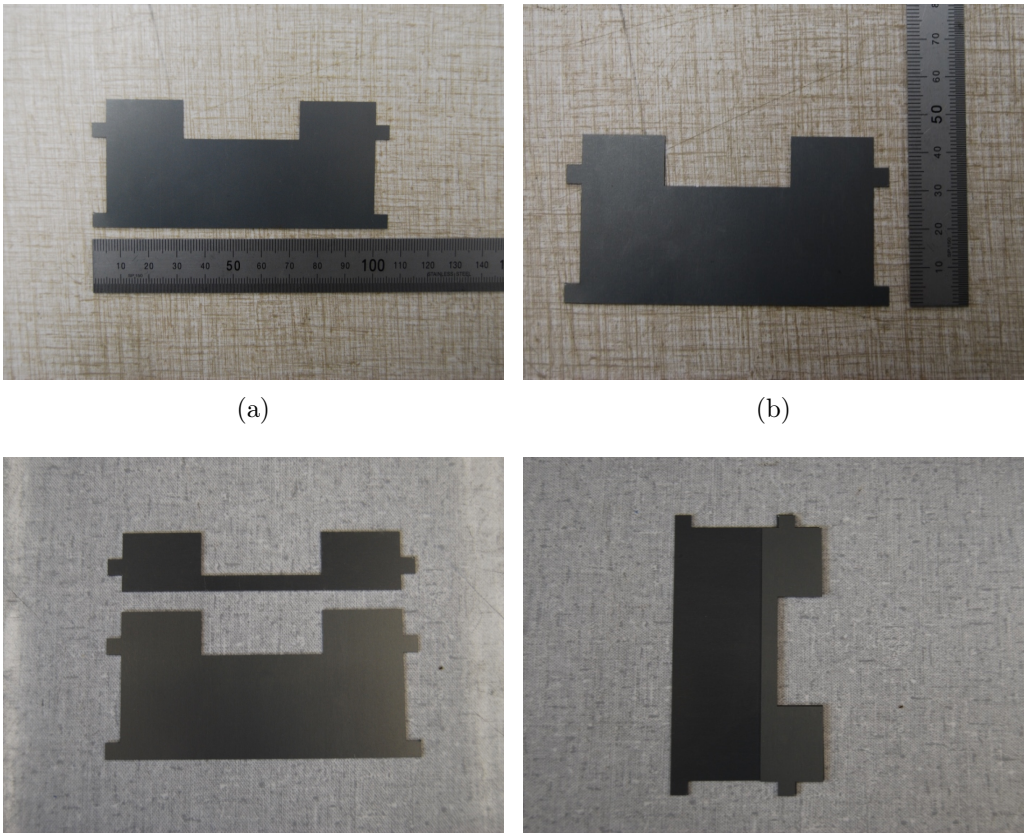

(a) (b)

(c) (d)

Figure 6.4: Secondary side lamination sizing: (a) Length, (b) Height. (c) and (d) show the size of the spacing lamination with respect to full size lamination.

The shaft and secondary support structure is shown in Figure 6.5. The shaft has a groove that allows the winding of the secondary coil to be taken out of the RT and along the shaft so that it can couple to the induction machine. This is

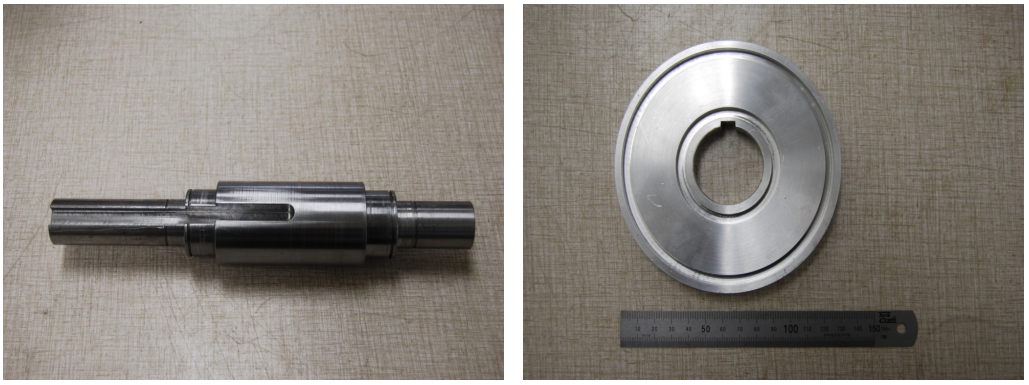

(a) (b)

(c)

Figure 6.5: Shaft and secondary side support structure: (a) Transformer's shaft, (b) secondary side end plate. (c) End plate fixed to the shaft, ready for lamination placement

shown in Figure 6.5(a). To assemble the secondary side, the first end plate is secured to the shaft as indicated in Figure 6.5(c). This is mounted upright and then all the laminations are packed in. Once all the laminations are placed the second end cap is secured. The process of stacking the laminations is shown in Figure 6.6. The effect of the additional laminations is evident if Figure 6.6(a) and Figure 6.6(d) are compared.

Once the laminations are all placed and the end cap is secured, the winding is placed. To wind the RT is simple, but care must be taken to ensure the end windings can be fed out through the bore on the shaft. Figure 6.7(c) shows

the suitable fill factor achieved, including the tape and varnish to secure the windings. The location of the end windings in the shaft groove is show in Figure 6.7(d).

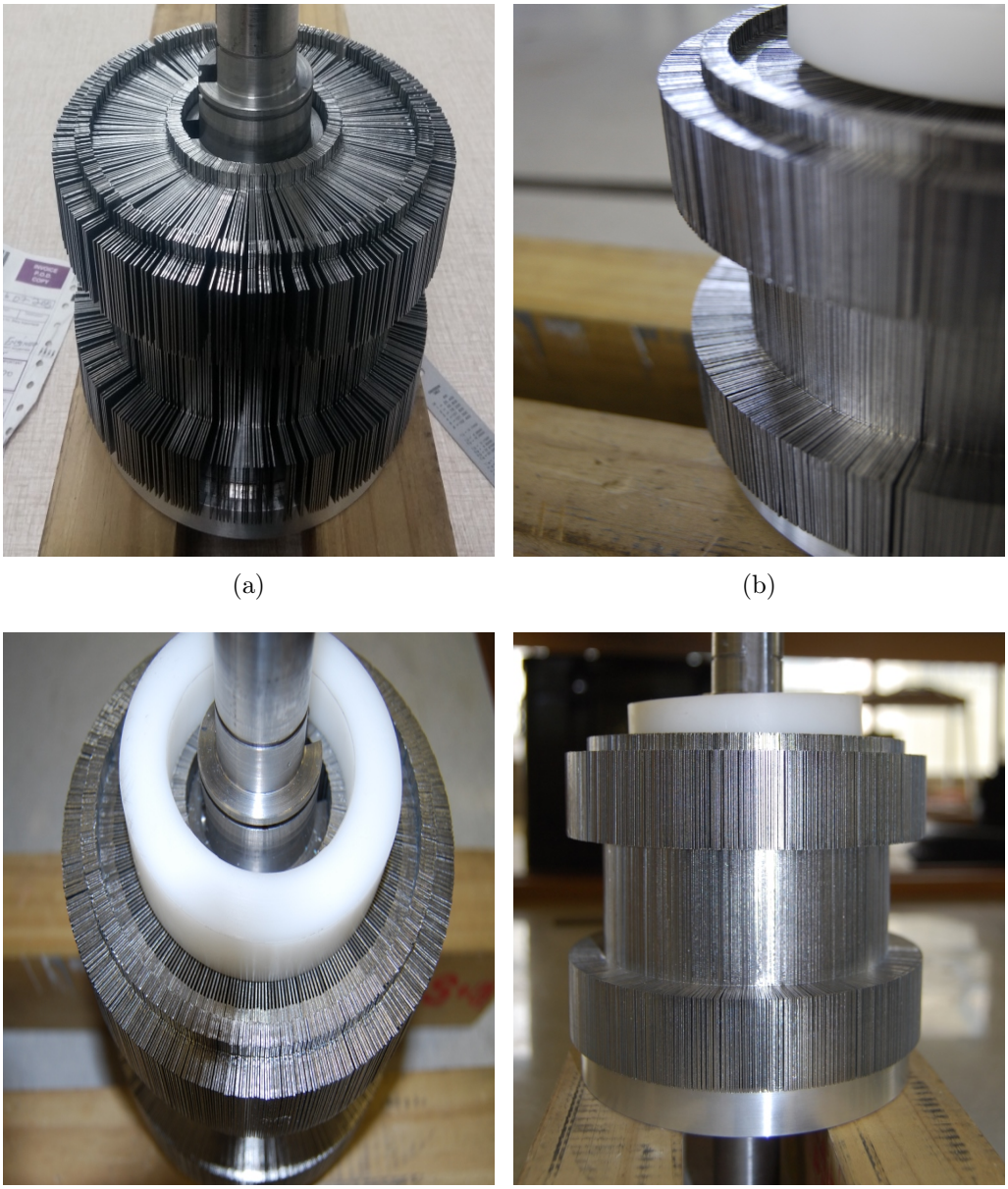

(a) (b)

(c) (d)

Figure 6.6: Secondary core assembly: (a) Before additional laminations are placed (b) side view, (c) top view, (d) full view

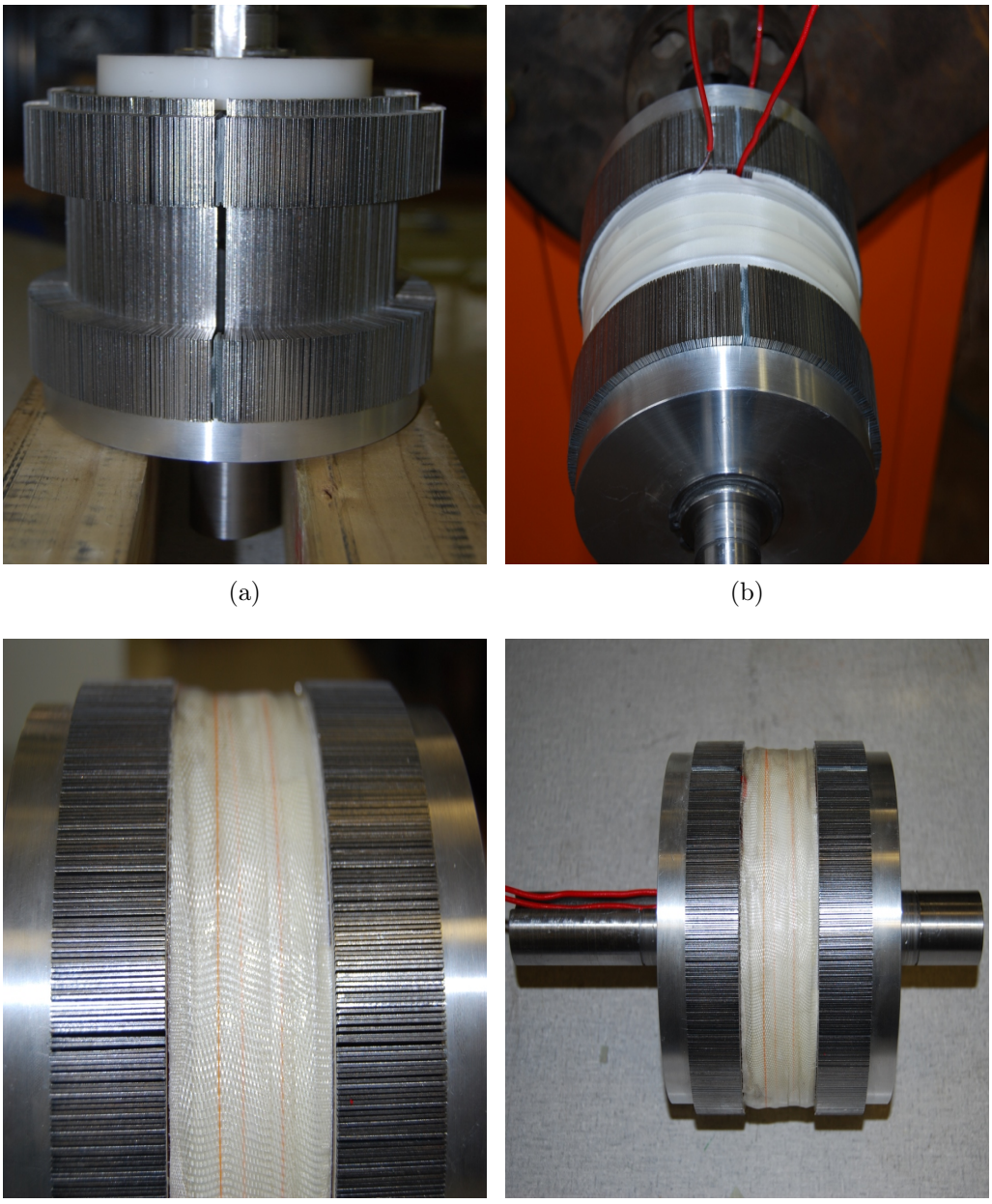

(a) (b)

(c) (d)

Figure 6.7: Secondary side winding: (a) Gap for end of secondary coil, (b) Completion of winding with insulating tape. (c) Close up of winding, (d) Final secondary side assembly.

6.2 Primary (Outer) Portion of RT

The primary side of the RT is more complex to construct since it requires the winding to be wound first and the core constructed around it. The technique used is to construct the primary core of the RT in two halves as indicated in Figure 6.8(b). The coil is wound using a former of the correct size. It is then wrapped in cloth and resin to keep it rigid. Once the coil is set as shown in Figure 6.8(a), the two sides of the core are brought over it and the assembly is secured using the end plates. The assembly procedure is demonstrated in Figure 6.8. The stacking factor of the laminations on the primary side is better than that of the secondary side. This is clearly indicated in Figure 6.8(e). The laminations for the primary core are shorter than the secondary laminations due to the geometric relationships discussed in Section 5.2.3. This results in a smaller deviation between the laminations at the outer diameter. Air gaps do still exist between the laminations but it is not feasible to add extra "inter-laminar" laminations in the primary core as they would be extremely narrow and difficult to place. The final primary side assembly is shown in Figure 6.8(f). The coil can be seen inside the window area of the coil. The primary coil ends that are removed from the housing can also be seen.

During assembly it was not possible to fit the desired number of turns on the primary winding. The number of turns and window area is the same as the on the secondary side. However, the complication of having to wind on a former and add extra resin and cloth to keep the winding rigid all results in the fill factor being lower than the designed value. The number of turns in the primary is 155, while the design value was 190.

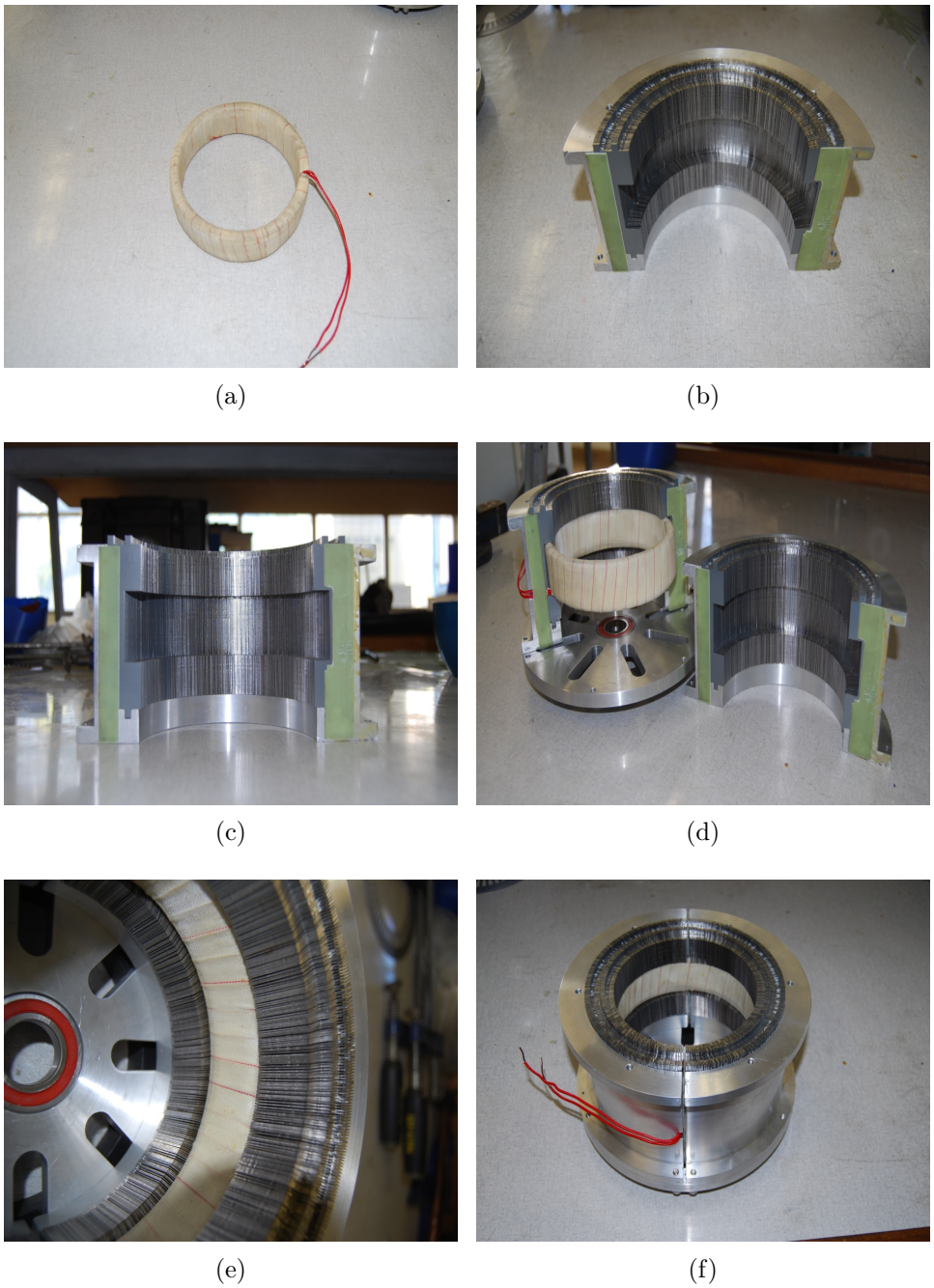

(a) (b)

(c) (d)

(e) (f)

Figure 6.8: Assembly of the primary portion of the RT: (a) primary coil, wrapped and coated in resin. (b) top view of core half and, (c) front view of core half. (d) Core half placed over the formed coil. (e) close up of the coil placed in the core. (f) completed assembly.

6.3 Full Assembly

The RT assembly is completed by placing the secondary side assembly into the primary side assembly. The end plate is then used to secure the primary core laminations and the bearing end-plate is fitted to align the shaft. The designed air gap of 0.4 mm is achieved, and the secondary side can freely rotate. The RT before it is closed with the bearing end plate is shown in Figure 6.9.

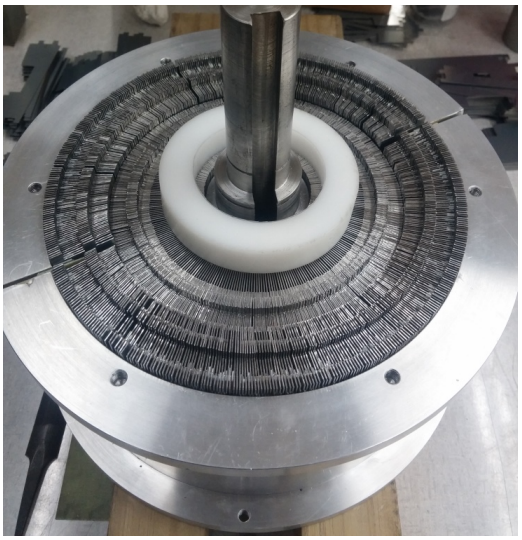

Figure 6.9: Secondary, rotating side, of RT placed inside the primary, stationary side, before the end plate is fitted.

6.4 Summary

This chapter presents the mechanical design of the RT. The outer housing is designed to ensure the laminated core is securely fastened. The tolerances on the design need to be correct in order to achieve an air gap of 0.4 mm, with a radially laminated core. Smaller laminations that fit in the air gaps between the main laminations are placed on the secondary side core, to improve the percentage of active material. The designed primary winding fill factor of 0.6 is not sufficient to fit the required number of turns. This is due to the extra insulation and support the primary winding requires. The primary turn number is adjusted to 155 turns.

Chapter 7

RT Measurements

The RT designed in Chapter 5 and Chapter 6 is tested in order to measure the designed parameters, analyse the operating conditions and determine the losses. The analytical and simulated results need to be updated, as the primary turn number changed from 190 to 155, as mentioned in Chapter 6. The effect of this change in turn number needs to be evaluated during testing.

The chosen tests are performed initially while the RT is stationary. The RT is then rotated, in order to compare with the stationary test results and determine the effect of rotation. The following tests are conducted:

Resistance and Inductance Measurements

The RT model developed in Section 4.1 and used in FEM analysis needs to be experimentally verified. This can be done by determining each of the parameters in the equivalent circuit shown in Figure 7.1.

No Load Test

The RT is tested under no-load conditions by keeping the RT's secondary terminals open. to determine the shunt parameters of the equivalent circuit. The maximum core loss can also be determined at this operating condition. The no load circuit characteristic curve provides a good indication of the applied voltage at which the RT core will begin to saturate.

Short Circuit Test

The short circuit test consists of shorting the secondary terminals of the RT, while applying enough voltage to deliver full load current. The test reveals the maximum conduction losses in the windings.

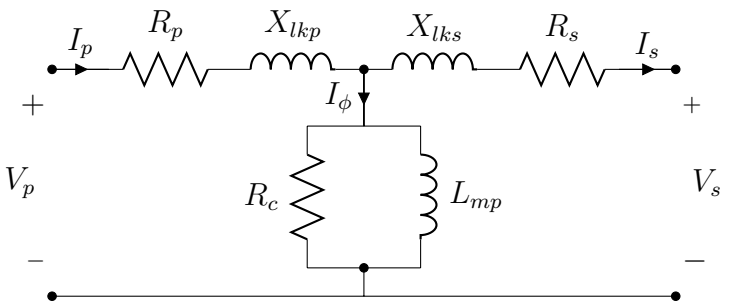

Figure 7.1: RT equivalent circuit

7.1 Resistances and Inductances

The primary and secondary winding resistances, R_p and R_s are obtained by doing a simple DC resistance test. In order to determine the magnetising, L_{mp}, and leakage inductances, L_{lkp} and L_{lks}, the following inductances need to be measured using the LCR meter:

1. The primary winding inductance with the secondary winding open, $L_{p(oc)}$
2. The secondary winding inductance with the primary winding open, $L_{s(oc)}$
3. The primary winding inductance with the secondary winding shorted, $L_{p(sc)}$

Then mutual inductance, M, is given by [41],

$$M = \sqrt{(L_{p(oc)} - L_{p(sc)})L_{s(oc)}}, \tag{7.1.1}$$

where $L_{p(oc)}$ is the primary winding inductance with the secondary winding open, $L_{s(oc)}$ is the inductance of the secondary winding with the primary winding open and $L_{p(sc)}$ is the inductance measured at the primary winding with the secondary winding short circuited.

The magnetising inductance is a function of the primary and secondary turns ratio, and the mutual inductance. The magnetising inductance as seen from the primary winding, L_{mp}, is

$$L_{mp} = \frac{N_s}{N_p} M, \tag{7.1.2}$$

and from the secondary winding,

$$L_{ms} = \frac{N_p}{N_s} M. \tag{7.1.3}$$

The primary and secondary leakage inductances,L_{lkp} and L_{lks}, are given by,

$$L_{lkp} = L_{p(oc)} - L_{mp} \tag{7.1.4}$$

and

$$L_{lks} = L_{s(oc)} - L_{ms}, \tag{7.1.5}$$

The DC winding resistances of both coils are shown in Table 7.1. The values compare well to the analytical values calculated in Section 2.1.

The measured inductances are shown in Table 7.2, and compared to the FEM and analytical values.

Table 7.1: Winding resistances at 20°C.

	Analytical	Measured	Unit
R_p	1.05	1.1	Ω
R_s	0.98	1.0	Ω

Table 7.2: Inductances of updated design, with 155:190 turn ratio

	Analytical	Analytical with error correction	FEM	Measured	Unit
L_{mp}	366.5	184.14	196.13	195.44	mH
L_{lkp}	-	4.79	3.28	3.8	mH
L_{lks}	-	0.46	0.58	1.74	mH

The magnetising inductances in Table 7.2 shows good correlation between measured and FEM values. The analytical results do not correlate well with the FEM or measured results, but shown a marked improvement over the values determined using the classical model. There is an increase in the measured values of leakage inductances, specifically for the leakage seen from the secondary side, L_{lks}. This discrepancy can be explained by the RT experiencing higher leakage flux due to the non ideal placement in the window area, especially concerning the extra layers of fabric tape to hold the coil rigid.

7.1.1 Effect of rotation

The inductances of the RT are measured while the RT is rotating. A Mercotac rotating contact is used to access the secondary winding of the RT while it rotates at a speed of 50 rpm. The test bench set up to run the test is shown in Figure 7.2. As mentioned in Section 3.7, the only parameters that are influenced by the RT rotating are the inductances. The leakage inductance, L_{lkp} increased by 11 % during rotation. The magnetising inductance increased by less than 1 %, indicating that a uniform air gap is maintained throughout rotation.

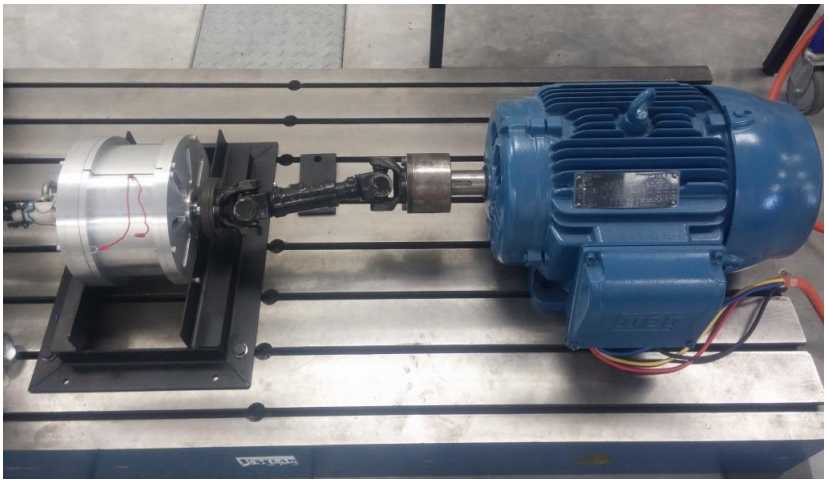

Figure 7.2: RT test bench.

7.2 No Load Test

The no load test consists of applying 0 - 110% of rated voltage to the RT's primary winding while the secondary winding is open. The corresponding primary current, secondary voltage and the power are measured during the test. The results of this test provide information to calculate the core loss and the shunt parameters of the RT. The equivalent circuit of the RT under no load operation is shown in Figure 7.3.

In a standard transformer the impedance of the exciting branch is high and so the voltage drop across the primary impedance is assumed to be negligible. However, this assumption can no longer be made in the case of the RT since the air gap leads to a low magnetising inductance. When analysing the current components and core loss under no load operation, this needs to be accounted for.

The power measured under no load, for a standard transformer, only represents core loss. For the RT the power loss under no load now contains a component of copper loss, such that the power drawn is given as,

$$P = I_c V_{p(oc)} + I_{p(oc)}^2 R_p. \tag{7.2.1}$$

where $V_{p(oc)}$ and $I_{p(oc)}$ are the measured primary voltage and current respectively. R_p is the primary winding resistance obtained from the DC resistance test. I_c is the component of the primary current that represents the core loss, and this can be calculated by solving for I_c in equation (7.2.1).

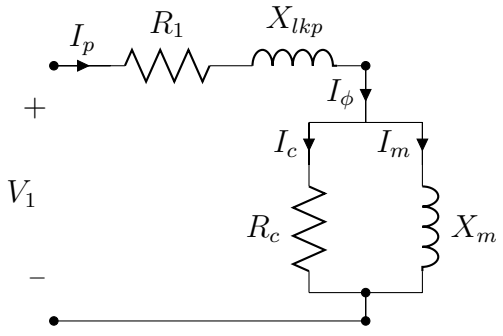

Figure 7.3: RT equivalent circuit for no load condition

The magnetising current I_m can then be calculated as,

$$I_m = \sqrt{I_{p(oc)}^2 - I_c^2}. \tag{7.2.2}$$

The magnetising reactance X_m can then be calculated as,

$$X_m = \frac{V_{p(oc)}}{I_m}, \tag{7.2.3}$$

and the value of the core loss resistance R_C is found from,

$$R_c = \frac{V_{p(oc)}}{I_c}. \tag{7.2.4}$$

An important indicator of the RT's performance is the no load characteristic curve. This graph is obtained by plotting the primary voltage vs. primary current. The desirable region of operation is such that this curve is linear. Once the graph starts to level out, a much larger current is required to sustain the same rated voltage, indicating saturation of the ferromagnetic core.

The no load characteristic curve of the transformer is plotted in order to evaluate whether the rated operating point falls within the linear region as indicated by the FEM analysis.

The number of turns in the primary winding were changed when constructing the RT. This is due to poor fill factor, where only 155 of the 190 design turns could be placed. The RT no longer has a 1:1 transformation ratio. If the primary number of turns is decreased, the rated voltage will also be lowered, while the rated current will increase. The new primary rated voltage is 187.5 V. The no load test is conducted first by magnetising the primary winding, and the curve is shown in Figure 7.4. Then a repeat of the test is done, now magnetising the secondary and leaving the primary winding open. This allows an evaluation of the RT's operation at the original rated voltage of 230 V. The no load curve for this condition is shown in Figure 7.5.

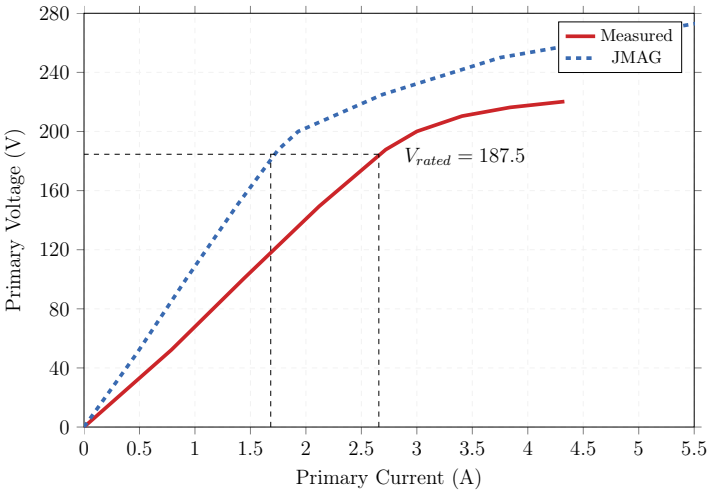

Figure 7.4: No load characteristic curve with the LV winding magnetised

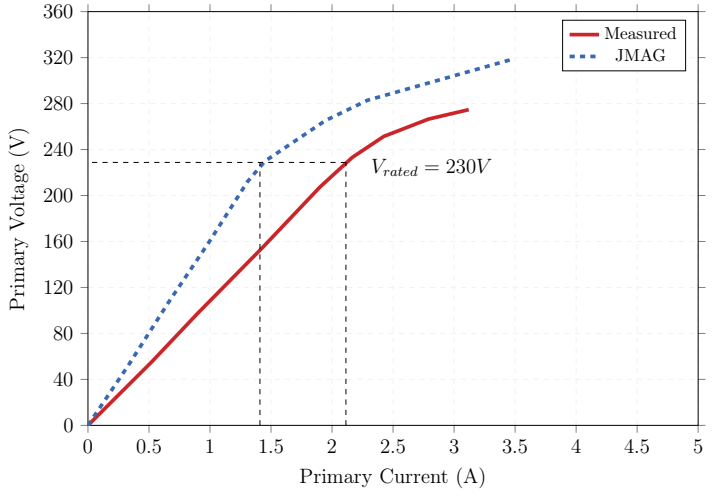

Figure 7.5: No load characteristic curve with the HV winding magnetised

Both graphs show that the operating point lies well within the linear operating region, indicating that the transformer's core size is sufficient for the power rating. Although both the simulated and measured waveforms provide the same result in this regard, there is a variation in the slope of the linear regions. The slope of the FEM results is much steeper, indicating less current is needed for the same voltage value. This variation can either be a caused by a difference in magnetising inductance or core loss. Under no load conditions the active components are as shown in Figure 7.3. This indicates that an increase in

current is directly related to an decrease in the magnetising inductance as well as an increase in the core loss of the actual RT. Since the FEM and measured values for the magnetising inductance in Table 7.2 correlate well, the change in slope can be directly attributed to the increase in core loss of the actual transformer. This increase in core loss can be attributed to the use of the smaller laminations to fill air gaps. Since the laminations are not the full size, heating and core loss can occur at the edges.

The waveforms presented in Figure 7.6 and Figure 7.7 show the no load voltage and current respectively. The waveforms are smooth, with no indication of saturation at the rated operating point. The no-load measurement summary is given in Table 7.3.

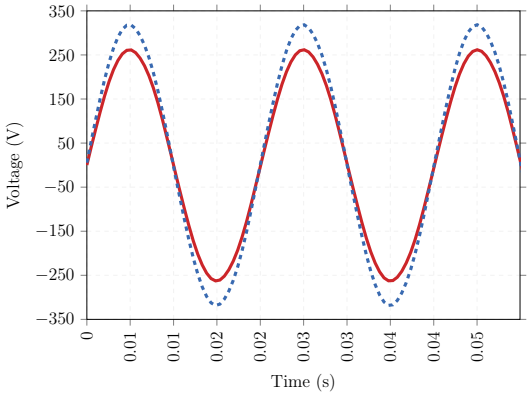

Figure 7.6: Primary and secondary voltage under no-load

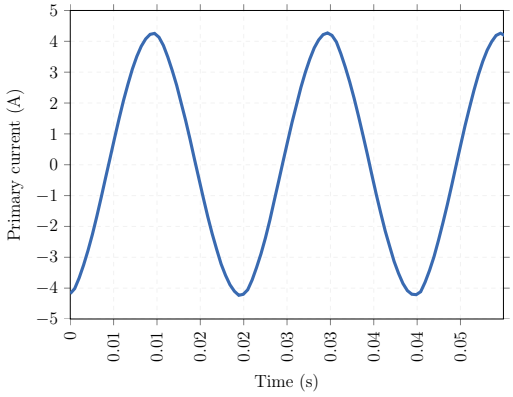

Figure 7.7: Primary current under no-load

Table 7.3: No load measurement summary

Parameter	Value	Unit
$V_{p(rated)}$	187.5	V
I_p	3.03	A
P	28	W
X_m	61.91	Ω
R_c	1963.93	Ω

7.2.1 Short Circuit Test

The short circuit test is used to determine the remaining equivalent circuit parameters. The secondary winding is shorted while primary voltage is applied until the primary current reaches the full rated value. This typically occurs at around 10-15% of the full load voltage. Under this condition the induced flux is low enough to be neglected and the power loss is purely the conductive losses in the windings, given by:

$$P_{sc} = I_{p(sc)}^2(R_p + R_s'). \tag{7.2.5}$$

In this case the cantilever equivalent circuit shown in Figure 7.8 can be used to determine the parameters. The equivalent resistance is given as

$$R_{eq} = R_p + R_s', \tag{7.2.6}$$

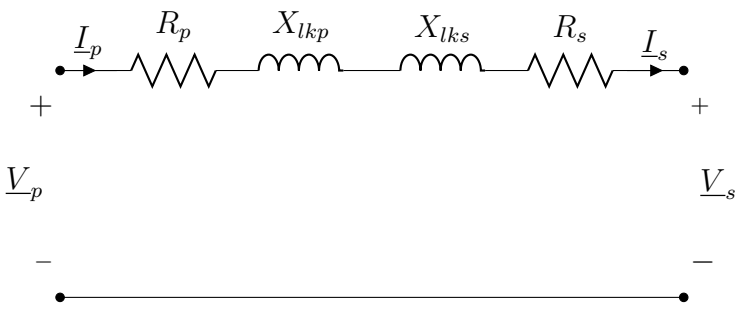

Figure 7.8: RT equivalent circuit for full load operation

The equivalent reactance is given by,

$$X_{eq} = X_{lp} + X'_{ls}. \tag{7.2.7}$$

The equivalent impedance, Z_{sc}, is needed to calculate the reactance. The simple calculation,

$$Z_{sc} = \frac{V_{p(sc)}}{I_{p(sc)}} \tag{7.2.8}$$

can be done. The winding resistances are already known, then the reactances can be determined from,

$$X_{lkp} + X_{lks} = \sqrt{Z_{sc}^2 - (R_p + R'_s)^2}. \tag{7.2.9}$$

The full load operation gives a measure of the maximum copper losses that exist in the transformer. The low voltage winding on the primary results in a higher current value that the original design. The wire diameter has already been set, so the increase in current translates directly to an increase in current density and winding loss. Table 7.4 gives the change in current and the subsequent increase in current density. The increase current density of 5.2 A/mm^2 is still within reasonable boundaries for operation, but will contribute to an increase in conduction losses.

The current and voltage waveforms under full load operation are given in Figures 7.9 and 7.10 respectively.

Table 7.5 provides a summary of the full load operation. The measured conduction loss is 6.3 % of the rated power, at 76 W.

Table 7.4: Change in current rating due to decrease in primary turn number

Design		**Actual**	
Rated Current	Current Density	Rated Current	Current Density
5.25 A	4.28 A/mm^2	6.43 A	5.20 A/mm^2

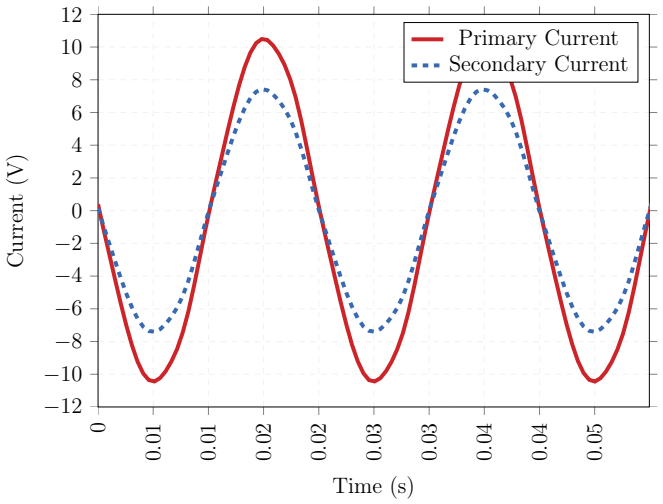

Figure 7.9: Primary and secondary current under full load

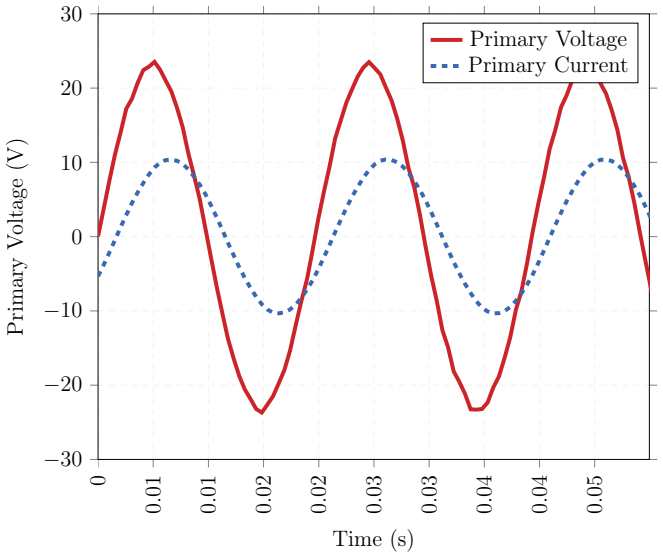

Figure 7.10: Primary waveforms under full load

Table 7.5: Summary of full load measurements

Parameter	Value	Unit
$I_{s(rated)}$	5.213	V
V_p	14.22	A
P_1	76	W
$X_{lkp} + X_{lks}$	1.94	Ω

7.3 Efficiency and voltage regulation

The power dissipated in the windings is measured for an increase in load current and the results are plotted in Figure 7.11. The gradient of the curve increases steeply as the load increases. This highlights the effect the change in turn number will have. The increase in core loss that this causes will have a negative impact on the efficiency of the RT.

The maximum copper and core loss values obtained through testing are used to calculate the efficiency of the transformer using,

$$\eta = \frac{P_{output}}{P_{input}} = \frac{P_{input} - P_{losses}}{P_{input}} \tag{7.3.1}$$

The efficiency is calculated as,

$$\eta = 91.38\%. \tag{7.3.2}$$

This efficiency of 91.38 % meets the minimum design threshold of 90 %. This is despite the increase in conduction loss. It is clear that a higher efficiency will be possible using the designed number of turns in the primary winding.

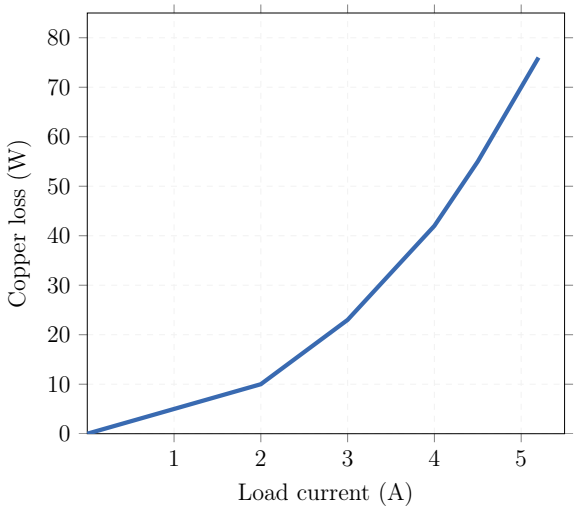

Figure 7.11: Copper loss as a function of load current

The voltage regulation is given by,

$$\eta = \frac{V_{o(NL)} - V_{o(FL)}}{V_{o(FL)}}, \tag{7.3.3}$$

Using the results of the tests and the substituting into equation (7.3.3), the voltage regulation is 2.23 %. A low voltage regulation is beneficial for the application of the RT.

7.4 Summary

The RT is thoroughly tested to access the operation and compare to expected theoretical values. The parameters for the equivalent circuit are determined and compared to the values obtained in the analytical model and FEM analysis. The measured magnetising inductance values and the FEM results correspond well. The measured leakage inductance shows a deviation from the FEM values. This increase in leakage flux is primarily attributed to the poor fit of the primary winding within the window area.

The no load characteristic curve indicates that the RT core size is sufficient for the power rating. This verifies the design methodology outcomes of a minimum core size, without leading to core saturation at the rated conditions. The efficiency constraint of $\eta \geq 90\%$ is met, despite an increase in conduction losses due to the primary turn number being adjusted. The measured efficiency is 93.18%, with the conduction losses being the dominant loss factor.

Chapter 8

Conclusions and Recommendations

The standard DFIG is a widely used wind turbine drive train due to its simplicity and low initial capital cost. The issue of reliability and high cost of maintenance due to the necessary slip rings warrants investigation into brushless generator topologies. The use of a RT with a DFIG is proposed to offer an alternative to standard BDFIGs. For the RT to be a viable replacement to slip rings assemblies and conventional brushless setups, it must meet two criteria: comparable size and efficiency. The main focus of this study is to develop a RT that meets these requirements.

The research procedure involved developing an analytical model to accurately predict the non-idealities of the RT: the main air gap, as well as the air gap introduced by the radial laminations. Using this model, a design methodology is presented that will result in the analytically optimal minimum size, while addressing the unique design constraints of the RT. A design that consists of analytical and FEM analysis is used to produce a single-phase prototype that is tested in order to verify the analytical model and methodology.

8.1 Conclusions

The conclusions of the study to implement a BDFIG design using an RT, are as follows:

- The developed analytical model provides a more accurate representation

of the transformer's magnetising and leakage inductances than the classic approach. The analytical method is however, not as accurate as FEM analysis.

- The RT's size can be reduced significantly by use of grid frequency as opposed to slip frequency. This can be achieved by operating the DFIG in the rotor-tied configuration.
- The design strategy resulted in a significantly reduced transformer size compared to previous developed prototypes of the same power rating, that made use of standard transformer design methods.
- Despite the reduction in size the RT's operation in the linear region is maintained.
- Although optimal size was favoured during the design process, the transformer's efficiency is maintained at 91.3 %.
- The RT experienced increased conduction losses due to the reduction in turn number on the primary winding.
- It is demonstrated by the scalability study that the RT is suitable for high power ratings (MW range) in terms of size. The increased size of the slip rings and their necessary cooling at this power rating may mean the RT's size becomes an advantage.
- The improved mechanical design allowed for a small air gap of 0.4 mm which greatly improves the RT's performance. The air gap length is maintained throughout rotation. Addition of the "inter-laminar" laminations on the secondary side of the core increased the amount of active material, which contributes to the larger linear operating region.
- The RT is complex to construct and requires an involved mechanical design and bulky outer housing

8.2 Recommendations

The results of the study presented in the report highlights numerous important areas where further research and investigation needs to be conducted. The recommended areas of study are as follows:

- Further work must be conducted on the analytical model. The proposed method provided an improved analytical representation of the RT over the standard transformer model, however the results do not correspond closely to FEM and measured results.

- A three phase RT system should be constructed and tested in conjunction with the DFIG to verify the modelled behaviour. An advantage of the classic BDFIG is the improved LVRT capabilities. This is attributed to the increased series inductance. A study should be conducted to evaluate whether the added inductance of the RT can offer a similar improvement on the DFIG's LVRT capabilities.

- Implementation of an optimisation of the three phase RT with efficiency as the primary constraint, to study the efficiencies that can be offered by the RT setup.

- A study should be conducted focusing on the alternative RT topologies that could provide better leakage inductances, especially during rotation.

- Improved mechanical design of the transformer housing in order to reduce the overall size. Consideration should also be done as to the use of Soft Magnetic Composites (SMC's) for the core construction.

- More investigation is necessary into the operation of the DFIG in the rotor-tied configuration. The impact of the new frequency range on the size and core loss needs to be studied. The control of the generator in this setup will also needs to be considered.

Bibliography

[1] Global Wind Energy Council, "GLOBAL WIND REPORT - Annual Market Update," 2014.

[2] H. Polinder, J. A. Ferreira, B. B. Jensen, A. B. Abrahamsen, K. Atallah, and R. A. Mcmahon, "Trends in Wind Turbine Generator Systems," *IEEE Journal of Emerging and Selected Topics in Power Electronics*, vol. 1, no. 3, pp. 174–185, 2013.

[3] A. Stenberg and H. Holttinen, "Analysing failure statistic of wind turbines in finland," VTT Technical Research Centre of Finland, 2010.

[4] J. Lopez, P. Sanchis, X. Roboam, and L. Marroyo, "Dynamic Behavior of the Doubly Fed Induction Generator During Three-Phase Voltage Dips," *IEEE Transactions on Energy Conversion*, vol. 22, no. 3, pp. 709–717, 2007.

[5] L. Meegahapola, T. Littler, and D. Flynn, "Decoupled-DFIG Fault Ride-Through Strategy for Enhanced Stability Performance During Grid Faults," *IEEE Transactions on Sustainable Energy*, vol. 1, no. 3, pp. 152–162, 2010.

[6] C. Wessels, F. Gebhardt, and F. Fuchs, "Fault ride-through of a dfig wind turbine using a dynamic voltage restorer during symmetrical and asymmetrical grid faults," *IEEE Transactions on Power Electronics*, vol. 26, no. 3, pp. 807–815, 2011.

[7] R. Cardenas, R. Pena, S. Alepuz, and G. Asher, "Overview of control systems for the operation of dfigs in wind energy applications," *IEEE Transactions on Industrial Electronics*, vol. 60, no. 7, pp. 2776–2798, 2013.

[8] T. Long, S. Shoa, P. Malliband, E. Abdi, and R. McMahon, "Crowbarless fault ride-through of the brushless doubly fed induction generator in

a wind turbine under symmetrical voltage dips," *IEEE Transactions on Industrial Electronics*, vol. 60, no. 7, pp. 2833–2841, 2014.

[9] B. Ambati and V. Kanjiya, P. andKhadkikar, "A low component count series voltage compensation scheme for dfig wts to enhance fault ride-through capability," *IEEE Transactions on Energy Conversion*, vol. 30, no. 1, pp. 208–217.

[10] A. K. Wallace, R. Spee, and G. C. Alexander, "The brushless doubly-fed machine: its advantages, applications and design methods," *International Conference on Electrical Machines and Drives*, no. 376, pp. 511–517, 1993.

[11] R. Carlson, H. Voltolini, F. Rtincos, and N. J. Batistelal, "Performance Analysis with Power Factor Compensation of a 75 kW Brushless Doubly Fed Induction Generator Prototype," *International Conference on Renewable Energies and Power Quality, ICREPQ*, pp. 1502–1507, 2007.

[12] E. Abdi, X. Wang, S. Shao, R. McMahon, and P. Tavner, "Performance characterisation of brushless doubly-fed generator," pp. 1–6, 2008.

[13] T. Long, S. Shao, E. Abdi, P. Malliband, M. Mathekga, R. McMahon, and P. J. Tavner, "Symmetrical low voltage ride- through of a 250 kw brushless dfig," pp. 1–6, 2012.

[14] M. Ruviaro, F. Rüncos, and N. Sadowski, "Wound Rotor Doubly Fed Induction Machine with Radial Rotary Transformer," *Journal of Microwaves, Optoelectronics and Electromagnetis Applications*, vol. 12, no. 2, pp. 1–16, 2013.

[15] F. Runcos and M. Ruviaro, "A Brushless doubly fed induction machine with flat plane rotary transformers," *International Conference on Electrical Machines*, 2012.

[16] H. Zhong and L. Zhao, "Design and Analysis of a Three-phase Rotary Transformer for Doubly Fed Induction Generators," no. c, pp. 1–6, 2014.

[17] R. Gibson, "Rotary transformers developed to replace slip rings and brushes," pp. 469–470, 1961.

[18] I. A. Gowaid, A. S. Abdel-khalik, S. Member, A. M. Massoud, S. Member, S. Ahmed, and S. Member, "Ride-Through Capability of Grid-Connected

Brushless Cascade DFIG Wind Turbines in Faulty Grid Conditions, A Comparative Study," *IEEE Transactions on Sustainable Energy*, vol. 4, no. 4, pp. 1002–1015, 2013.

[19] H. Liu and L. Xu, "Design and Performance Analysis of a Doubly Excited Brushless Machine for Wind Power Generator Application," *IEEE International Symposium on Power Electronics for Distributed Generation Systems*, pp. 597–601, 2010.

[20] R. A. Mcmahon, E. Abdi, P. D. Malliband, S. Shao, M. E. Mathekga, and P. J. Tavner, "Design and Testing of a Medium-Speed 250 kW Brushless DFIG ," *International Conference on Power Electronics, Machines and Drives*, pp. 1–6, 2012.

[21] E. Abdi, M. R. Tatlow, R. A. Mcmahon, and P. J. Tavner, "Design and Performance Analysis of a 6 MW Medium-Speed Brushless DFIG," *Renewable Power Generation Conference (RPG)*, vol. 7, no. 6, pp. 1–4, 2013.

[22] A. Oraee, E. Abdi, S. Abdi, R. A. Mcmahon, S. John, and C. Cb, "A Study of Converter Rating for Brushless DFIG Wind Turbines," *Renewable Power Generation Conference (RPG)*, vol. 1, no. 2, pp. 3–6, 2013.

[23] T. A. Lipo and D. Panda, "Design and Test of DC Voltage Link Conversion System and Brushless Doubly-Fed Induction Generator for Variable-Speed Wind Energy Applications Design and Test of DC Voltage Link Conversion System and Brushless Doubly-Fed Induction Generator for Variable-Speed Wind Energy Applications," 2005.

[24] H. R. Mohabati, J. S. Moghani, and S. T. Boroujeni, "Fully laminated shell-type three-phase rotating transformer for brushless applications," *Electric Power Applications*, vol. 9, pp. 349–357, 2014.

[25] N. L. Zietsman and N. Gule, "Design and evaluation of a 1 kw rotary transformer," *South African Universities Power Engineering Conference*, 2013.

[26] ——, "Optimal Design Methodology of a Three Phase Rotary Transformer for Doubly Fed Induction Generator Application."

[27] S. Marx and R. Bounds, "A Kilowatt Rotary Power Transformer," *IEEE Transactions on aerospace and electronic systems*, vol. 7, no. 6, pp. 1157–1163, 1971.

[28] M. Tosi, "Rotary Transformer Design for Brushless Electrically Excited Synchronous Machines," Master's thesis, University of Padua, 2014.

[29] Y. You, T. A. Lipo, and B. Kwon, "Design and Analysis of a Novel Grid-Connected to Rotor Type Doubly Fed Induction Machine," *IEEE Transactions on Magnetics*, vol. 48, no. 2, pp. 919–922, 2012.

[30] B. A. Potter, "Design , Implementation and Characterisation of a Contactless Power Transfer System for Rotating Applications," *Conference on Industrial Electronics (IECON)*, pp. 2168–2173, 2006.

[31] E. Landsman, "Rotary Transformer Design," pp. 139–152.

[32] C. W. M. T. Mclyman, *Transformer and Inductor Design Handbook*, 3rd ed. Marcel Dekker, Inc, 2004.

[33] K. D. Papastergiou and D. E. Macpherson, "An Airborne Radar Power Supply With Contactless Transfer of Energy, Part I : Rotating Transformer," *IEEE Transactions on Industrial Electronics*, vol. 54, no. 5, pp. 2874–2884, 2007.

[34] J. Legranger, G. Friedrich, S. Vivierl, and J. C. Mipo, "Comparison of two optimal rotary transformer designs for highly constrained applications," *Internationsl Electric machines and drives conference*, vol. 2, pp. 1546–1551, 2007.

[35] R. Chacko, R. Mh, S. Mk, T. Sabu, S. A. Vt, and J. Cc, "Magnetic Slip Ring, Rotary Transformer Based Novel Non-Contact Signal transfer Mechanism for Spacecraft Application."

[36] R. Trevisan, S. Member, A. Costanzo, and S. Member, "A 1 kW Contactless Energy Transfer System Based on a Rotary Transformer for Sealing Rollers," *IEEE Transactions on Industial Electronics*, vol. 61, no. 11, pp. 6337–6345, 2014.

[37] A. Abdolkhani, A. P. Hu, and N. C. Nair, "Modelling and Parameters Identification of Through-Hole Type Wind Turbine Contactless Sliprings," *Engineering, Scientific Research*, pp. 272–283.

[38] W. G. Hurley, W. H. Wölfle, and J. G. Breslin, "Optimized Transformer Design : Inclusive of High-Frequency Effects," *IEEE Transactions on Power Electronics*, vol. 13, no. 4, pp. 651–659, 1998.

[39] M. Say, *The performance and design of alternating current machines*, 3rd ed. Sir Isaac Pitman & Sons Ltd.

[40] *Electrical Steel Non Oriented Fully Processed*, Cogent Power Ltd.

[41] K. D. Papastergiou and D. E. Macpherson, "Contact-less Transfer of Energy by means of a Rotating Transformer," pp. 1735–1740, 2005.

[42] I. Boldea, *The Induction Machine Handbook*. CRC Press, 2002.

[43] B. Y. G. Kroni, "Rules to Predetermine Crawling , Vibration , Noise and Hooks in the Speed-Torque Curve Induction Motor Slot Combinations," vol. 50, no. 1, pp. 757–767, 1931.

Appendices

Induction machine design

The design of a simple retrofit wound rotor induction machine is presented in this chapter. The design is done in order to have a prototype machine with which to test the RT.

Rotor Design Strategy

Standard induction machine design techniques rely on the output coefficient or loading distribution method as a starting point. The concept is that for a given rated input power, and based on the electric and magnetic loadings specified, there will be a product D^2L which will govern the machine's size outer diameter, D, and stack length, L.

Since an existing induction motor is being used a number of the constraints are already set. The outer diameter, D and stack length, L are fixed by the original stator. The new wound rotor is designed in accordance with these constraints and to meet the necessary specifications. The overall design procedure is shown in Figure 1.

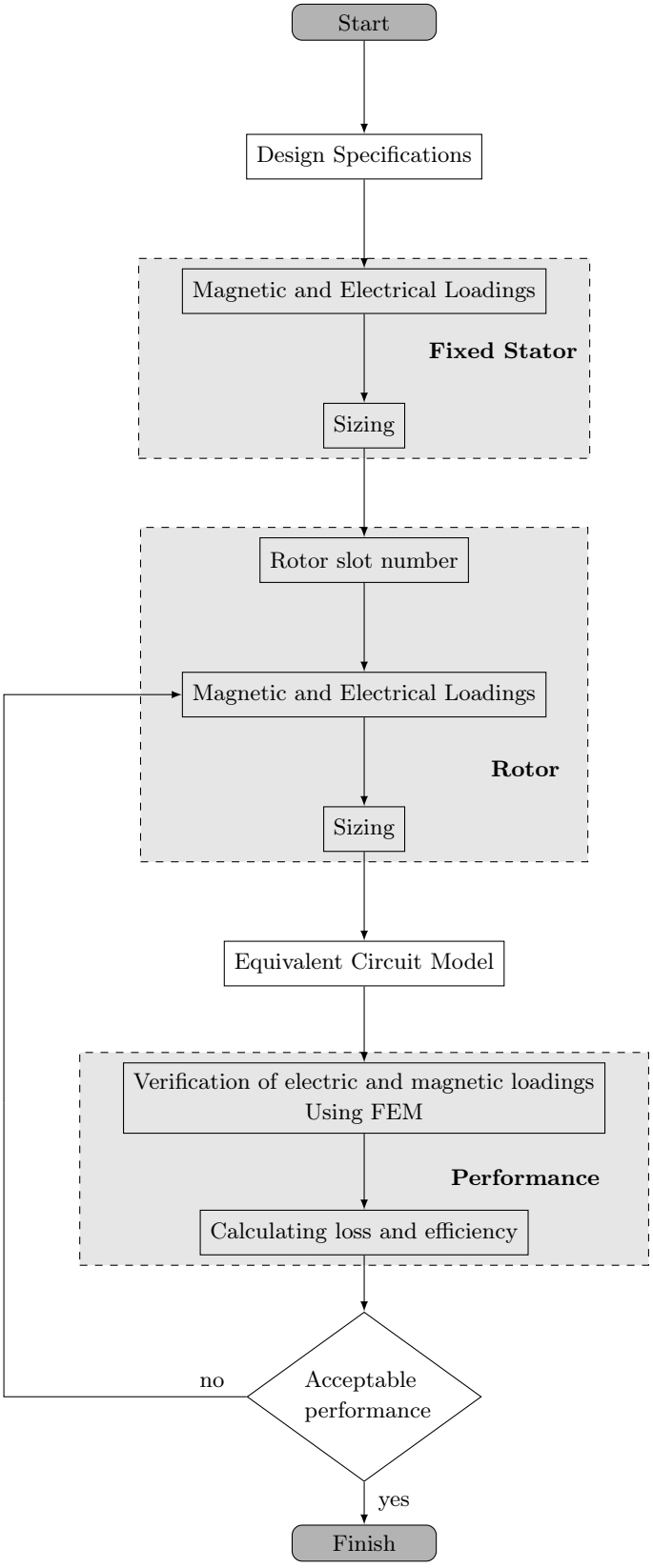

Figure 1: Flow chart illustrating the wound rotor induction machine design procedure

A standard efficiency, off-the-shelf 3 kW WEG squirrel cage motor is used. The specifications are shown in Table 1. The geometry of the motor is presented in Table 2.

A new wound rotor is designed using the fixed dimensions as a starting point. The first constraint that needs to be decided on is the number of rotor slots. This is affected by the already fixed number of stator slots. A suitable combination between rotor and stator slot number is necessary to avoid crawling, vibration and noise. A detailed investigation into the possible rotor slot numbers and winding is presented in the following section.

Table 1: WEG squirrel cage motor specifications

Parameter	Value
Rated output power	3 kW
Rated voltage	400 V (Wye)
Number of poles	4
Frame size	100L

Table 2: Machine geometry

	Stator	Rotor
Outer diameter	160 mm	99.3mm
Inner diameter	100 mm	34.7 mm
Stack length	130 mm	
Air gap	0.35 mm	

Choice of Rotor Slot Number

There are two types of harmonics that can manifest in machine operation: time and space harmonics. Time harmonics are introduced by the input supply to the machine, and cannot be mitigated during the machine design process. Space harmonics are a consequence of the non sinusoidal distribution of the coils in slots around a stator or rotor. The results of these harmonics manifest

in the following ways:

1. Distortion of the induced voltage waveforms
2. Parasitic torques
3. Vibration and noise
4. Increase in core loss (high frequency components of the induced voltages)

Mitigation of these nonidealities can be done in the choice of a combination between stator and rotor slot number (N_s and N_r), slot geometry and winding topologies. The existing cage rotor has 28 slots, which in combination with the stator's 36 slots is a frequently used ratio for a 4 pole induction motor [42]. The rotor being wound means that the rotor slot number needs to be divisible by the number of phases, hence a multiple of three. The most suitable options for N_r are provided in Table 3. A thorough evaluation of each option is conducted and 18 is eliminated due to the high risk of cogging. Since $36/18 = \text{int}(2)$, each of the rotor slots can align with two stator slots and cause the motor to lock on start up. 30 and 33 are eliminated based on the narrow rotor tooth that would result from such a high number of slots. Both 21 and 27 would result in a double layer, fractional slot winding, while 24 will yield a simple integral slot winding. Although 24 results in a simpler winding, the combination of 36/24 stator to rotor slots is unfavourable. The risk of cogging at this combination is high and evidence of parasitic torques is provided in [43]. For this reason the final choice is between 21 and 27 rotor slots. 27 is ultimately chosen, in keeping with the general rule of $\text{Nr} > 0.75\text{Ns}$
The fractional slot winding is an atypical layout for induction motors due to the pole asymmetry introduced and is more complicated to wind. Despite

Table 3: Comparison of slot numbers and winding topologies

Nr	Evaluation
18	Fractional winding; Severe cogging
21	Fractional winding
24	Integral winding; Evidence of cogging and parasitic torque hooks
27	Fractional winding
30	Number too great - narrow teeth
33	Number too great - narrow teeth

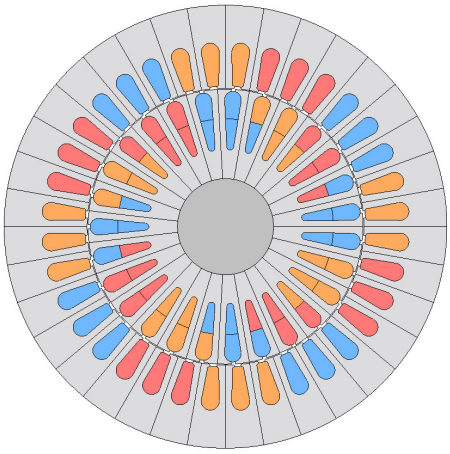

Figure 2: Phase grouping and winding layout of the induction machine rotor

this, with the correct choice in slots/pole/phase, the harmonic content of the air-gap flux density can be reduced [42].

The winding factor (k_w) provides the ratio between the amount of flux that would have been linked by a single layer, full pitch integer slot winding of same number of turns and slots/pole/phase, and that which is linked by the actual winding. It is comprised of three separate factors, namely pitch (k_p), distribution (k_d) and skew factors (k_s), such that

$$k_w = k_p.k_d.k_s. \tag{.0.1}$$

The pitch factor can be calculated as,

$$k_p = sin(n\frac{\pi}{2}\frac{coilspan}{polepitch}), \tag{.0.2}$$

the distribution factor is,

$$k_d = \frac{sin(n\frac{\pi}{6})}{qsin(n\frac{\pi}{6q})}, \tag{.0.3}$$

and the skew factor is,

$$k_s = \frac{sin(np\frac{\gamma}{4})}{np\frac{\gamma}{4}}. \tag{.0.4}$$

where γ is the skew angle in mechanical radians.

The rotor winding data is calculated from equation (.0.1)-equation (.0.4), and the results are presented in Table 4.

Table 4: Rotor winding data

Parameter	Value	Parameter	Value
Number of poles (p)	4	Average coil span	7 slots
Number of phases	3	Slots/pole/phase (q)	$\frac{9}{4}$
Number of slots	27	Pitch factor (k_p)	0.985
Number of layers	2	Distribution factor (k_d)	0.980
Pattern	Overlap	Skew factor (k_s)	0.995
Connection	Series	Winding factor (k_w)	0.960

Magnetic and Electrical Loadings

The magnetic and electric loading of the stator is already fixed depending on the tooth width and wire thickness used respectively. The magnetic loading is chosen such that the tooth flux density does not exceed 1.8 T. The chosen current density for the rotor windings is 5.5 A/mm^2. The number of turns on the rotor, N_2 needs to be determined. This is determined by the desired rotor voltage, stator voltage and number of turns as,

$$N_2 = \frac{E_2 k_{w1} N_1}{E_1 k_{w2}}, \tag{.0.5}$$

where E_2 is the desired rotor emf, E_1 is the stator emf, N_1 is the number of turns on the stator and k_{w1} and k_{w2} are stator and rotor winding factors, respectively.

The stator phase emf is 230 V, with 180 turns/phase. The required rotor emf is 230 V, with the corresponding number of turns is 180. The rotor slot shape is determined based on predetermined suitable shapes for good performance. The actual slot area required is calculated based on the number of turns, rated current density and a suitable fill factor. The resultant rotor slot shape is shown in Figure 3. The area is based on 180 turns, at 5.5 A/ mm^2 and a fill factor of 0.4. The semi-open slot is necessary for placing the winding

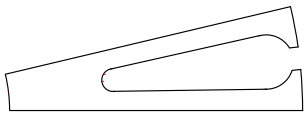

Figure 3: Rotor slot geometry

on the rotor. A summary of the fixed stator and designed rotor winding is given in Table 5.

Table 5: Induction machine stator and rotor winding data

Stator		Rotor	
Number of poles	4	Number of poles	4
Number of phases	3	Number of phases	3
Number of slots	36	Number of slots	27
Number of layers	1	Number of layers	2
Coil span	1:8:10	Average coil span	7 slots
Pattern	Concentric	Pattern	Overlap
Connection	Series	Connection	Series
Turns per coil	30	Turns per coil	20

Equivalent Circuit

The equivalent circuit of the IM is shown in Figure 4. The resistances and inductances can be calculated analytically in order to build an accurate model to be used in finite element analysis (FEM). The stator phase resistance is,

$$R_1 = \rho_{cu} \frac{l_{c1} N_1}{A_{c1}}, \tag{.0.6}$$

where ρ_{cu} is the resistivity of copper, l_{c1} is the length of the winding, N_1 is the stator number of turns, and A_{c1} is the cross sectional area of the copper.

Similarly, the rotor resistance is given by

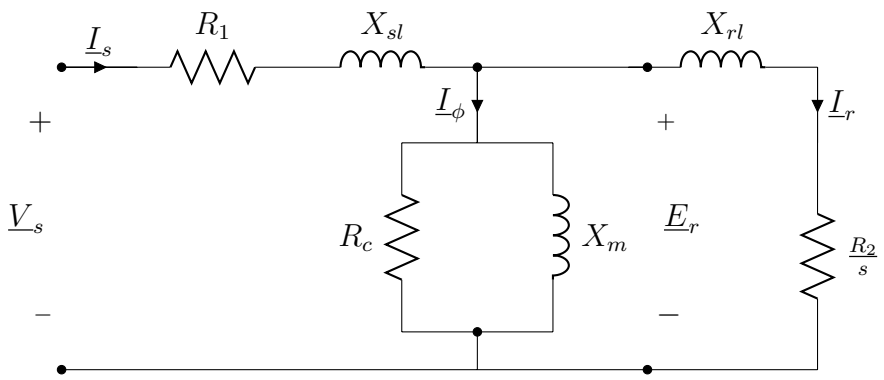

Figure 4: Equivalent circuit model of the induction machine

$$R_2 = \rho_{cu} \frac{l_{c2} N_2}{A_{c2}}, \tag{.0.7}$$

where ρ_{cu} is the resistivity of copper, l_{c2} is the length of the winding, N_2 is the rotor number of turns, and A_{c2} is the cross sectional area of the copper.

The stator and rotor leakage inductances, X_{sl} and X_{rl}, are calculated using,

$$X_{sl} = 2\mu_0 \omega L \frac{(N_1)^2}{p_1 q} (\lambda_s 1 + \lambda_d s1 + \lambda_c c1) \tag{.0.8}$$

and,

$$X_{rl} = 2\mu_0 \omega L \frac{(N_2)^2}{p_2 q} (\lambda_s 2 + \lambda_d s2 + \lambda_c c2), \tag{.0.9}$$

where λ_{s1} and λ_{s2}, λ_{ds1} and λ_{ds2}, λ_{cc1} and λ_{cc2} are slot, differential and end ring coefficients respectively.

The expressions in equation (.0.8) and equation (.0.9) are from [42]Using the developed equivalent circuit and the design geometry, FEM analysis of model can be done. This model can be used to verify the magnetic and electrical loadings of the designed rotor. The performance of the machine can also be evaluated at this point.

RT Mechanical Design Drawings

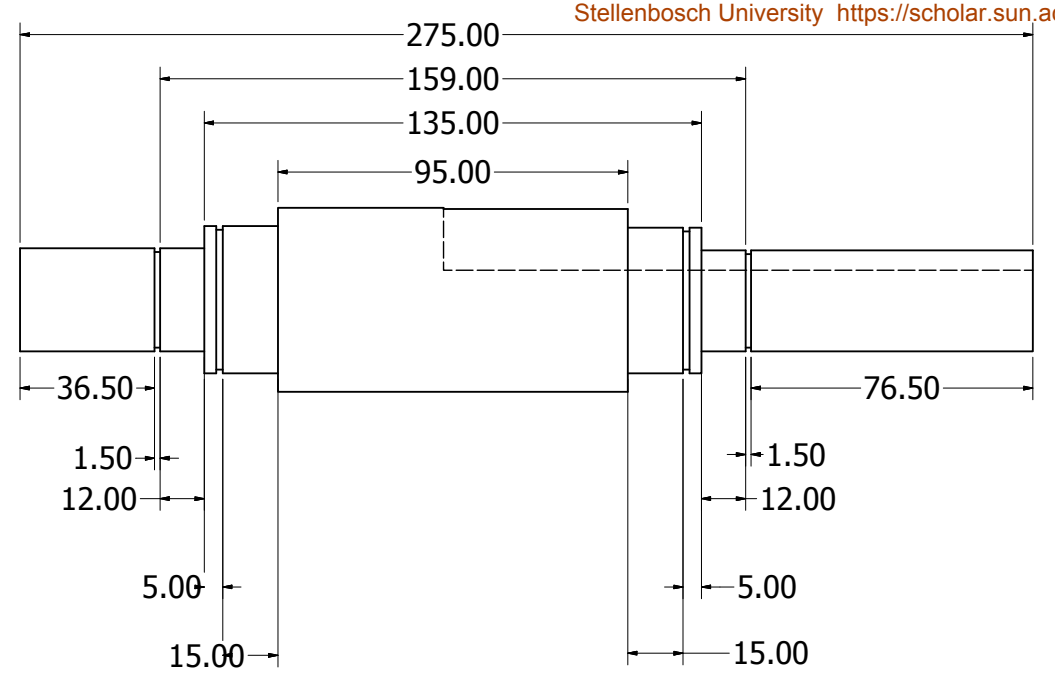

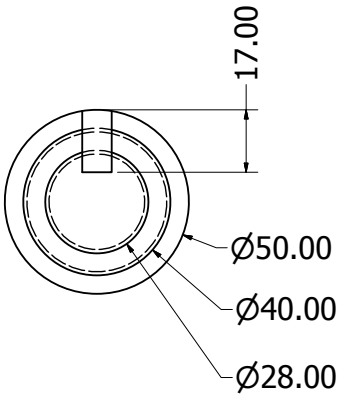

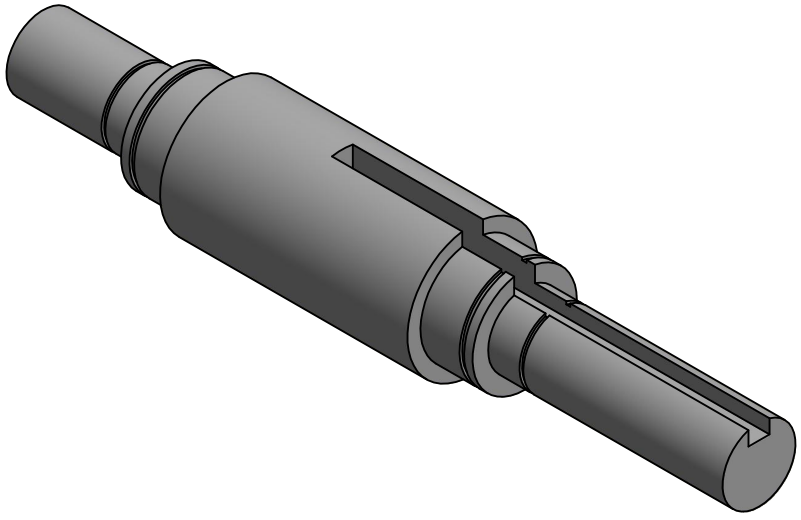

DRAWN 15714403	2015/06/10		
CHECKED		TITLE	
QA			
MFG			
APPROVED			
		SIZE C / DWG NO Shaft / REV	
		SCALE	SHEET 1 OF 1

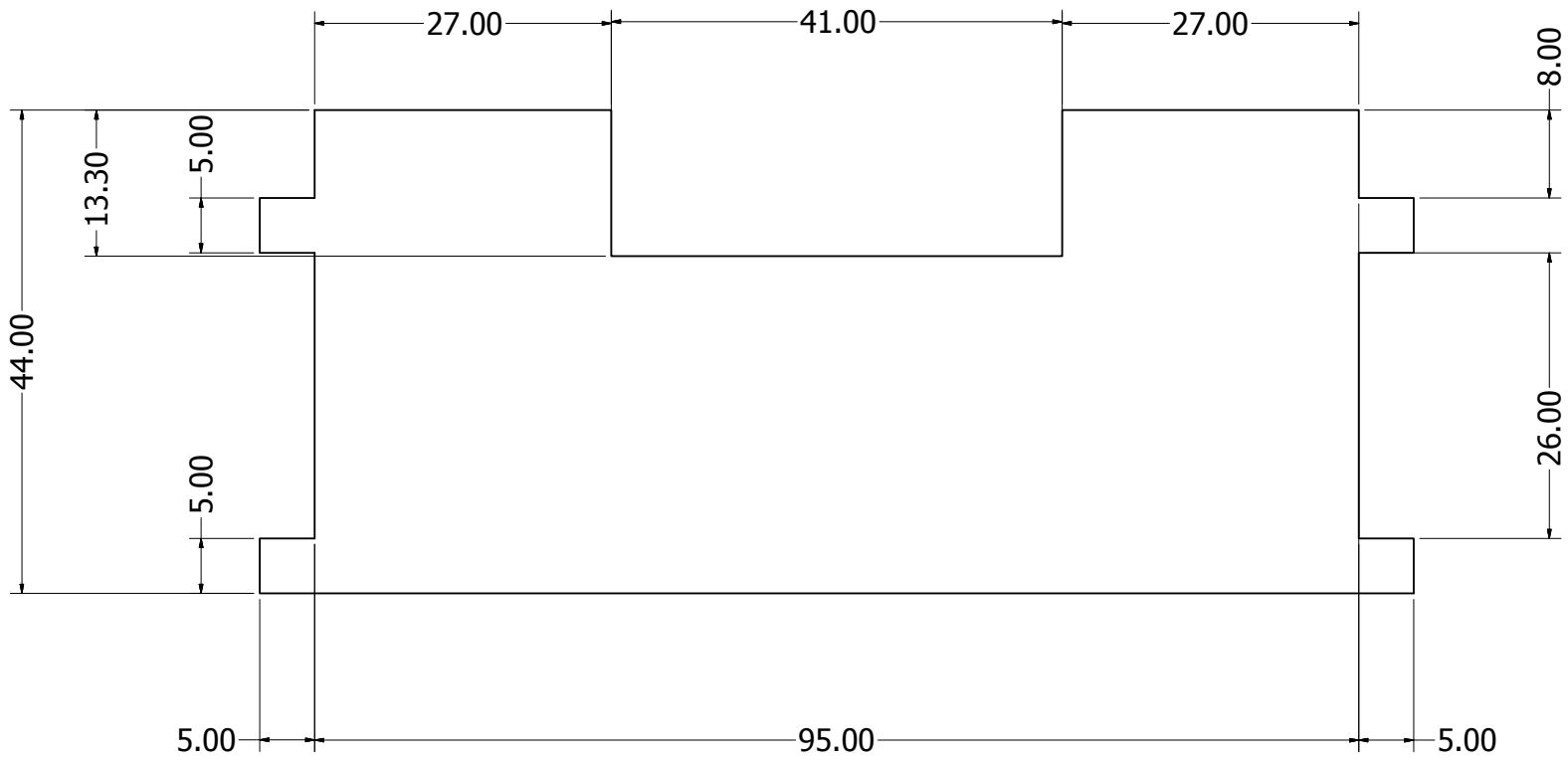

DRAWN 15714403	2015/06/10	
CHECKED		TITLE
QA		
MFG		
APPROVED		
		SIZE C / DWG NO Rotor Lamination / REV
		SCALE / SHEET 1 OF 1

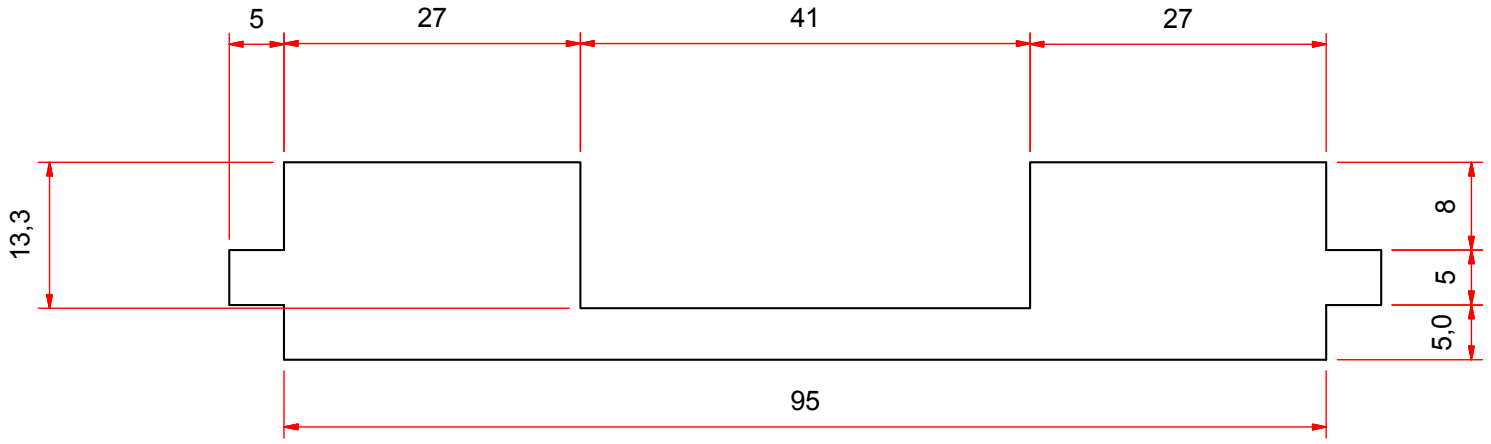

ITEM	BESKRYWING	AANTAL	MATERIAAL / SPESIFIKASIES

UNIVERSITEIT VAN STELLENBOSCH

SKAAL OP A	TITEL:	
MATE IN		
DATUM	VEL No. VAN VELLE	No.

STUDENTE No.	TEKENAAR	NAGESIEN

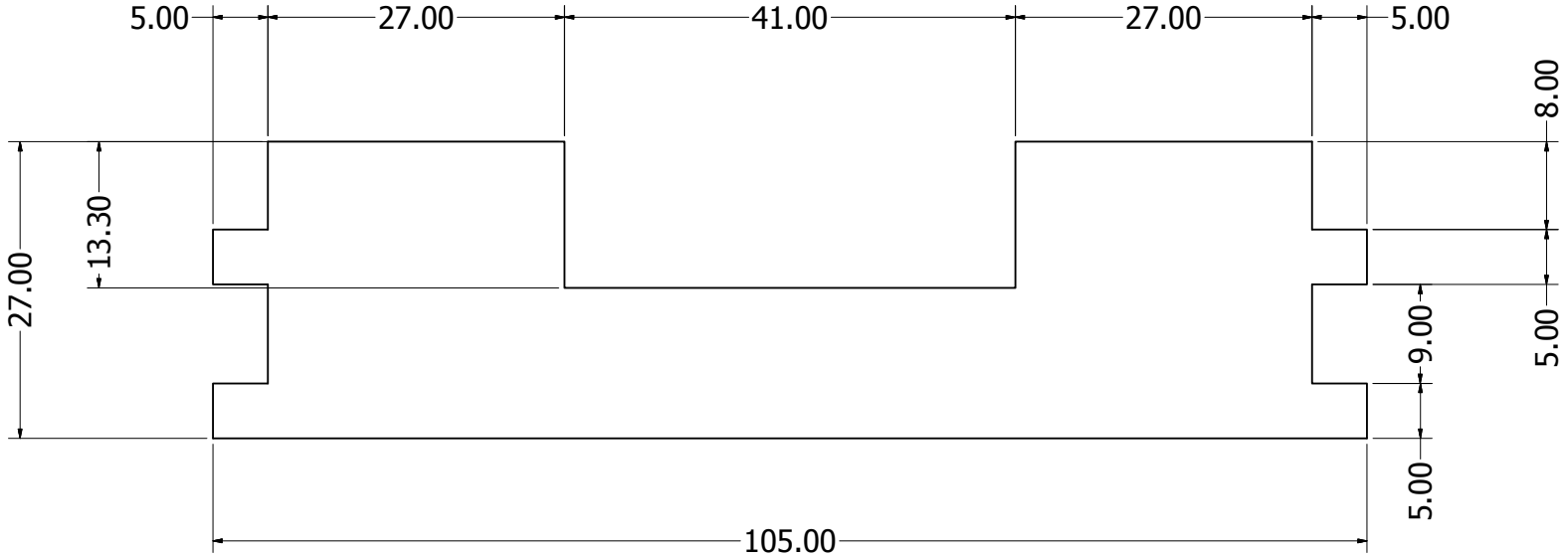

DRAWN 15714403	2015/06/10				
CHECKED					
QA			TITLE		
MFG					
APPROVED					
		SIZE C		DWG NO Stator Lamination	REV
		SCALE		SHEET 1 OF 1	

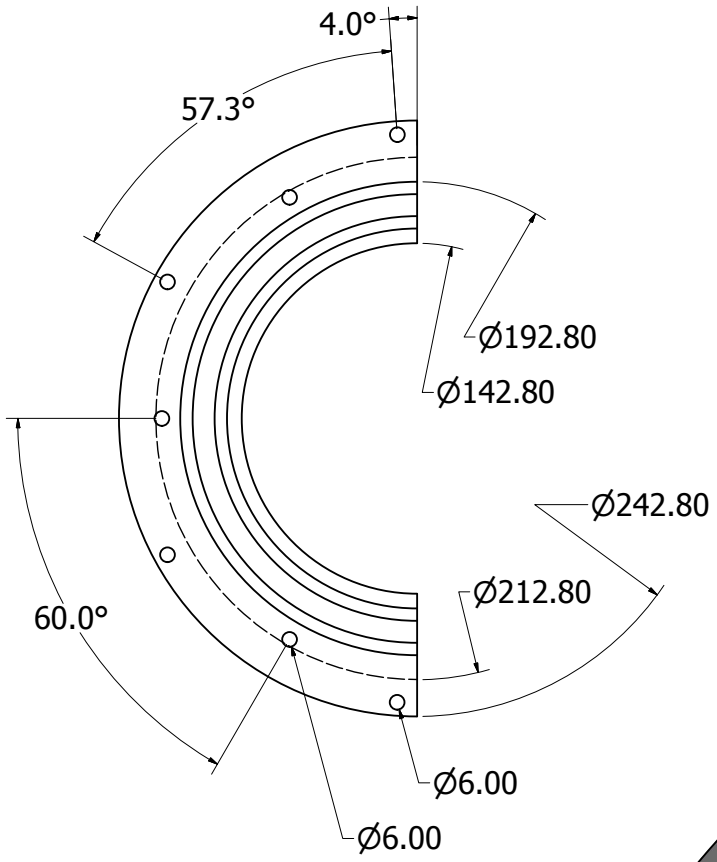

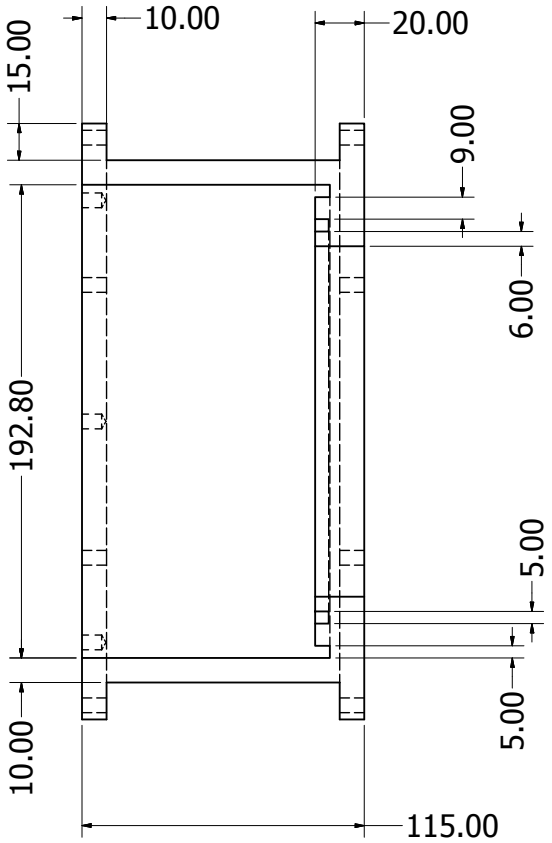

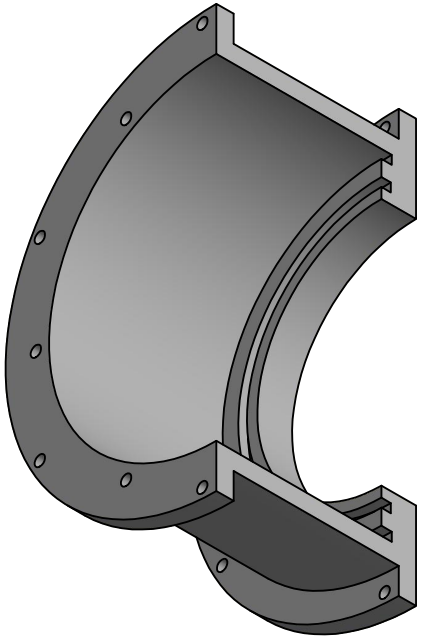

DRAWN 15714403	2015/06/10			
CHECKED				
QA		TITLE		
MFG				
APPROVED		SIZE C	DWG NO Stator H1	REV
		SCALE	SHEET 1 OF 1	

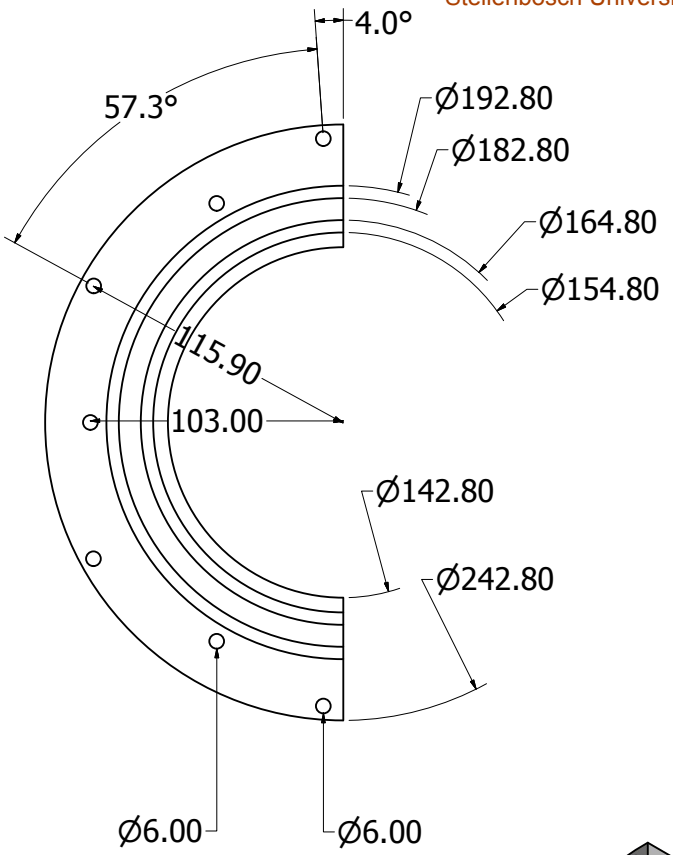

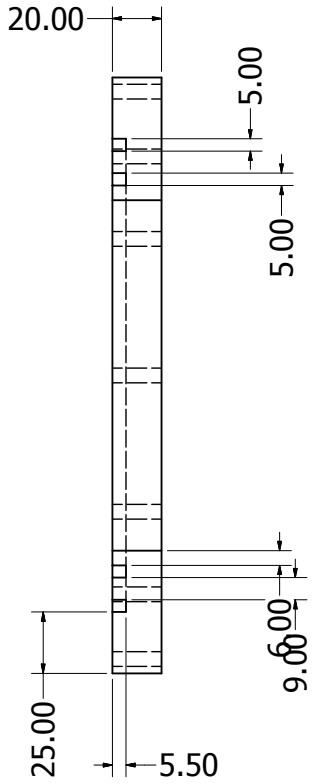

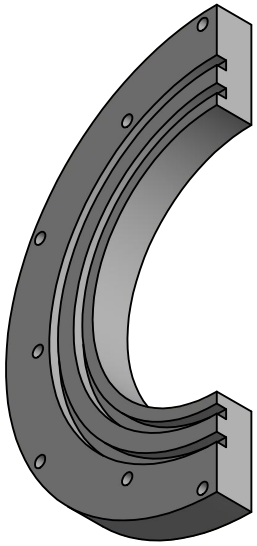

DRAWN 15714403	2015/06/10			
CHECKED		TITLE		
QA				
MFG				
APPROVED		SIZE C	DWG NO Stator H2	REV
		SCALE	SHEET 1 OF 1	

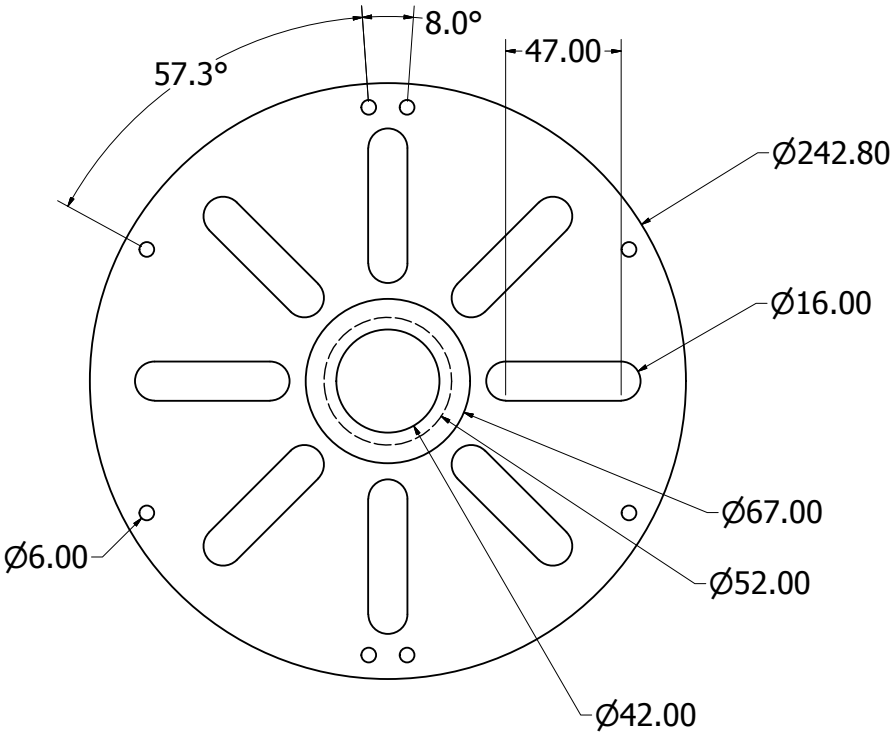

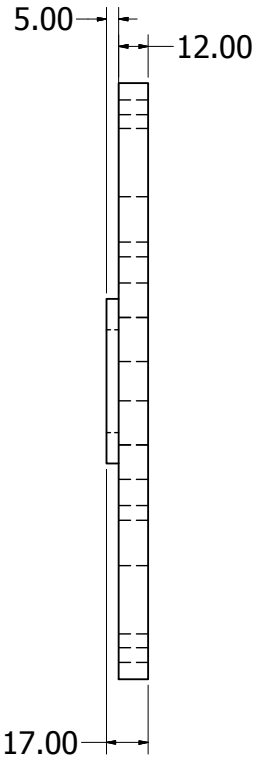

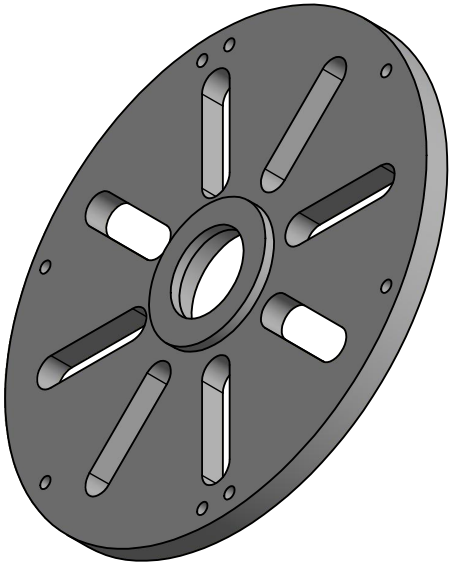

DRAWN 15714403	2015/06/10			
CHECKED		TITLE		
QA				
MFG				
APPROVED				
		SIZE C	DWG NO Bearing End Plate	REV
		SCALE	SHEET 1 OF 1	